Winter 1993

Description and Dynamics of 50-Day Oscillations in the Western Tropical Region of the CME Model

Julie Lorraine McClean
Old Dominion University

DESCRIPTION AND DYNAMICS OF 50-DAY OSCILLATIONS IN THE WESTERN TROPICAL REGION OF THE CME MODEL

by
Julie Lorraine McClean

M.Sc., December 1987, University of Sydney, Sydney, Australia
B.Sc., April 1981, Monash University, Melbourne, Australia

A Dissertation submitted to the Faculty of
Old Dominion University in Partial Fulfillment of the
Requirement for the Degree of

DOCTOR OF PHILOSOPHY
OCEANOGRAPHY

OLD DOMINION UNIVERSITY
JANUARY, 1993

Approved by:

John M. Klinck (Director)

Larry P. Atkinson

Gabriel T. Csanady

John E. Kroll

Abstract

DESCRIPTION AND DYNAMICS OF 50-DAY OSCILLATIONS
IN THE WESTERN TROPICAL REGION OF THE CME MODEL

Julie Lorraine McClean

Old Dominion University, 1993
Director: Dr. John M. Klinck

The WOCE Community Modelling Effort (CME) general circulation model of the north Atlantic was used to investigate the behavior, nature and dynamics of 50-day oscillations seen in the meridional component of velocity between 35° and 55°W and between 5° and 11°N. Validation studies showed that the model reproduced the surface circulation in this area with a reasonable degree of accuracy, in particular, the characteristic seasonal variability. From June to December, the North Brazil Current (NBC) retroflects to form the western arm of the North Equatorial Countercurrent (NECC). Associated with the NECC is a standing meander pattern which extends from the retroflection region (50°W, 7°N) into the interior of the basin (35°W, 5°N), and has a wavelength of about 800 km. This meander pattern starts to break down in December and concurrently, oscillations of the meridional component of velocity appear with a period of about 50 days. They appear first near 35°W, and are advected westward. They have a westward

phase velocity of 0.1 m s^{-1}, wavelength of about 500 km and a very slow eastward group velocity. Their period, phase speed and wavelength agree with observations [Johns et al. 1990]

Calculation of the leading balance of terms from the full vorticity equation following a modal decomposition in the propagation region, showed that the oscillations were first and second mode baroclinic Rossby waves. Repetition of the vorticity analysis during the period of the retroflection revealed the NECC meanders also to be first and second mode baroclinic Rossby waves; the same as the 50-day oscillations. These findings, together with the time evolution of the individual flow components over an annual cycle, suggested that the 50-day oscillations were the westward advected residue of the NECC meander pattern that is released as the NECC slows in fall. The retroflecting NBC produces Rossby waves with very slow eastward group velocity that are advected eastward until they reach 35°W, where they dissipate. A standing wave pattern is established for several months, while the NECC is active. Once it slows, the waves retreat westward and disappear totally by May. Wind forcing was not considered to be responsible for the oscillations in this model.

To my parents

Barry and Shirley McClean

Acknowledgements

I wish to thank my advisor, Dr. John Klinck, for his guidance and support. His sound direction and calmness helped me overcome many hurdles during the pursuit of this degree. My thanks also go to the other members of my committee, Dr. Gabe Csanady, Dr. Larry Atkinson and Dr. John Kroll. I am particularly grateful to Dr. Csanady for the time and effort he put into this thesis. Dr. Atkinson and Dr. Kroll are also thanked for their time and encouragement.

Dr. Mike Spall is acknowledged for providing the vorticity analysis code and for helpful discussions. The faculty, particularly Dr. Lew Rothstein, from the "Workshop on the Physics of Equatorial Oceans" are appreciated for giving me the opportunity to attend this meeting. Dr. Jay McCreary is acknowledged for originally suggesting that I look for 50-day oscillations in the CME model. Dr. Denny Kirwan, Dr. John Adam and Dr. Pete Spain are all thanked for helpful discussions as well as their friendships. Thanks are due to Dana Oblak for her outstanding assistance with administrative problems. Dr. Wayne Schroll is thanked for his help with computer related problems, as is Ken Hansen at NCAR. Dr Glen Wheless is gratefully acknowledged for producing the movie shown at my oral defense. The work was supported by NSF grant OCE-89-22860.

All the folks at CCPO and the Oceanography Department are thanked for their friendship and encouragement over the last four years, particularly Margaret

Dekshenieks, Karal Gregory, Lisa Hommel, Cathy Lascara, Ana Martins, John Moisan, Tiffany Moisan, Caitlin Mullen and Yvette Spitz. I am especially grateful to Linda Pirkle, Carolyn Pirkle and Judy Walker for their constant support and friendship during both the good and the bad times.

Contents

List of Figures

List of Tables

1 Introduction

Recently, oscillations of the meridional component of velocity, with a mean periodicity of about 50 days, have been observed in the western tropical Atlantic by Johns et al. [1990]. These observations were obtained from a moored current meter array that was deployed off French Guiana in September 1987 at the locations seen in Figure 1. Mooring B, located over the slope, and mooring C, deployed in 5000 m of water, were recovered in July 1988 and September 1988, respectively. The oscillations were present all year, however their period varied from 40 to 60 days, with the shortest periods occurring in spring and the longest in fall. They were observed over the top 900 m of the water column with the strongest signature occurring at the upper current meter at 100 m depth (Figure 2). Peak-to-peak fluctuations in excess of 1 m s^{-1} were recorded.

The narrow-band, almost deterministic nature of the signal lead Johns et al. [1990] to suggest that the oscillations arose from a single coherent wave process. Consequently, they determined the dispersion characteristics of the oscillations by examining the horizontal phase relations between moorings B and C. Figure 3 shows variance-preserving spectra of the meridional component of velocity at the 300-m level on mooring B and at the 200-m level on mooring C, as well as the cross-spectrum between these velocity components. The variance-preserving spectra (Figure 3a) show coherent peaks centered near 40-50 days with a rapid decay of energy toward higher frequencies. Energy spectra of the meridional velocity in the upper 900 m of the water column display similar characteristics. A significant peak at the

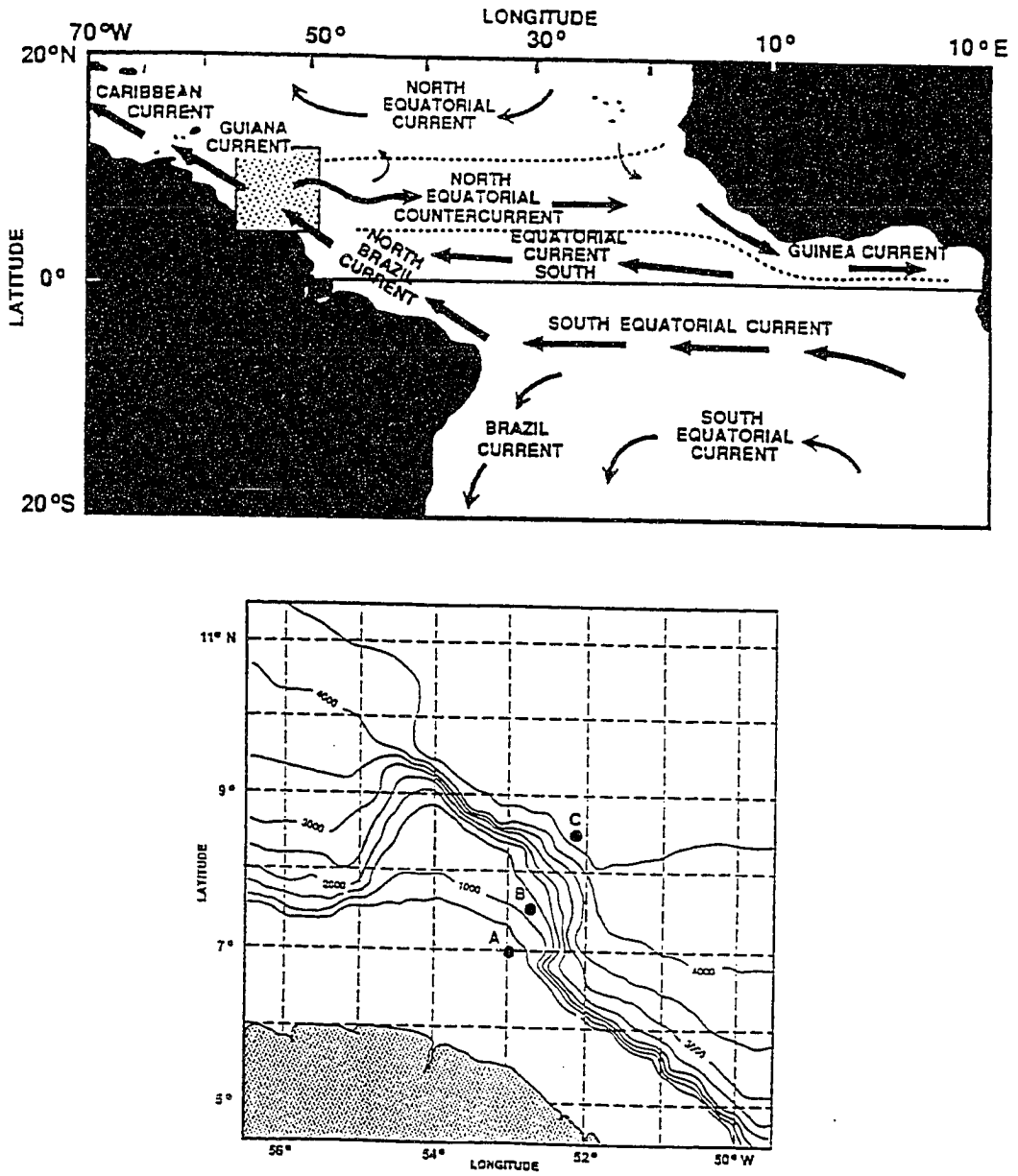

Figure 1: Local area map showing mooring locations and bathymetry for the shaded region indicated in the top diagram (after Johns et al. [1990]).

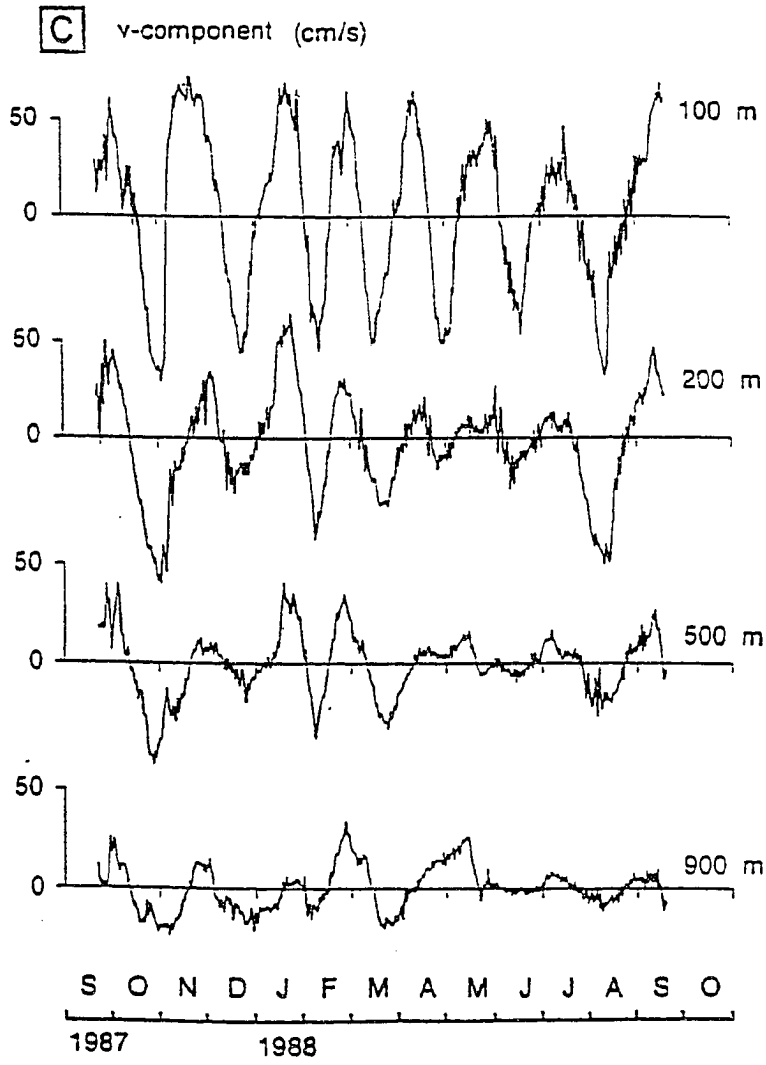

Figure 2: Time series of meridional velocity over the upper 1000 m at mooring site C (after Johns et al. [1990]).

95% level is seen in the squared coherence in the 40-60 day band (Figure 3b), while the phase difference is -45° (Figure 3c), meaning that the currents at the mooring B (the most westward site) lag those at mooring C by about 6 days. If a wave is assumed to have propagated through the array, its wavelength is 520 km with a range of 390-740 km and its phase speed is -0.12 m s^{-1} with a range of -0.09 to -0.17 m s^{-1}. These estimates were found to be consistent with the characteristics of an off-equatorial first baroclinic mode Rossby wave.

Johns et al. [1990] have speculated as to the cause of the 50-day oscillations. Due to their spatially limited data set, they were unable to definitively determine the cause or origin of the oscillations. The two major currents in the region, the North Brazil Current (NBC) and the North Equatorial Countercurrent (NECC), exhibit strong seasonal variability. In the fall, the NBC retroflects, or turns back on itself, to form the western arm of the eastward flowing meandering NECC (Figure 1). During the spring, the NECC is replaced by westward flow and the NBC continues northwestward along the coast of South America toward the Caribbean. One possible cause of the 50-day oscillations suggested by Johns et al. [1990] is that they are eddies which are shed from the NBC retroflection region as a result of a local instability process. Alternatively, they suggested that the oscillations may result from the westward movement of the NECC meander pattern that is released when the NECC decays at the end of fall. In an attempt to better understand the dynamics of the oscillations, they examined output from the eddy resolving, high viscosity World Ocean Circulation Experiment (WOCE) Community Modeling Effort (CME) general circulation model. No evidence was found in the model of the oscillations.

Oscillations with periods of 50 days have also been observed south of the equator

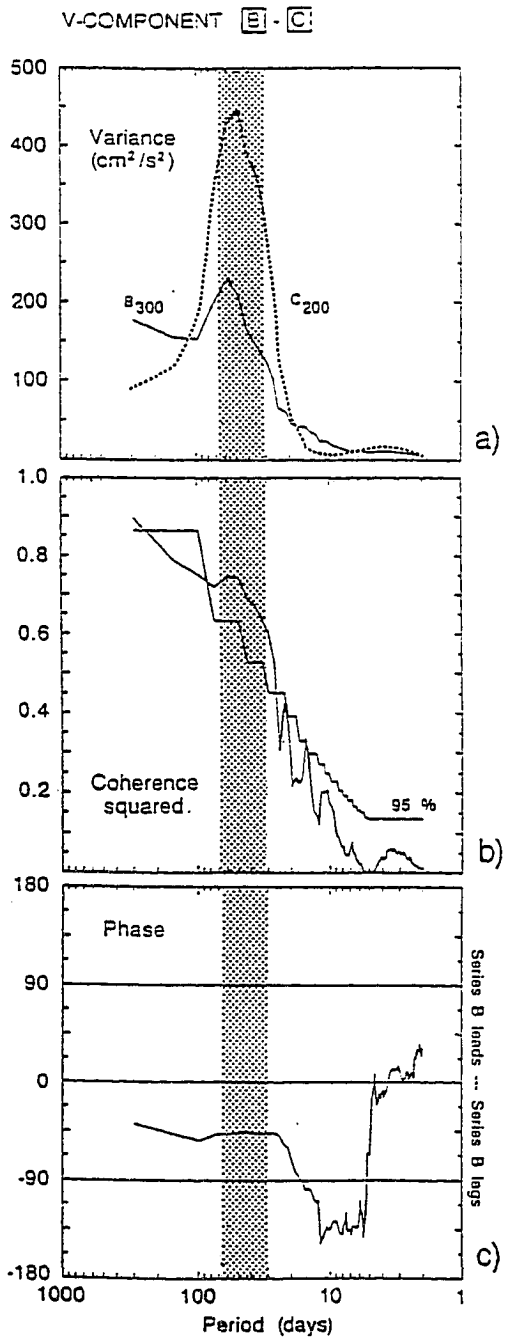

Figure 3: (a) Variance-preserving spectra and (b) coherence-squared and (c) phase of meridional velocity between the 200-m level on mooring C and 300-m level on mooring B (after Johns et al. [1990]).

in the western Indian ocean, a region suggested by Johns et al. [1990] to be dynamically similar to that of the NBC retroflection. The South Equatorial Current splits at the coast of Madagascar into northward and southward branches. During the northeast Monsoon (November to March), the northward branch rounds the tip of Madagascar at 12°S and continues north along the coast of Africa as the East African Coastal Current (EACC). During this season, the Somali Current flows southward across the equator and joins the EACC off Kenya to form an eastward South Equatorial Countercurrent (SECC) [Swallow et al. 1988]. Climatological mean surface currents for this period (Figure 4a), compiled from ship drift data, show this current to meander as it flows offshore [Swallow et al., 1991]. During the southwest Monsoon (May to September), the EACC flows into the northward flowing Somali Current (Figure 4b).

Mysak and Mertz [1984] found 40- to 50-day oscillations in the longshore current and temperature fluctuations that were measured in the Somali Current source region at 3°S, 41°E off Kenya, from January to July 1976. They found similar period fluctuations in the zonal wind stress component collected at 2.5°S, 47.5°E during these months. The latter signal was the 40- to 50-day oscillation of the tropospheric wind field discovered by Madden and Julian [1972]. Consequently, they attributed the oceanic oscillations to forcing by this atmospheric signal. The coupling mechanism was not understood. Alternatively, they suggested that since the Somali Current had strong lateral shears, the oscillations may be due to barotropic instability. Atmospheric forcing was also suggested by Quadfasel and Swallow [1986] as the cause of 50-day oscillations found off the northern tip of Madagascar in the South Equatorial Current (SEC) during March to July, 1975. They did not, however, have any wind data to substantiate their claim. Later, Schott et al. [1988] found that the wind field in this region did not have a prominent peak in the 40-

to 50-day period and instead, attributed the oscillations to shear instability of the zonal current system.

Kindle and Thompson [1989] found 50-day oscillations of the meridional velocity component in their reduced-gravity model of the western Indian ocean between 3° and 8°S and west of 55°E. Realistic basin geometry north of 30°S was used, while the model was forced with Hellerman and Rosenstein [1983] monthly wind stress climatology. The oscillations initially appeared at 55°E where the meander pattern associated with the eastward flowing offshore branch of the EACC first broke down. The onset of the oscillations and the break down of the meander pattern occurred almost coincidentally during April. The oscillations were seen near the coast of Africa (40°E) by mid-June. Westward flow also appeared at 55°E during April and then at progressively westward locations, until it was seen near the coast in June. As a result, Kindle and Thompson [1989] attributed the oscillations to barotropic instability. Wind forcing was not considered to be responsible since little wind energy was contained in the 40- to 60-day period in the model forcing. They also found these oscillations to have the character of first baroclinic mode Rossby waves.

The mechanisms proposed by these investigators for the 50-day oscillations observed in the western Indian ocean were largely speculative. Kindle and Thompson [1989] ruled out wind forcing in their model, however they did not rigorously test their barotropic instability hypothesis. Mysak and Mertz [1984] found similar period oscillations in the ocean and atmosphere but failed to establish a dynamical relationship between the two. Quadfasel and Swallow's [1986] observations were suggested by later investigators to be due to barotropic instability [Schott et al. 1988] or baroclinic instability [Kindle and Thompson, 1989]. These explanations, however, were again speculative.

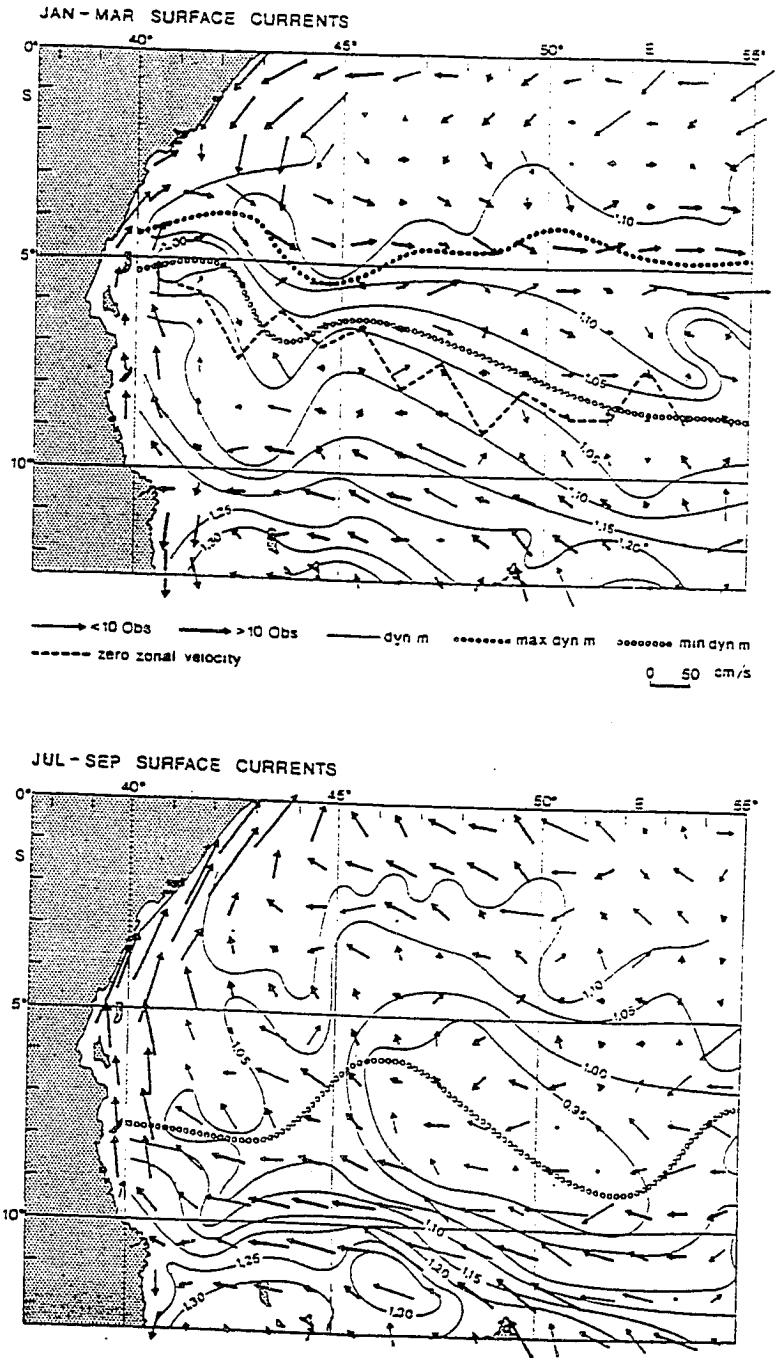

Figure 4: Climatological mean surface currents and geopotential topography relative to 500 dbar for (a) January, February and March, and (b) for July, August and September in the western Indian ocean (after Swallow et al. [1991]).

Several interesting questions arise from these studies and that of Johns et al. [1990]. What is the spatial extent of these oscillations? Where is their origin? Is it in the interior of the basin or is it near the western boundary? What is their nature; are they baroclinic Rossby waves as suggested? And finally what are the governing dynamics of the oscillations? To adequately answer these questions, information is required over temporal and spatial scales currently available only from numerical models. Consequently, the low viscosity CME general circulation model, which represents one of the most realistic calculations to date, was chosen in this study to help find answers to these questions. The model is based on the primitive equation model developed at the NOAA Geophysical Fluid Dynamics Laboratory by Byran [1969] and Cox [1984].

The thesis is organized in the following manner. A review of the relevant literature is presented in the second chapter. The details of the CME simulation and the methodology, which involves model field selection and validation, are found in the third and fourth chapters, respectively. Since the main objectives of this thesis are to describe and determine the nature and cause of the 50-day oscillations in the CME model, the subsections of Chapter 5 reflect these goals. A discussion of the dynamics of the oscillations is found in Chapter 6. As well, the findings from this study are related to previous studies performed by other investigators and their importance discussed. The summary and conclusions are found in Chapter 7.

2 Background

To obtain answers to the research questions posed in the previous section, it is necessary to understand the climatology and dominant scales of variability in the western tropical Atlantic. Hence, findings from several large observational programs conducted in the region are reviewed. The region is characteristed by a strong seasonal change in the current regime; the NBC retroflects to form the eastern arm of the meandering NECC during boreal summer and fall. Since the occurrence of 50-day oscillations will be shown to be dependent upon this seasonal cycle, the dynamics of the area will also be discussed here.

The surface circulation of the tropical Atlantic Ocean is characterized by the afore-mentioned seasonal cycle. Our knowledge of the changes in the surface circulation associated with this cycle is largely based on observational studies conducted in the region during the early eighties. Particularly important were the Seasonal Response of the Equatorial Atlantic (SEQUAL) and the Programme Français Océan et Climat dans l'Atlantique (FOCAL) programs whose joint objective was the understanding and modeling of the main physical processes responsible for the redistribution of heat, mass and salt in the equatorial Atlantic [Katz, 1987]. To achieve this objective field studies were designed to observe the upper 500 m of the equatorial Atlantic for at least one annual cycle. Measurement strategies during these programs were formulated on the basis of historical ship drift velocities [Richardson and McKee, 1984], hydrographic data [Garzoli and Katz, 1983] and the GATE (GARP Atlantic Tropical Experiment) velocity measurements [Halpern, 1980].

Richardson and McKee [1984] obtained a basic knowledge of the variability of the current regime in the tropical Atlantic by analyzing ship drift data. They created monthly composites of ship drift velocity observations in the region 20°S–20°N, 10°E–70°W. These composites were grouped together to produce characteristic velocity fields for the periods August–October and February–April (Figure 5). During the former period, the eastward flowing NECC, found between 5° and 10°N, is bounded by the westward-flowing North Equatorial Current (NEC) and the northern branch of the South Equatorial Current (SEC). The southern branch of the SEC, centered at 4°S, feeds the NBC that flows northwestward along the coast of South America. Near 8°N, 50°W, it retroflects, or turns back on itself, to form the western arm of the NECC. Some small amount of the NBC has been suggested to continue towards the Caribbean [Csanady, 1990]. Flagg et al. [1986] obtained independent evidence of the NBC retroflection from current profiles collected over the continental slope off South America between 2° and 7°N. The profiles showed that the main body of the NBC current flowing northwestward along the South American coast and further offshore a coherent current toward the southeast.

During February–April, the ship drifts exhibit westward flow except in the eastern NECC (east of 20°W) and in the Guinea Current. The NBC no longer veers offshore, but continues along the coast towards the Caribbean. Richardson and McKee [1984] also calculated monthly meridional sections (20°N to 15°S) of zonal velocity in the central and western Atlantic (Figure 6). These sections show the start-up (June), development and disappearance (December) of the NECC. Meridional shifting of the currents is also observed.

Garzoli and Katz [1983], using hydrographic data, analyzed the thermal structure

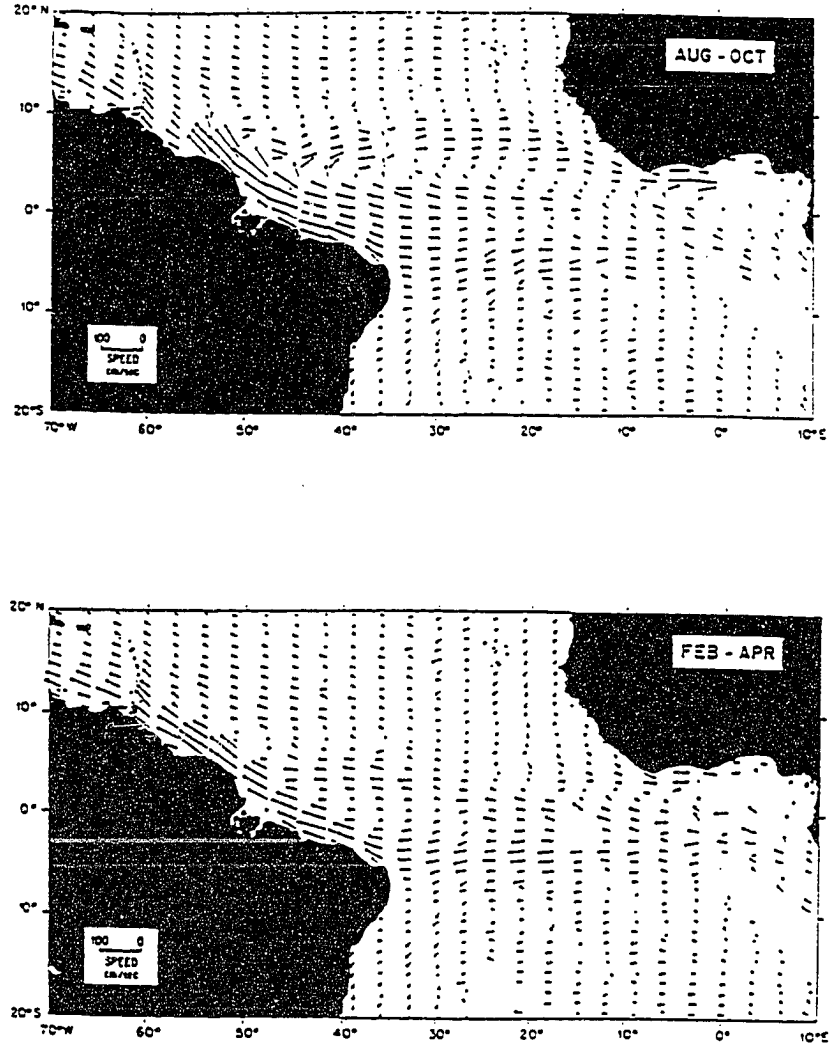

Figure 5: Maps of velocity vectors calculated from ship drift data for the three month periods August to October and February to April (after Richardson and McKee [1984]).

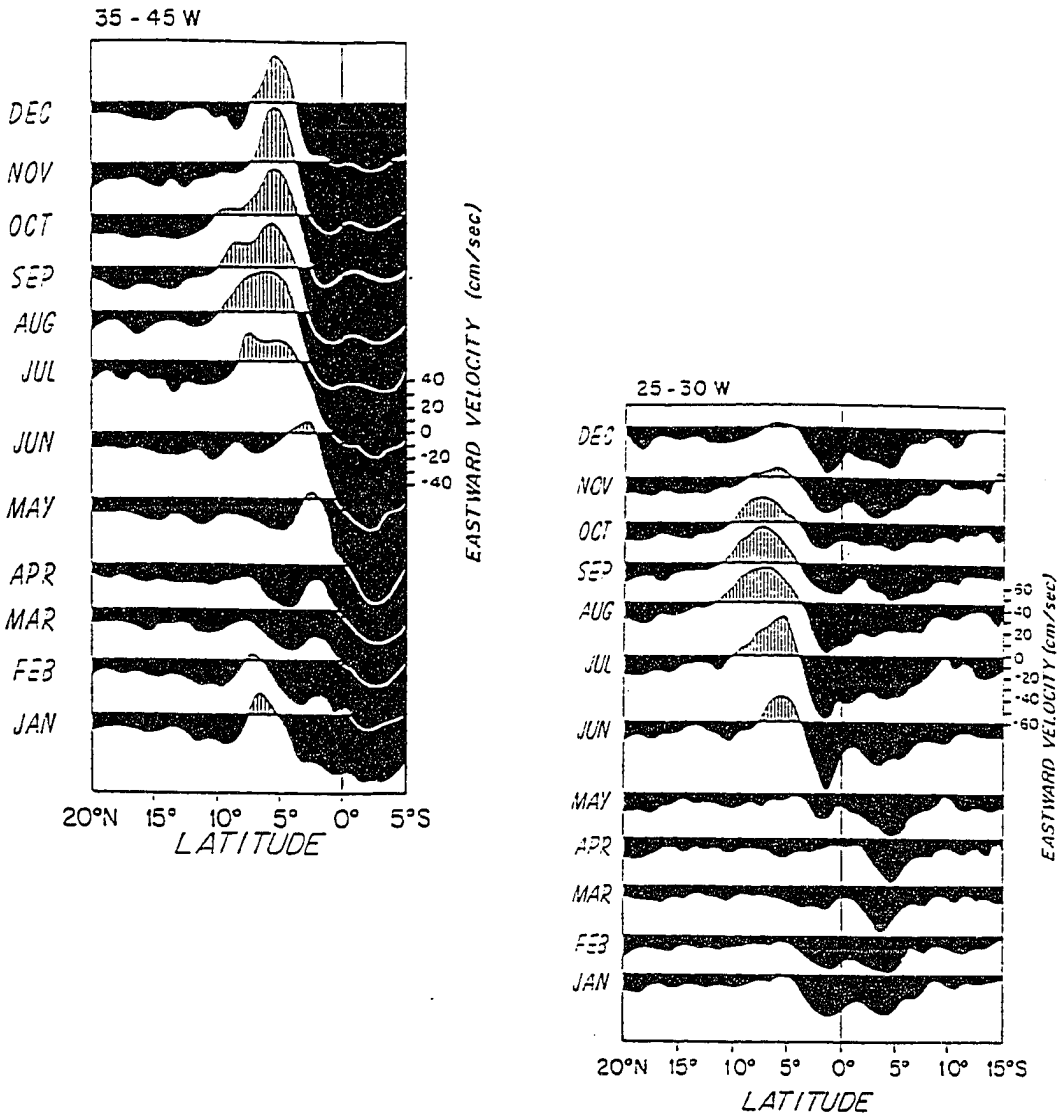

Figure 6: Monthly north-south profiles of zonal velocity in the central (25°-30°W) and western Atlantic (35°-45°W) (after Richardson and McKee [1984].)

associated with the NECC and its relation to the seasonally varying winds. They found that to the west of 25°W, the depth of the thermocline on the southern side of the NECC (4° to 7°N) oscillates annually 180° out of phase with the oscillations on the northern side (7° to 10°N). East of 25°W the thermocline rises and falls nearly in phase across the countercurrent. The western NECC occurs at the same latitude as the mean position of the intertropical convergence zone (ITCZ), which shifts north and south annually. This meridional shifting of the ITCZ is responsible for annual period variations in the curl of the wind stress which are out of phase on opposite sides of the mean position of the ITCZ and hence the NECC. Consequently, the curl of the wind stress was qualitatively correlated with the thermocline behavior in the western Atlantic.

Richardson and Reverdin [1987] released lagrangian drifters at various locations along the NECC and SEC at different times of the year during FOCAL and SEQUAL (spring, fall and NECC start-up as estimated from ship drift data) to monitor seasonal variability. Monthly composites of these buoy trajectories, smoothed with a 10-day filter, are shown in Figure 7 for the spring (March to July) of 1983 and fall (July to November) of 1984. In the spring, gradual westward advection and mesoscale fluctuations can be seen between 5° and 10°N. The start-up of the NECC is seen in late May (one buoy) and during June and July. The fall trajectories show westward flow in the South Equatorial Current (SEC), the retroflection of the NBC into the NECC, and the westward turnings of buoys from the NECC into the NEC. The NECC meanders between the retroflection region and 30°W. No buoys were observed to drift eastward after December. The waves or meanders seen in the buoy trajectories in the western NECC during fall were largest and strongest in the west, with wavelengths of 900 km, meridional displacements of 300 km, and amplitudes of meridional velocity fluctuations of 1 m s^{-1}. The trajectories suggested that

the waves propagated westwards with a phase speed of about 0.04 m s^{-1}. As the NECC decreased in speed during fall and winter, these meanders gradually shifted westward.

Information about the variability of the vertical structure of the NECC was obtained from continuously recording current meters moored for 20 months at depths from 20 to 300 m at 6°N, 28°W [Richardson and Reverdin, 1987]. This location was selected as it lies near the central equatorial Atlantic; ship drift velocities [Richardson and McKee, 1984] showed it to be near the meridional center of the Countercurrent [Richardson, 1984]. The averaged vertical profile of eastward velocity during July-August of 1984 displays velocities of 0.4 m s^{-1} near the surface decreasing to about 0.1 m s^{-1} at 300 m. March-April profiles indicate weak (<0.04 m s^{-1}) westward velocities below 20 m (Figure 8). This value is less than the standard error at 20 m for this period, $\sim$ 0.1 m s^{-1}, therefore it is not possible to determine from this data whether the NECC is present or not.

The meandering of the NECC in the western Atlantic basin is a feature observed in other western boundary current extensions such as those of the Brazil and Agulhas Currents. These meanders are considered to be long stationary waves [Campos and Olson, 1991] and were explained by Moore [1963] and Moore and Niiler [1974] as damped Rossby waves superimposed on a steady eastward flow. Recently, Campos and Olson [1991] developed an analytical model to better understand the nature and cause of these stationary waves.

Their analytical model supposes a barotropic ocean with spatially constant mean flow and Laplacian lateral dissipation. The ocean has two regions (Figure 9); a western boundary layer (Region I) and the interior region (Region II). The west-

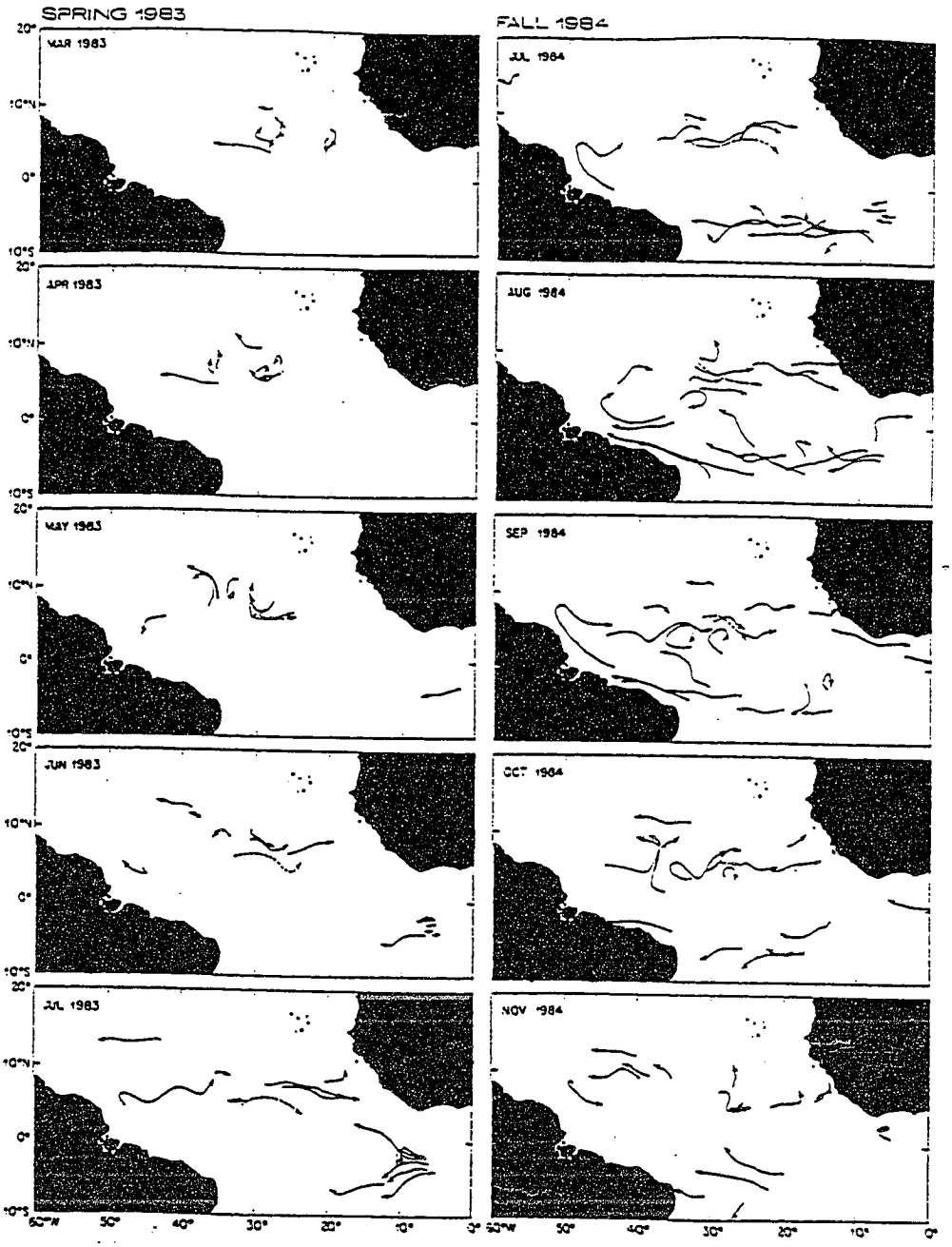

Figure 7: Monthly composites of buoy trajectories smoothed with a 20-day filter. One set is from March to July 1983 showing spring trajectories. The second set is from July to November 1984 showing fall trajectories (after Richardson and Reverdin [1987]).

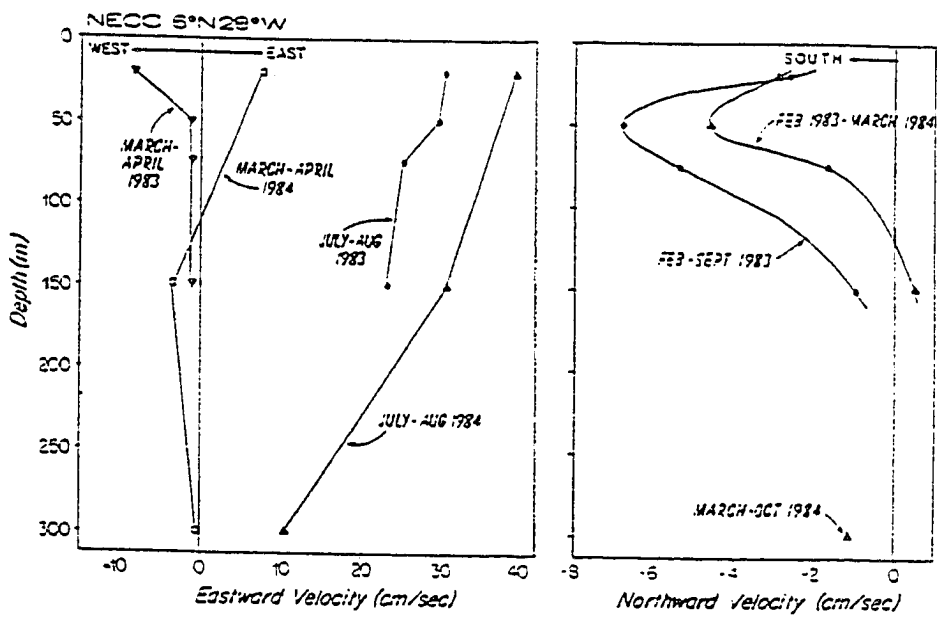

Figure 8: Vertical profiles of velocity obtained from the current meter mooring at 6°N, 28°W (after Richardson and Reverdin [1987]).

ern boundary current flows southward in Region I until it reaches the latitude of separation where it leaves the coast and enters the interior region (the model was formulated for the southern hemisphere). The dynamics of the western boundary layer or of the separation region were not considered; Region I was thought of as a black box acting as a source at the separation line. Given a source at the western boundary only waves with eastward group velocity were of interest, superimposed on an eastward zonal current. A similar model could well represent the retroflecting NBC and the meandering path of the NECC into the interior of the Atlantic basin. Campos and Olson [1991] obtained several solutions; the one of interest here contains waves with amplitude constant in time, decaying spatially. It simulates the meanders in the NECC and hence, even though the analytical model is oversimplified, it throws light on the nature of the meanders which are presumably Rossby waves with eastward group velocity. Another solution obtained by the investigators represents a wave whose amplitude is growing in time and damped in space. This solution could model eddy shedding from the retroflection region.

The dominant vorticity balance of terms for linear, baroclinic Rossby waves in the presence of a mean current, such as the NECC, is

$$\zeta_t = -\mathbf{u}_H \cdot \nabla\zeta - \beta v + f w_z$$

where ζ_t is the time change of relative vorticity, βv is the advection of planetary vorticity, $f w_z$ is the stretching of planetary vorticity and $\mathbf{u}_H \cdot \nabla\zeta$ is the advection of relative vorticity by a mean current [LeBlond and Mysak, 1978]. In the absence of a mean current, the balance is

$$\zeta_t = -\beta v + f w_z$$

while the balance for nondivergent, barotropic Rossby waves is [LeBlond and Mysak,

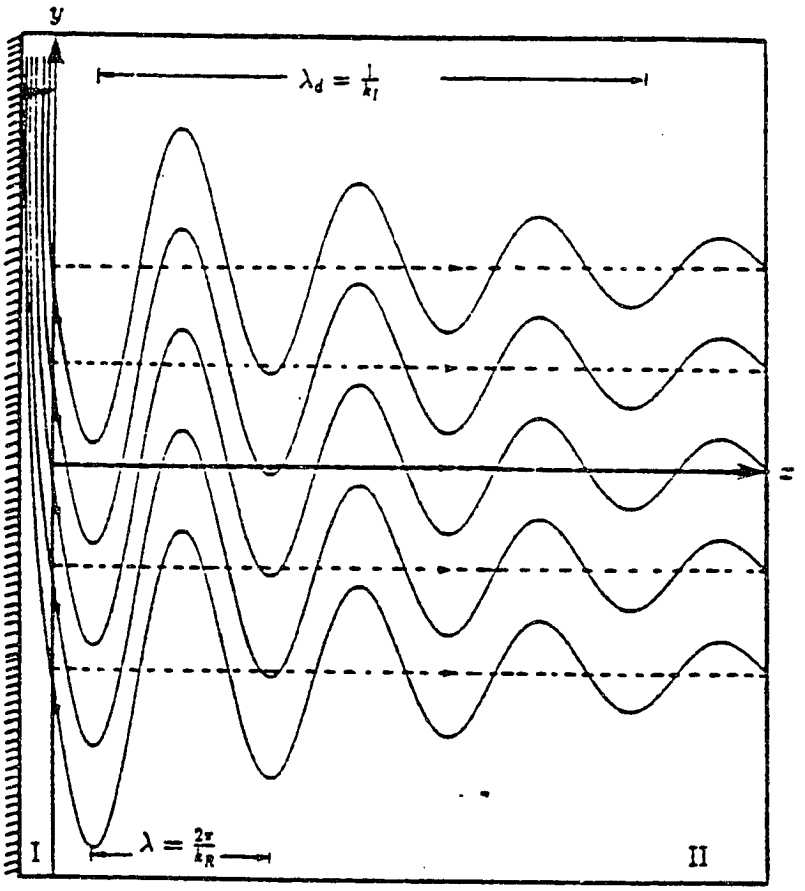

Figure 9: Schematics of the physical problem. The oceanic basin is divided into two regions: (I) the western boundary layer and (II) the interior. λ is the wavelength and λ_d is the distance in which the wave amplitude decays by a factor e^{-1}. Solutions consisting of an eastward zonal current and Rossby waves with eastward group velocity are illustrated (after Campos and Olson [1991]).

$$\zeta_t = -\beta v$$

Garzoli and Katz [1983], in an effort to quantify the observed correlation between wind stress curl and thermocline behavior discussed earlier in this section, calculated each of the terms in the vorticity equation. The vorticity equation, however, was derived from the equations for a wind-forced, reduced-gravity linear transport model. The terms were calculated from hydrographic and wind data collected over a one year period in the basin interior (42° to 22°W, 3° to 9°N). The dominant balance of terms was

$$H_0 f W_z - H_0 \beta V = -\nabla \times \tau / f \rho_0$$

where $\nabla \times \tau / f \rho_0$ is the wind stress curl, $H_0 f W_z$ is the depth-averaged stretching of planetary vorticity and $H_0 \beta V$ is the depth-averaged advection of planetary vorticity. Here, U and V denote the depth-averaged current in the upper layer, W_z is the depth-averaged vertical velocity gradient and H_0 is the depth of the thermocline. This is a forced, simplified version of the vorticity balance shown above for baroclinic Rossby waves. It can be rewritten as

$$h_t - C_{px} h_x = -\nabla \times \tau / f \rho_0$$

where $C_{px} = \beta g' H_0 / f^2$ is the phase speed of propagation and h is the mean depth of the thermocline. This can be interpreted in the following manner; in a frame of reference moving westward with C_{px}, $\nabla \times \tau \rho_0$ equals $-f dh/dt$. In other words, the effect of the wind stress curl, which is to decrease the thermocline depth, moves westward with C_{px}. The thermocline depth will increase if the wind stress curl is negative. Garzoli and Katz [1983] found this balance to hold over an annual period, hence the annual cycle of the thermocline topography is in balance with the annual cycle of the wind stress curl. The reversal of the curl of the wind stress in

the western basin is, therefore, responsible for the pressure field accompanying the reversal of the NECC. A similar diagnostic vorticity analysis was used in this thesis to investigate the nature and dynamics of 50-day oscillations. Since these analyses require large amounts of information in both space and time, output from the CME general circulation model was used to carry out this study.

3 CME Simulation

The numerical simulation used in this thesis is a three dimensional, high resolution model of the wind-driven and thermohaline circulation of the North Atlantic developed by Bryan and Holland [1989] as the Community Modeling Effort (CME) for the World Ocean Experiment (WOCE). It is based on the primitive equation model developed at the NOAA Geophysical Fluid Dynamics Laboratory by Bryan [1969] and Cox [1984]. The primitive equations are solved using a second-order finite difference scheme on the Arakawa B-grid and conserve total heat content, mass, energy and tracer variance in the absence of explicit dissipation and forcing [Bryan and Holland, 1989]. The form of the model equations and the parameterizations developed for this experiment have been summarized by Spall [1990].

The model domain extends from 15°S to 65°N and from 100°W to 14°E. The horizontal resolution is 1/3° in latitude and 2/5° in longitude, giving equal grid spacing in the north-south and east-west directions of 37 km at 34°N. This is about equal to the first internal Rossby radius of deformation at mid-latitudes, hence the resolution is just adequate to represent many of the eddy processes. There are 30 discrete vertical levels distributed over a maximum depth of 5500 m. The vertical spacing is nonuniform with a minimum of 35 m at the surface which increases to 250 m below 1000 m. Bottom topography is derived from a digital terrain data set with 5′ latitude-longitude resolution. All single grid point bathymetric features have been removed and the Florida Channel has been deepened so that the cross-sectional area of the channel is equal to the true value. Cuba and Hispañola are treated as true

islands while shallow banks represent other islands. The Caribbean Sea and the Gulf of Mexico, but not the Mediterranean Sea, are included in the model domain. The model domain and bathymetry are seen in Figure 10.

The model was initialized at rest using the January temperature and salinity fields of Levitus [1982] and integrated for 25 years. Surface wind forcing is taken from the monthly mean winds derived by Hellerman and Rosenstein [1983]. The surface heat flux is calculated from a bulk formula [Han, 1984] as a function of the difference between the model-predicted temperature and a prescribed atmospheric temperature. The time scale of the surface heat flux is on the order of 50 days [Spall, 1990], and depends on the latitude, longitude, time of year and surface temperature. The surface salinity is relaxed towards Levitus [1982] climatology also with a time scale of 50 days. Linear interpolation between monthly and seasonal means is used to obtain necessary values for all surface forcing fields at each model time step. Model output fields were saved every three days.

Two CME simulations were calculated using different parameterizations of the subgridscale mixing processes. Fields from the first experiment (start of year 20) were used as initial conditions for the second experiment which was run for five more years. In the first experiment (CME1), lateral friction was represented by a biharmonic operator with a coefficient of -2.5 $\times$ 10^{11} m^4s^{-1} for both momentum and tracers [Bryan and Holland, 1989]. The vertical dissipation mechanism is a second order operator with constant coefficients of 3.0 $\times$ 10^{-3} m^2s^{-1} for momentum and 3.0 $\times$ 10^{-5} m^2s^{-1} for tracers. In the second simulation (CME2), the biharmonic friction was reduced by a factor of 2.5 and vertical momentum mixing was reduced by a factor of 3. Additional dissipation of momentum was provided in both cases by a quadratic bottom drag. A Kraus-Turner [1967] type surface mixed layer was

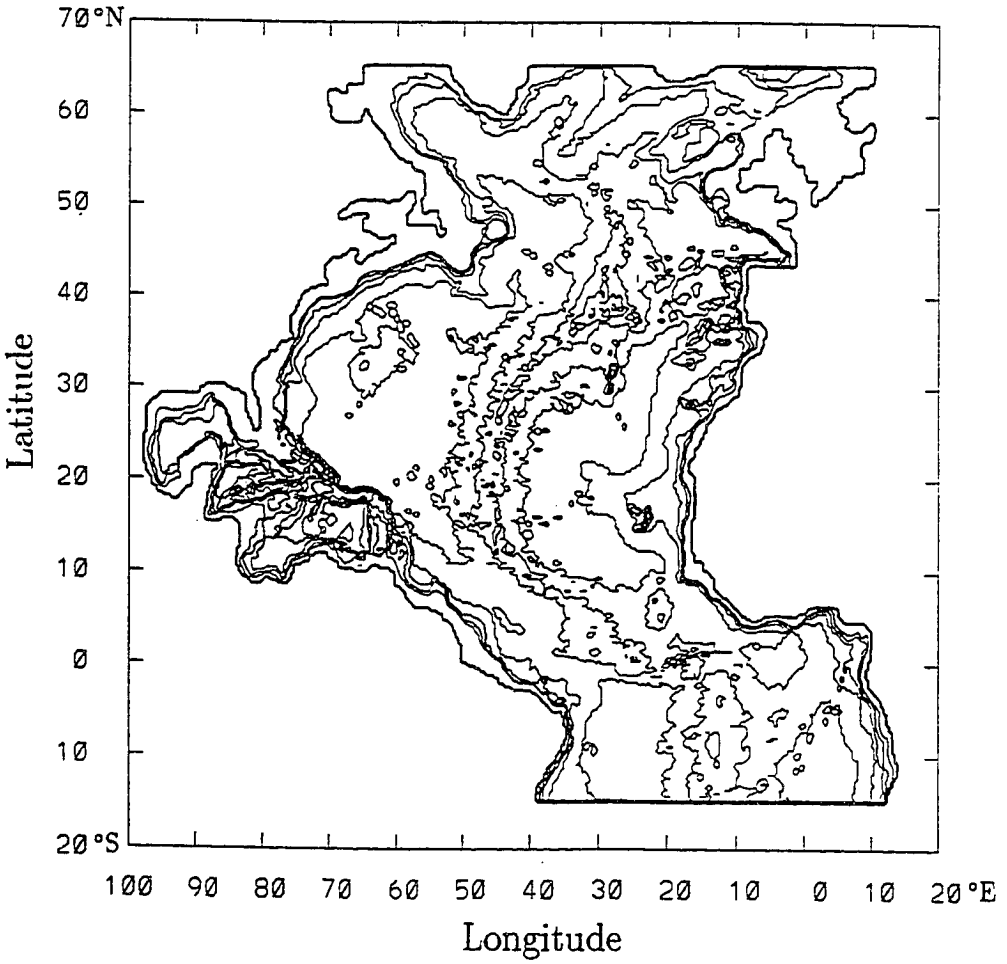

Figure 10: CME model domain and bathymetry

included at the top of the model. A conventional adjustment scheme was used to treat free convective mixing [Bryan and Holland, 1989].

The boundaries in the northern and southern ends of the domain are closed to any inflow or outflow. The mean effect of wind and thermohaline forcing from the rest of the world oceans is parameterized by "sponge" layers which lie adjacent to the boundaries and extend 5 grid points into the model interior. Within these sponges the temperature and salinity fields are forced back toward Levitus' monthly mean values by Newtonian damping. The damping terms are thought to provide some of the effects of interbasin exchange of water masses as well as suppressing the reflection and generation of waves at the boundaries. The Mediterranean outflow and the Labrador Sea were treated in a similar fashion. There is no explicit flow through the Straits of Gibraltar, however water parcels leaving the damping region will take on the properties characteristic of the climatological temperature and salinity field in this region. The damping in the Labrador Sea is required to maintain realistic sea temperatures over the shelf where there is extreme cooling to the atmosphere [Spall, 1990]. One passive tracer, age, has been included in the model. It is set to zero at the model surface and increases linearly with time in the interior. It can be used as a nonconservative tracer of water masses.

Validation studies were performed on the output from several different CME calculations [Bryan and Holland, 1989; Schott and Böning, 1991; Treguier, 1992]. Schott and Böning [1991] considered fields from CME1 and a version where the vertical diffusion coefficient was reduced by a factor of three. The horizontal diffusion was the same as in CME1. This simulation was designated IFM-HR. The output from IFM-HR to be discussed shortly varies little from the output obtained from CME2, whose horizontal diffusion was also reduced by a factor of three. Hence,

the results reviewed here can be equally applied to CME2, which is the version of the model chosen for use in this thesis. This version was selected since the velocity fields in the equatorial region were shown to be more realistic in the equatorial region than those from CME1 [Schott and Böning, 1991]. Since fields from the tropics were required for this study, CME2 was an appropriate choice. Other details regarding CME1 are included for completeness.

Bryan and Holland [1989] found that the CME1 solution had little drift in the basic hydrographic structure away from that described by the initial conditions. The difference between the mean sea surface temperature (SST) for January over the last 15 years of the simulation and the Levitus [1982] climatology is less than 1°C over most of the basin. The largest differences were found on the inshore side of the Gulf Stream. They conclude that the surface heat flux and mixed layer parameterizations in the model are reasonably accurate. The Gulf Stream, however, is not seen to separate from the coast at Cape Hatteras. Instead, it follows the coast for several hundred kilometers further north where the separation is dominated by a very tight and nearly stationary anticyclonic gyre that is totally unrealistic. The causes for this anomaly are not understood. South of Cape Hatteras, the simulation is much more realistic. The mean barotropic transport is about 50×10^6 m^3 s^{-1} just south of Cape Hatteras, the core of the North Atlantic Deep Water is found between 2000 and 3000 m depth and a coherent deep western boundary current is found south of Cape Hatteras. The amplitude and phase of the variability of the volume transport through the Straits of Florida agree well with observations [Bryan and Holland, 1989]. A maximum in summer and a minimum in fall are seen in the model values.

Treguier [1992] found that the eddy kinetic eddy (EKE) distribution in CME2

shows a good agreement with observations in the western Atlantic but a deficit in the eastern Atlantic. The representation of the bottom topography and the absence of high frequency wind variability may be partially responsible for this low eddy activity, but the main cause is the low level of instability in the model arising from the coarse horizontal model resolution.

Schott and Böning [1991] have evaluated the upper layer circulation in the western equatorial region of the CME model. The models considered are CME1 and IFM-HR. The Equatorial Undercurrent (EUC) in CME1 does not penetrate far enough eastward; the core speed is only 0.3 m s^{-1} at 30°W in February. Speeds greater than 0.60 m s^{-1} have been reported in the real EUC core at 1°E in February 1984 [Hénin et al. 1986]. In the less viscous IFM-HR solution the core speeds are 0.90 m s^{-1} at 30°W, suggesting that IFM-HR better represents the equatorial currents. The EUC, however, surfaces in the west during winter in IFM-HR, pushing apart the westward surface flow of the SEC with a band of eastward surface currents (Figure 11c). Surfacing of the undercurrent has been observed by Katz et al. [1981] in current profiling sections collected during October, February and March. Eastward flow has also been seen by Weisberg et al. [1987] in current meter measurements collected at 10-m depth. In the temperature section along the equator from IFM-HR during August, the thermocline slants upward and eastward as in the real ocean, however the thermocline is too diffuse in comparison with observed temperatures. This deficiency is attributed to the constant vertical eddy diffusion coefficient.

The main features of the surface currents as revealed by observational studies [Richardson and McKee, 1984; Richardson and Reverdin, 1987] in the equatorial region have been reproduced in both models. Current vectors from the upper layer

(17.5 m) of IFM-HR from August (Figure 11a) and February (Figure 11c) show that the details and seasonality of the current regime as revealed by observations have been captured in this region of the model. In August, the southern branch of the SEC (SSEC) found between 3°S and 5°S, feeds into the cross-equatorial NBC which, in turn, retroflects into the meandering NECC. This pattern develops in early June and continues until December when the meanders start to break down. In February the SSEC inflow is present but weaker. North of 2°N, the flow is disorganized but generally westward. At the undercurrent level (133 m), the cross-equatorial flow out of the SSEC turns into the EUC in August (Figure 11b), while an equatorward undercurrent off Guiana flows into the NECC. In February (Figure 11d), equatorward current flows into the Equatorial Undercurrent (EUC).

The zonal currents at 30°W between 5°S and 15°N from CME1 (NCAR) and IFM-HR, are found in Figures 12a and b for August and February, respectively. During August all model solutions display the eastward flow of the NECC between 3° and 10°. IFM-HR show bands of eastward flow with a narrow jet on the southern edge of the NECC (3°N) and a wider core at about 6°N. The narrow core is the meandering jet seen in Figure 12a. These meanders remain stable during August through December. Meandering of the NECC has been reported by Richardson and Reverdin [1987]. The penetration of the jet far into the interior, however, is not considered to be realistic. Two separate NECC cores have occasionally been observed in the real ocean [Hénin and Hisard, 1987]. Geosat altimetry data confirm the double peak structure of the NECC with cores occurring at 5°N and 9°N during fall [Didden and Schott, 1992]. Their occurrence in IFM-HR is considered to be a result of the reduced vertical friction parameterization. During February, the currents are generally to the west (Figure 12b), in agreement with observations [Richardson and Reverdin, 1987]. Finally, it should be noted the annual mean

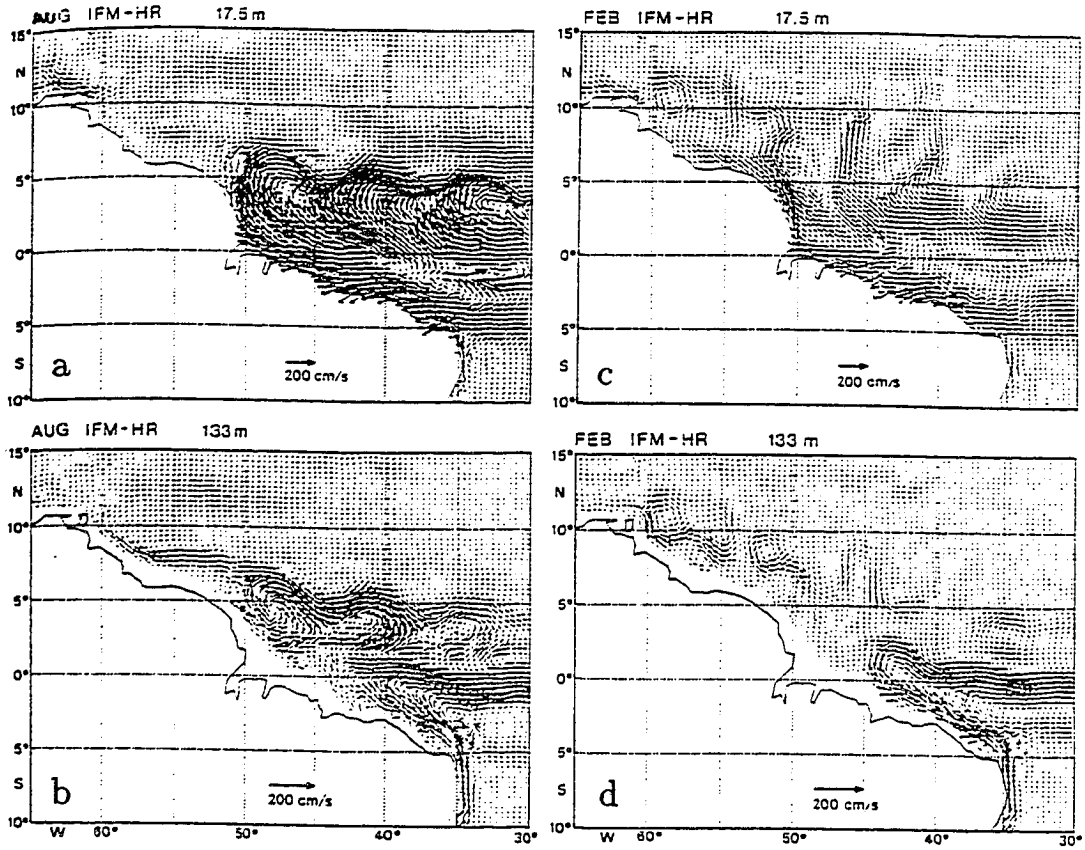

Figure 11: Currents in the IFM-HR model at the (a) surface (17.5 m) and at (b) 133 m in August and at (c) 17.5 m and (d) 133 m during February (after Schott and Böning [1991]).

throughflow from the southern hemisphere into the Caribbean along the western boundary is small in the model. There is no enhanced throughflow in winter when the NBC is not retroflecting into the NECC.

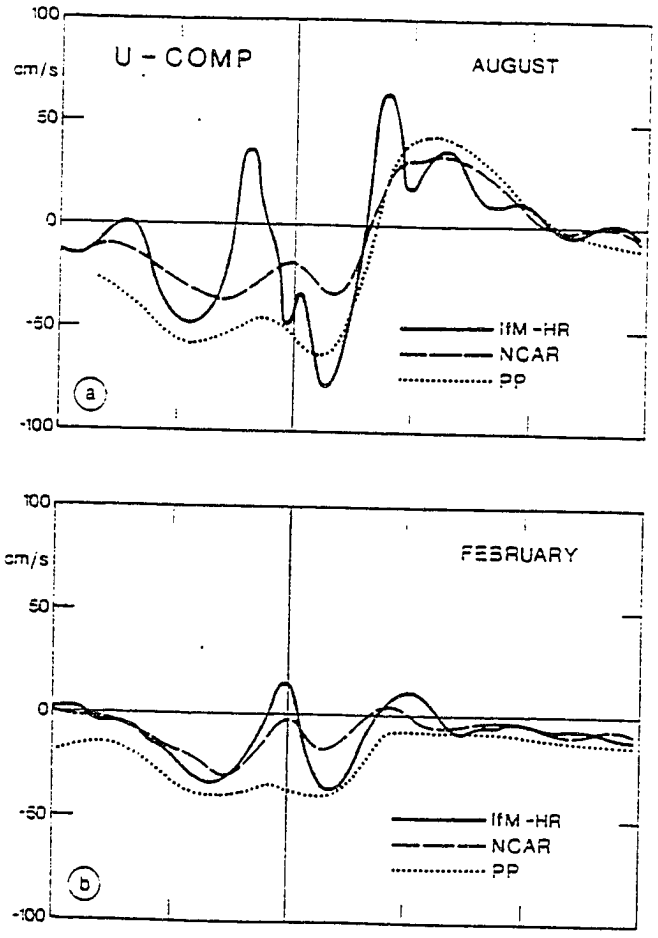

Figure 12: Zonal surface currents at 30°W, 5°S-15°N from ship drifts and three models, IFM-HR, NCAR and PP (this latter model is not discussed in the text) in (a) August and (b) February (after Schott and Böning [1991]).

4 Methods

4.1 Model Field Selection

To carry out the descriptive part of this study, it was necessary to extract the subset of the CME2 solution that was likely to contain the signature of the 50-day oscillations. Obtaining a model subset also allowed easier manipulation of the model fields. The following choices were made to ensure that the oscillation signal was adequately represented in the extracted fields. The tropical region of the model extending from 5°S to 15°N and 60°W to 5°E was chosen as the domain of the extracted fields. The last 256 realizations of the CME2 solution were retrieved to ensure that several oscillation cycles were resolved. These snapshots served as the population underlying the statistical analyses discussed in the following chapter. The time interval between each model realization is three days, hence a little over two years (779 days) of the solution was extracted.

The zonal wavelength of the 50-day oscillations discussed in the Introduction was 520 km with a range of 390-740 km. To check that these oscillations were adequately resolved in the model, the shortest wavelength obtained with a longitudinal grid spacing (Δx) of 0.4° (about 40 km) was calculated from the wavenumber at the Nyquist limit

$$\lambda_{min} = \frac{1}{k_{max}} = \frac{\Delta x}{\pi}$$

It was found to be about 14 km; an order of magnitude smaller than the observed wavelengths. I then sub-sampled this grid, giving a longitudinal spacing of 1.2° (about 120 km). Five grid points (600 km) over the zonal wavelength are required

to represent a wave, so wavelengths of about the size of the 50-day oscillations will be seen with this grid spacing. The latitudinal spacing is that of the model solution (1/3°). The meridional structure of the oscillation will be resolved since the internal Rossby radius of deformation in this region is about 120 km [Emery et al. 1984]. As noted in the Introduction, the signature of the 50-day oscillations was found to be strongest in the surface waters, hence the top eight levels (upper 400 km) of the CME2 solution were extracted. The variables obtained were temperature, salinity, zonal and meridional velocity and vertical velocity. This subset will be known as CME2E in the following discussion.

The zonal and meridional velocities were depth-averaged over the surface layer of CME2E. For the purposes of this study, the surface layer is defined as the layer between the 23°C isotherm and the free surface. Boyd [1986] categorized the flow in the upper kilometer of the water column in the western tropical Atlantic into four regions. Using mean temperature and salinity (T/S) curves for this area [Emery and Dewar, 1982], she chose the surface layer to lie between the 23°C and 27°C isotherms (Figure 13), which corresponds, in the western basin, to water depths between 0 and 80 m. The CME2 T/S relationships in this region will shortly be shown to be similar to those obtained by Emery and Dewar [1982], hence it is reasonable to define the CME2E surface layer in the same manner. In CME2E, the mean position of the 23°C isotherm shallows towards the east; it is found at about 110 m at 50°W and 80 m at 35°W. Hence, three vertical grid points were used when depth-averaging in the western basin and two points in the interior. All velocity fields discussed below are depth-averaged unless otherwise stated.

Emery and Dewar [1982] computed annual mean T/S relationships for 5° squares in the Atlantic ocean. Figure 14 shows their T/S relationship for the region west of

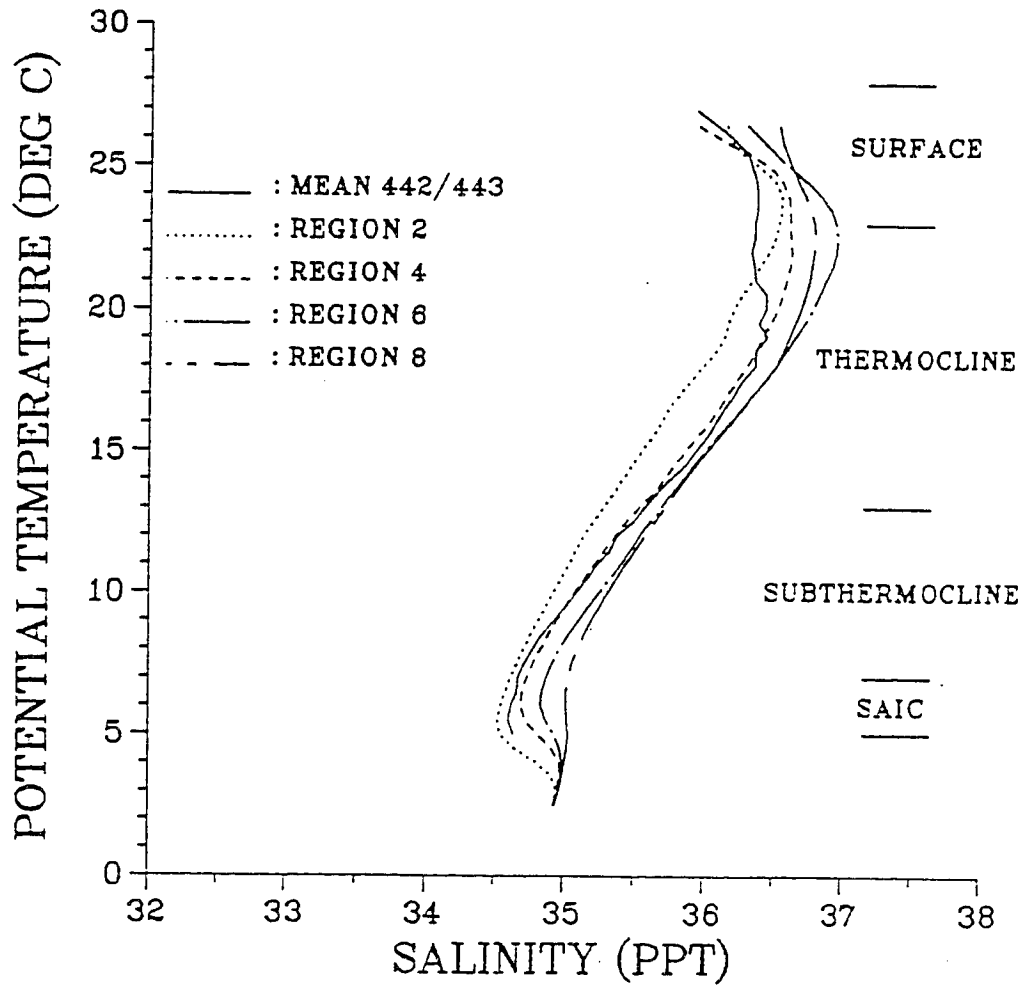

Figure 13: Typical potential temperature-salinity relationships for the northern hemisphere western tropical region and the four classifications in the upper 1 km of the water column. The curves representing regions 2, 4, 6 and 8 are from Emery and Dewar [1982]. The other curve is not relevant to this study (after Boyd [1986]).

40°W between 5° and 15°N and that from CME2 between the coast of Brazil and 40°W along 7.5°N. I obtained the latter relationship by averaging monthly averaged temperature and salinity fields which, in turn, were monthly averages from the last five years of the simulation. I plotted all the temporally averaged T/S points along 7.5°N between Brazil and 40°W, hence an envelope of values can be seen in the deeper layers. The two relationships largely agree, although the CME2 surface water is slightly cooler and fresher than the observed surface layer T/S points.

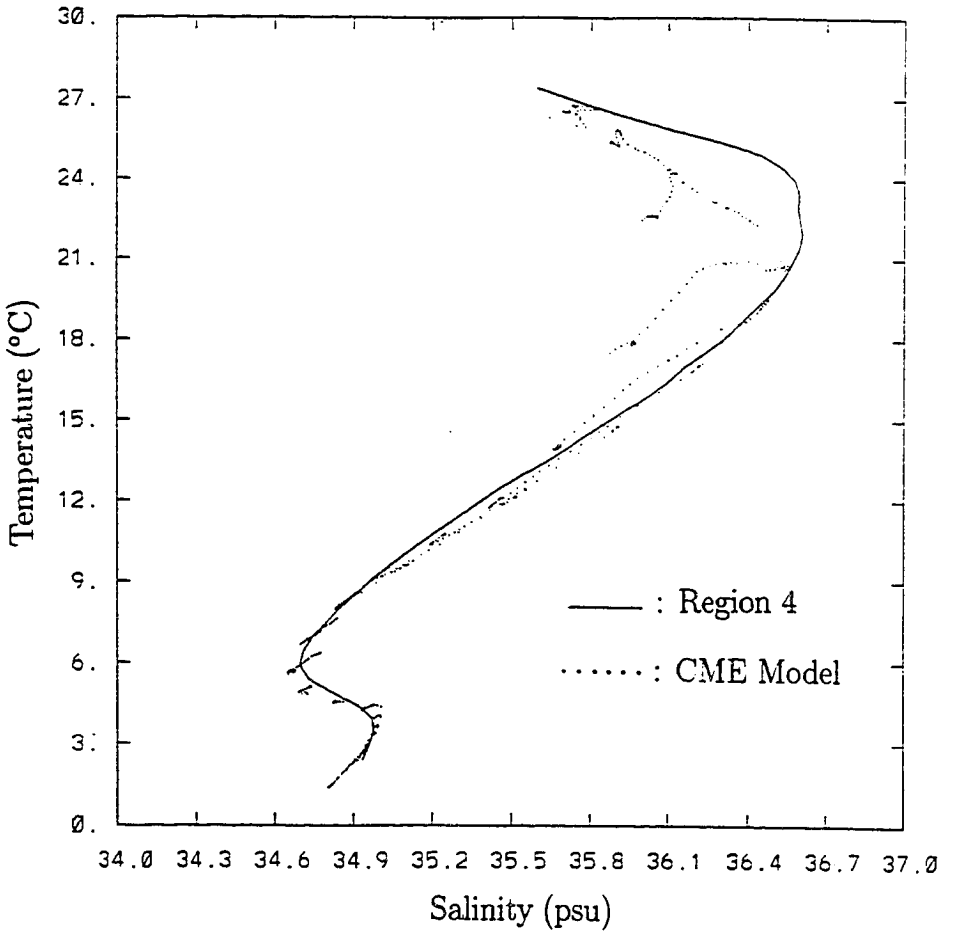

Figure 14: Annual mean potential temperature-salinity relationships from Region 4 from Emery and Dewar [1982] and from 7.5°N between Brazil and 40°W in CME2

4.2 Model Validation

To verify that the CME2E velocities adequately represent the surface circulation of the real western Atlantic tropics, these velocity fields were compared with the surface layer flow discussed by Boyd [1986]. She constructed a synthesis of the surface circulation based on observations up to 1986. Figure 15 shows a schematic of these currents during fall. It displays the flow details discussed earlier; the SEC feeding into the NBC, which retroflects into the NECC. The Demerara Anticyclone, seen at 50°W, 9°N, was reported by Bruce et al. [1985] to be a semi-permanent feature of the region. Johns et al. [1990] since questioned this idea on the basis on their observational findings. As noted by Schott and Böning [1991] this feature is not present in the CME fields.

In order to compare the CME2E velocities with the flow features described by Boyd [1986], it was necessary to average the CME2E velocities over the time interval represented in the schematic. For the purposes of this study, this interval will be called the retroflection period. The remaining time during the year will be known as the non-retroflection period. To document this annual cycle of retroflection and non-retroflection periods, monthly averaged CME2E velocity fields were examined to determine when the retroflection started and finished. They showed that it started in June and disappeared at the end of January. Consequently, all the CME2E fields over this time period were averaged to produce a flow field representative of the retroflection period (Figure 16b). The remaining fields (February through May) were averaged and are considered to represent the non-retroflection period (Figure 16a).

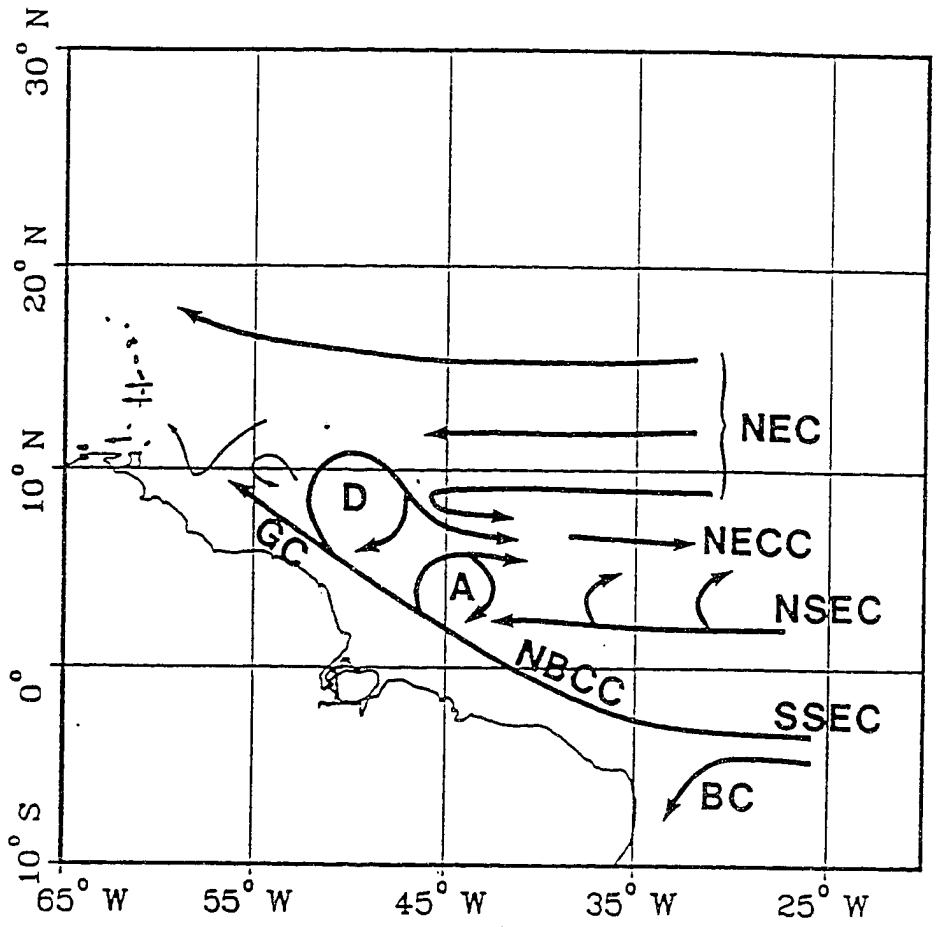

Figure 15: Major surface currents (23-27°C of the northeast coast of South America. Initials are defined as: A–Amazon Anticyclone; D–Demerara Anticyclone, NBCC–North Brazil Coastal Current (same as NBC) and BC–Brazil Currents. Remaining initials are defined in the text (after Boyd [1986]).

The flow field for the retroflection period (Figure 16b), displays many of the same features as seen in Boyd's schematic. The westward flowing SEC feeds the NBC which retroflects into a meandering NECC. The SEC, however, is split apart by the eastward directed EUC which has surfaced in the western basin. The NECC has two cores; one broad and slow, while the other appears as a jet extending across much of the basin. As discussed in the Simulation section, the appearance of two separate NECC cores has been observed in the real ocean, however their persistence over such a long period (seven months) has not been observed during the experiments reviewed in the Background section. Similarly, the eastward extent of the penetration of the NECC jet has not been observed. As also mentioned in the Simulation section, the EUC only surfaces on occasion, hence this persistent feature is unlikely to be realistic. During the non-retroflection period, westward flow appears in place of the eastward flowing NECC in the western basin (Figure 16a). The NBC flows northwestward along the coast of South America and the EUC has surfaced in the western basin, again causing the SEC to split and flow around it. The same argument applies during this period as during the retroflection period regarding the realism of the persistence of the surfaced EUC. The other features reflect the observational findings for this season discussed in the Background. Hence, these velocity fields have captured the circulation features of the real ocean as depicted by ship drift, lagrangian and current meter data collected in the region for the two periods. Some flow features, however, are unrealistic. Since the area of interest in this research is limited to the western basin, neither the surfacing of the EUC or the eastward penetration of NECC jet will impact upon this study.

For the purposes of this thesis, which concentrates on the western tropical region of the north Atlantic, the retroflection and the meandering of the NECC can be con-

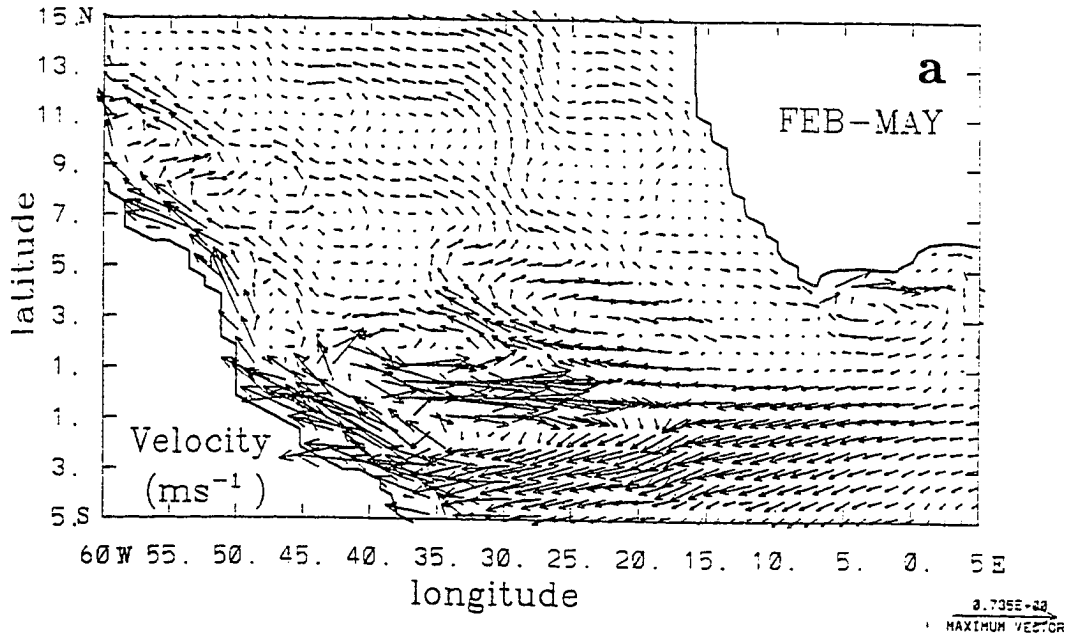

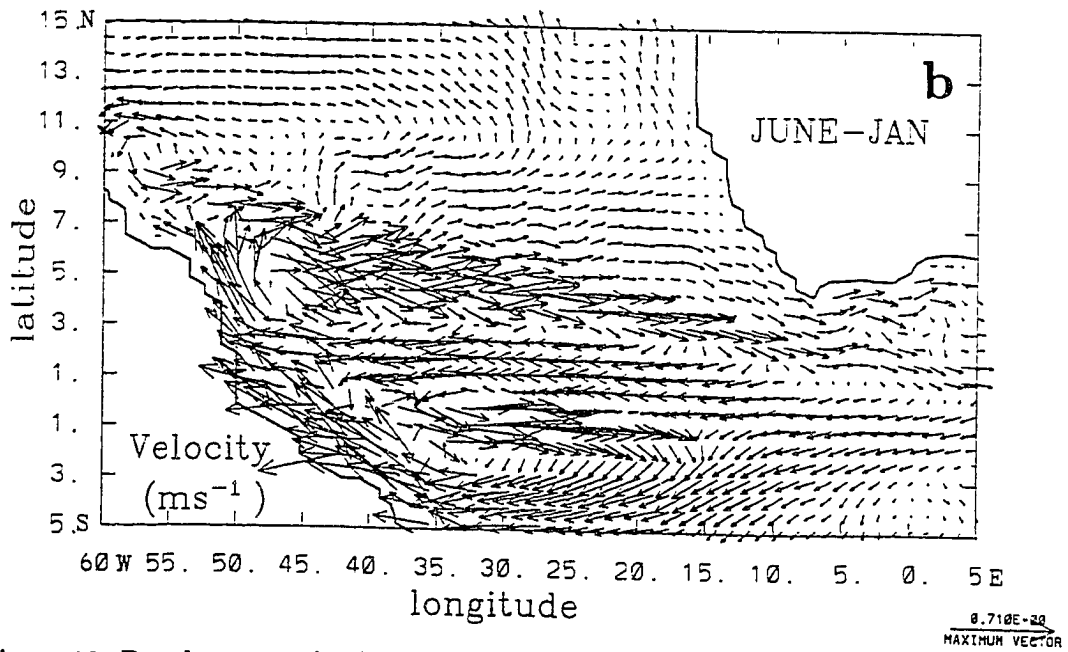

Figure 16: Depth-averaged velocity fields for (a) the non-retroflection period (February through May) and (b) the retroflection period (June through January).

sidered to be quite realistic. The wavelength of the NECC meanders in Figure 16b is about 800 km, while the eastward extent of the meandering is about 30°W. These findings agree with those reported in the Background. A comparison of CME2E and observed zonal velocities at 6°N, 28°W (Figure 8) reveal that the magnitude of the flow is very similar near the surface, however the CME2E velocities decay too quickly in the vertical. The average profile for August from CME2E (Figure 17) decreases to almost zero at 130 m, while in the real ocean it decreases to 0.3 m s^{-1} at 150 m and over the next 150 m the flow decreases linearly to 0.1 m s^{-1}. Hence, it appears from these findings that the model is reproducing the details of the surface circulation with some accuracy, but the deeper flow is inadequately simulated.

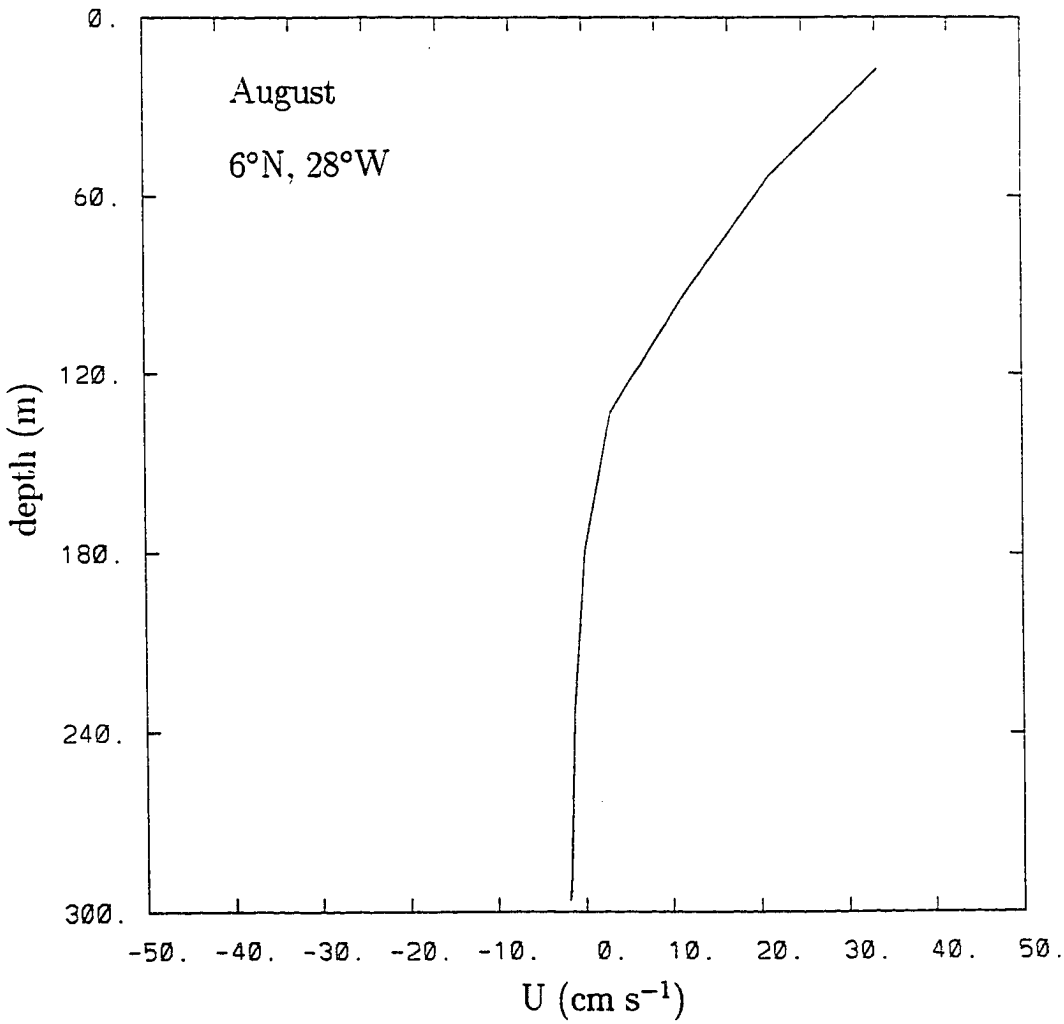

Figure 17: Vertical profile of zonal velocity at 6°N, 28°W for August from CME2

5 Results

5.1 Description of Model Flow Fields

A sequence of velocity contour snapshots, selected at monthly intervals over an annual cycle from the western tropical region of CME2E, were examined to follow the evolution and decay of major flow features. The onset and decay of the retroflection and the NECC is reflected in the zonal velocity contours (Figures 18a-30a). The meander pattern associated with the NECC during the retroflection is seen in the meridional velocity contours. As well, wave-like structures are seen in these contour fields once the NECC has slowed and disappeared (Figures 18b-30b). These waves will later be shown to be 50-day oscillations.

The sequence consisted of snapshots from the middle of each month starting in July of the second last year of the CME simulation (year 23) and finishing in the following July. Two cores of eastward flow associated with the NECC are seen in July (Figure 18a): the jet to the south and the broader slower flow to the north. The westward flow of the NEC and the northern branch of the SEC are seen to the north and south of the NECC. Alternating bands of northward and southward flow are seen in the meridional velocity contours (Figure 18b) in the region of the standing meander pattern of the NECC jet. Westward and southward flow are represented by the hatched regions and the contour interval is 10 cm s^{-1}. This pattern is repeated in August (Figures 19a and b) and September (Figures 20a and b), however the eastward flow in the NECC jet and the meridional flow associated with the meanders intensified. The meanders have penetrated further eastward. In

October (Figures 21a and b) and November (Figures 22a and b), the flow magnitudes decrease slightly in these key regions, however the patterns are largely unchanged. Pockets of westward flow appear north of the NECC jet in both months.

In December, the westward flow has formed a coherent band from the western boundary to 35°W. The speed of the eastward jet has decreased in magnitude (Figure 23a). In January, westward flow is seen across the entire basin north of the NECC jet, which has slowed considerably (Figure 24a). The alternating bands of northward and southward flow of the meander pattern have translated westwards (Figure 24b), whereas earlier these bands were stationary. By the middle of the next month, February, the eastward and westward flows are of about the same magnitude and westward flow has infiltrated most of the basin. Remnants of the eastward NECC remain (Figure 25a). The alternating bands seen in the meridional velocity contours are more pronounced in the west and are weakening in magnitude in the interior (35°W) (Figure 25b). The zonal component of flow behaves similarly in March and April (Figures 26a and 27a), while alternating bands of meridional flow are found to be weakening in the west and disappearing entirely in the interior (Figures 26b and 27b). By May, the alternating bands are no longer observed (Figure 28b) and the flow is predominantly westward (Figure 28a). In June, the NECC is seen to start up again (Figure 29a) and alternating bands of northward and southward flow are seen in the western basin(Figure 29b). By July, these meanders have penetrated into the interior (35°) and the NECC has intensified again (Figures 30a and b).

This time history of the flow in the western tropics suggests that the the meander pattern, represented by wave-like structures in the meridional velocity contours, is held stationary by the NECC during the retroflection period and then moves westward as the NECC weakens. It is also possible, however, that these displacements

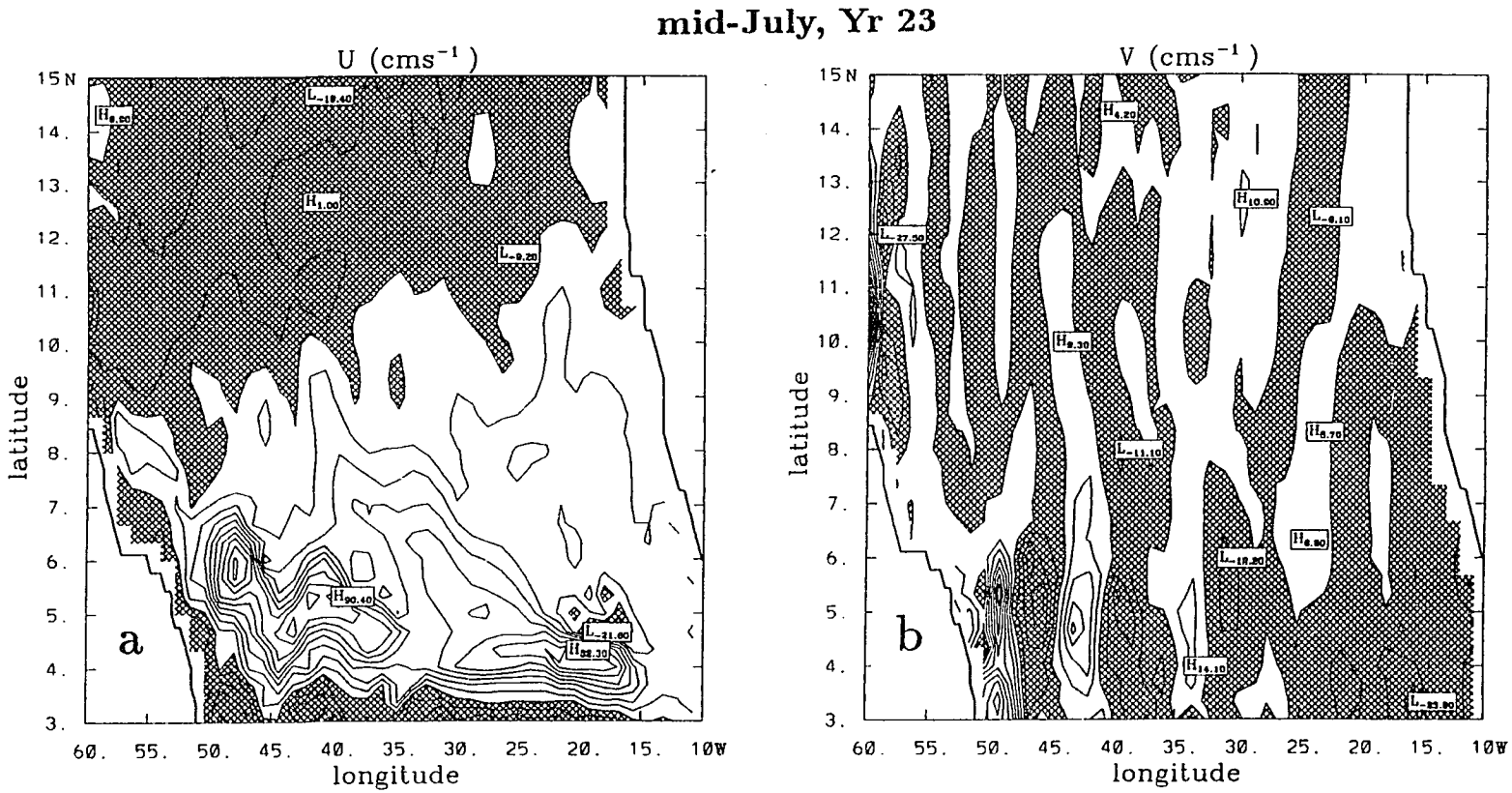

Figure 18: Contours of (a) zonal and (b) meridional velocity from mid-July in the second last year of the model. Contour interval is 10 cm s^{-1} and the hatched regions represent westward and southward flow.

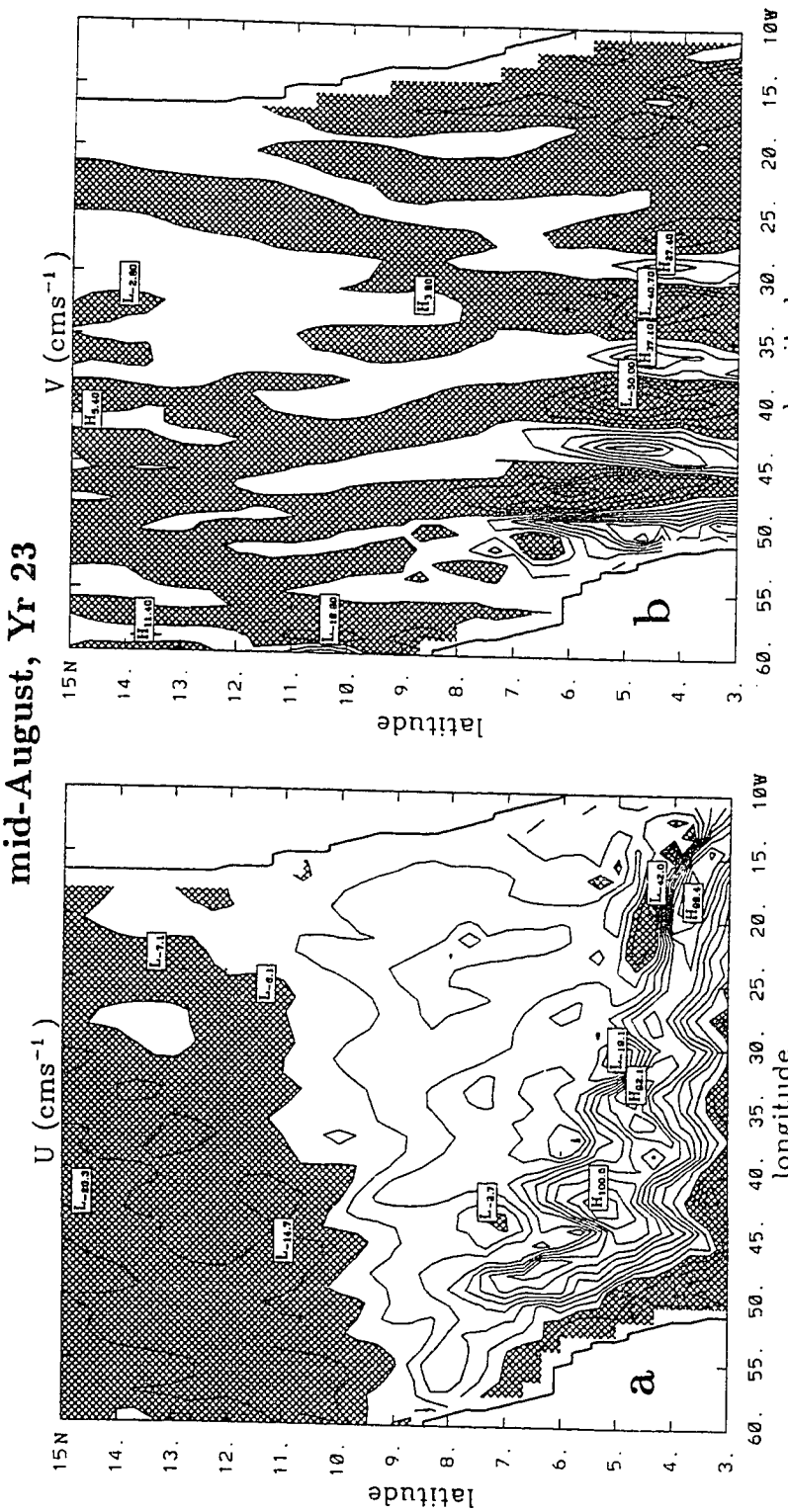

Figure 19: Same as Figure 18, but for mid-August

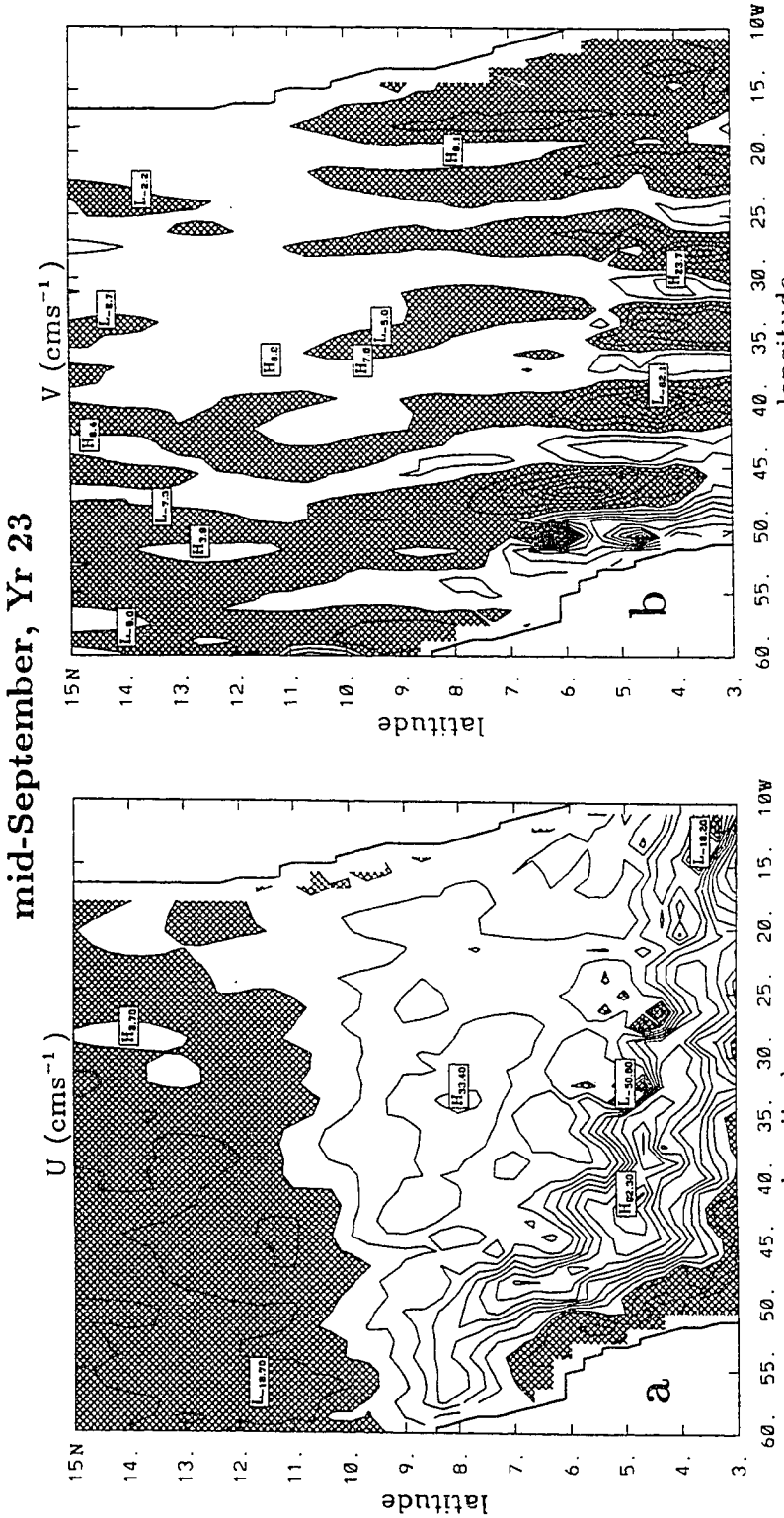

Figure 20: Same as Figure 18, but for mid-September

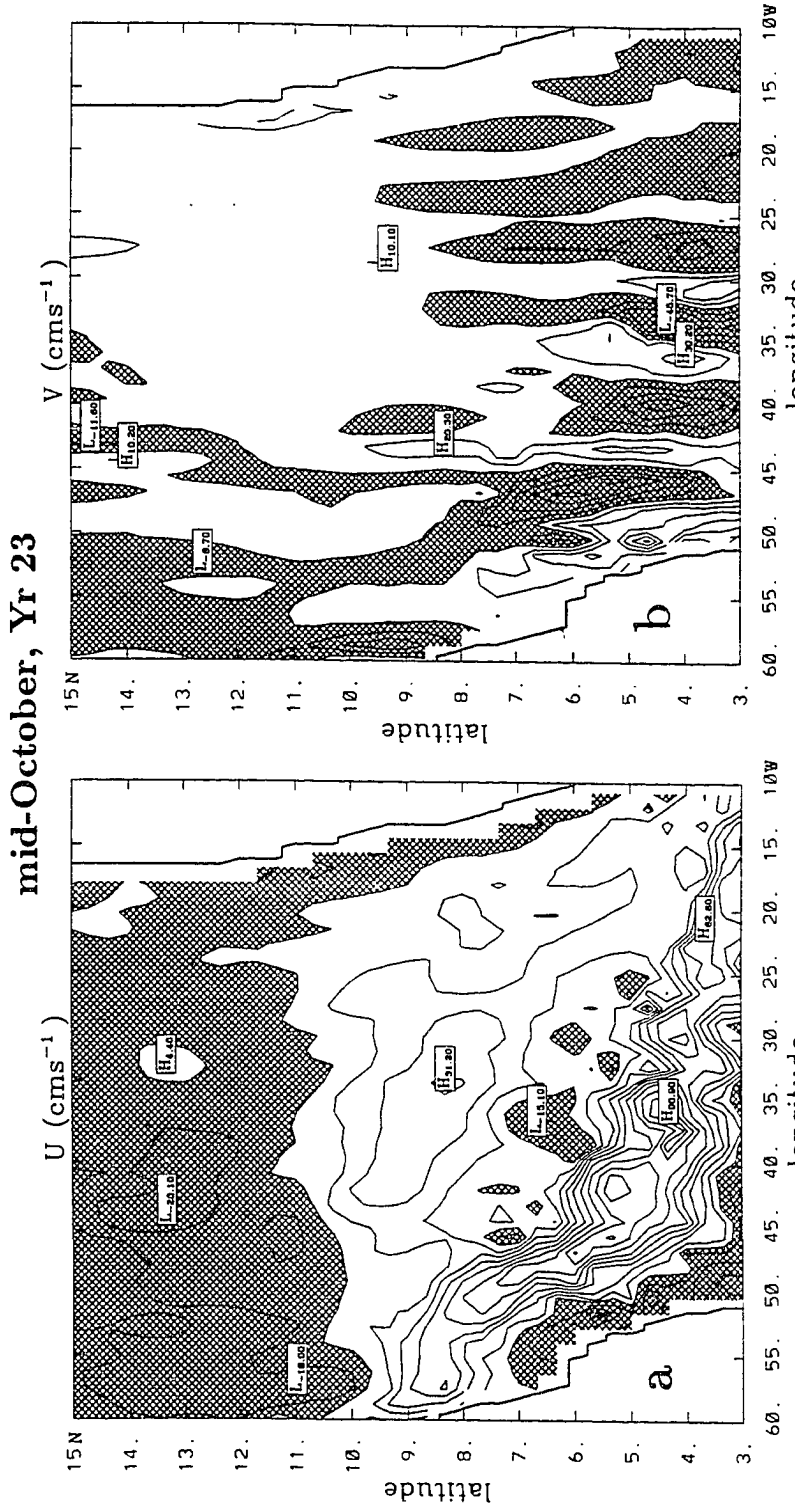

Figure 21: Same as Figure 18, but for mid-October

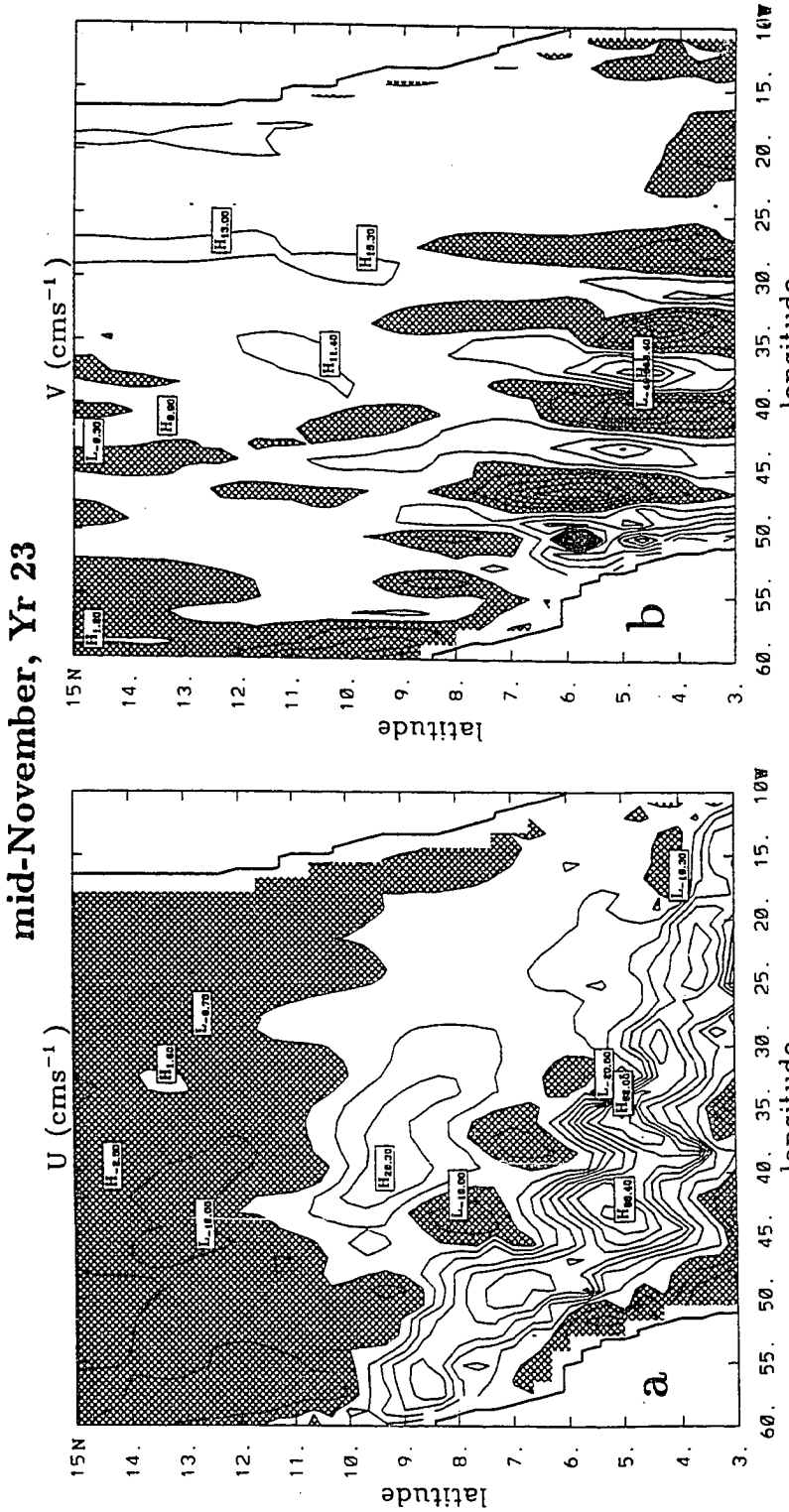

Figure 22: Same as Figure 18, but for mid-November

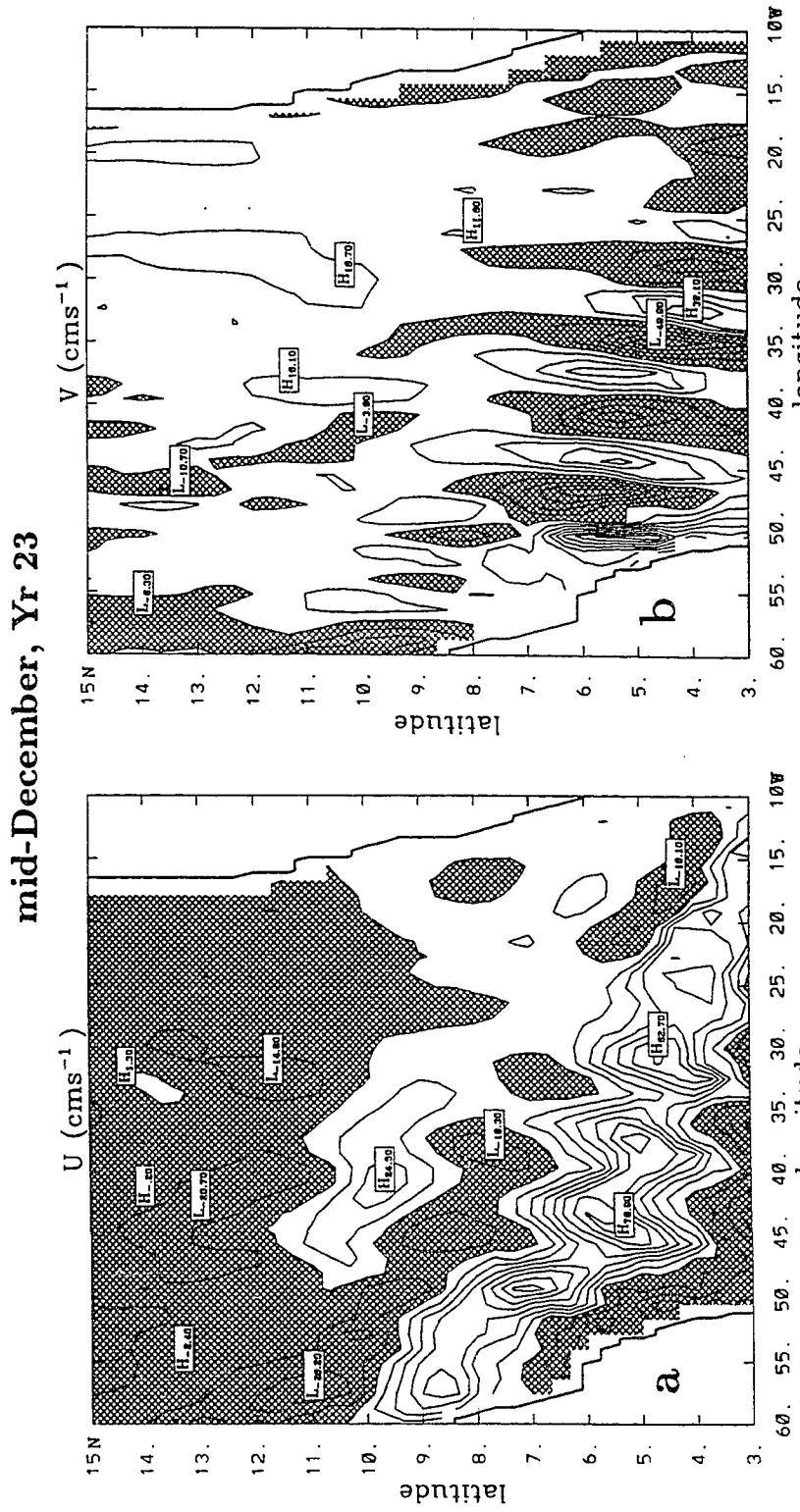

Figure 23: Same as Figure 18, but for mid-December

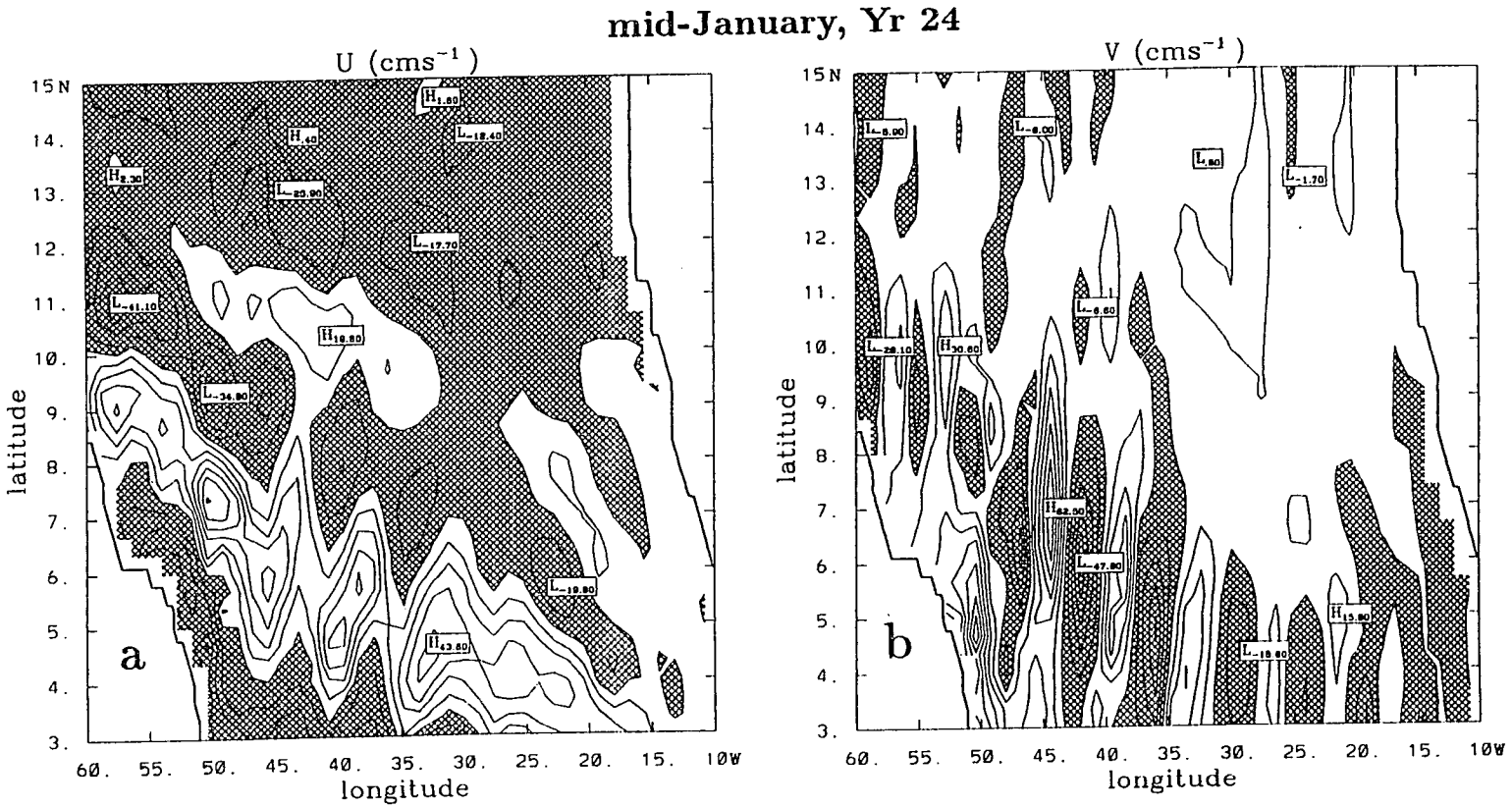

Figure 24: Same as Figure 18, but for mid-January of the last year of the model

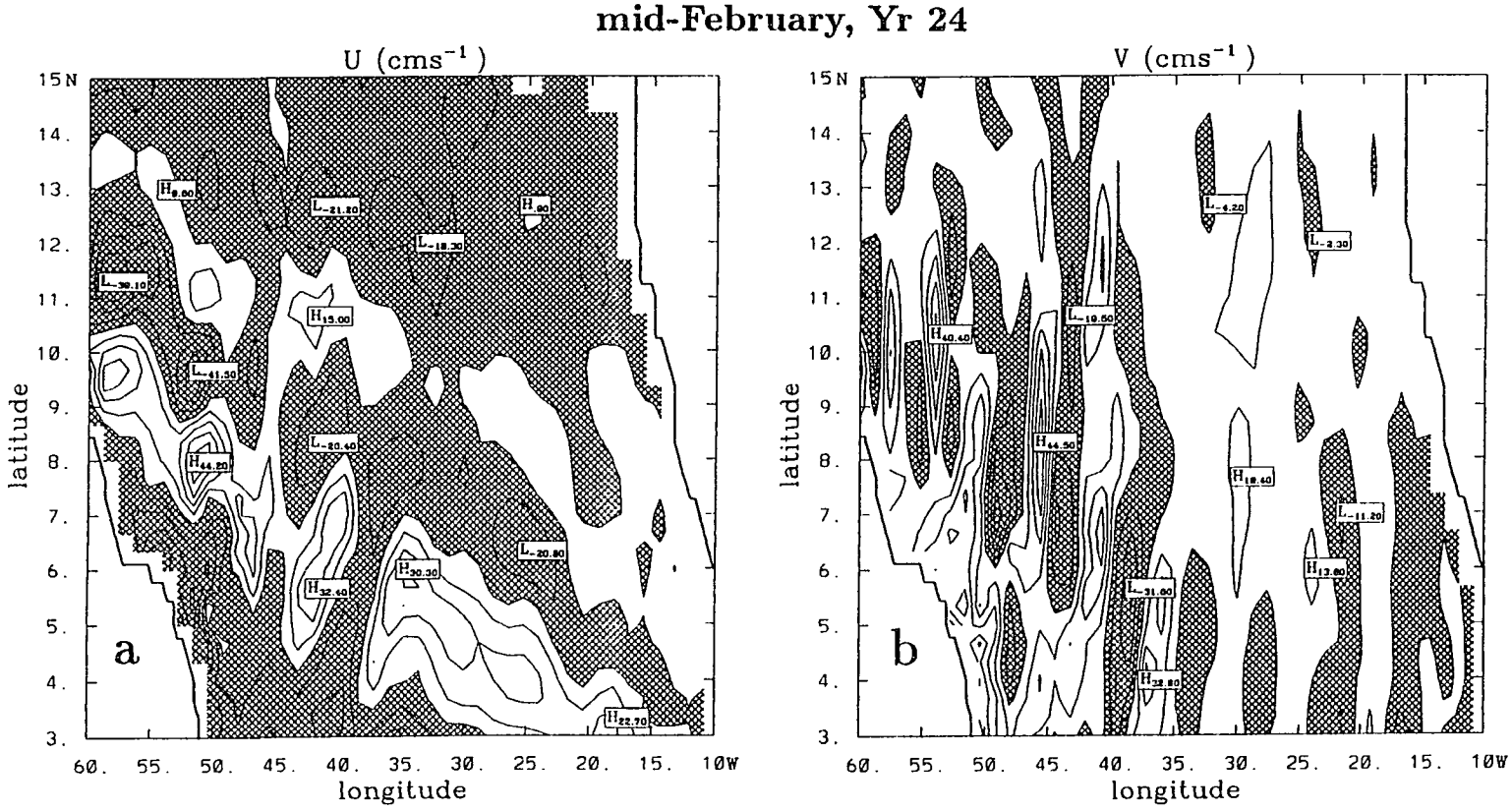

Figure 25: Same as Figure 18, but for mid-February of the last year of the model

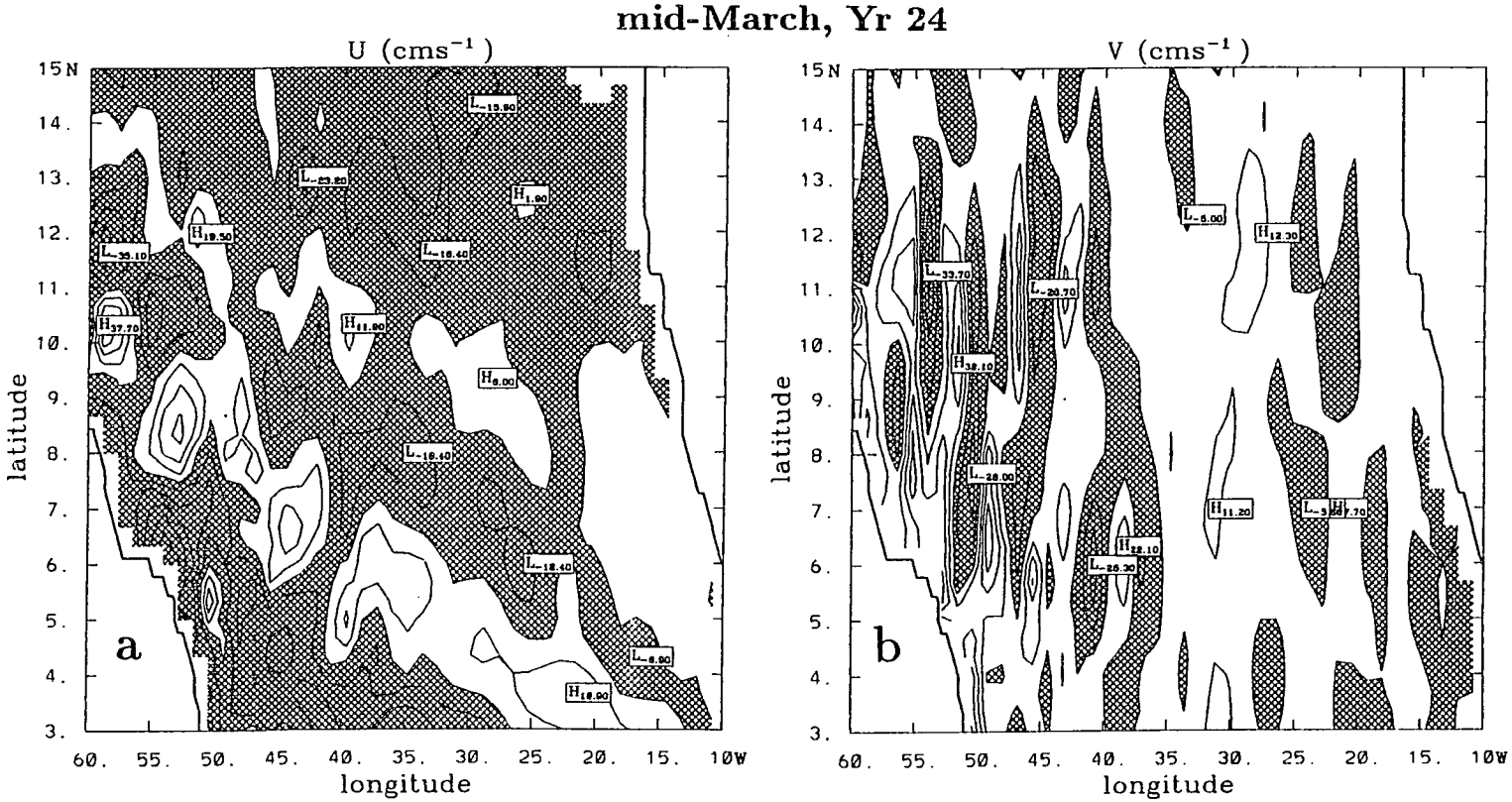

Figure 26: Same as Figure 18, but for mid-March of the last year of the model

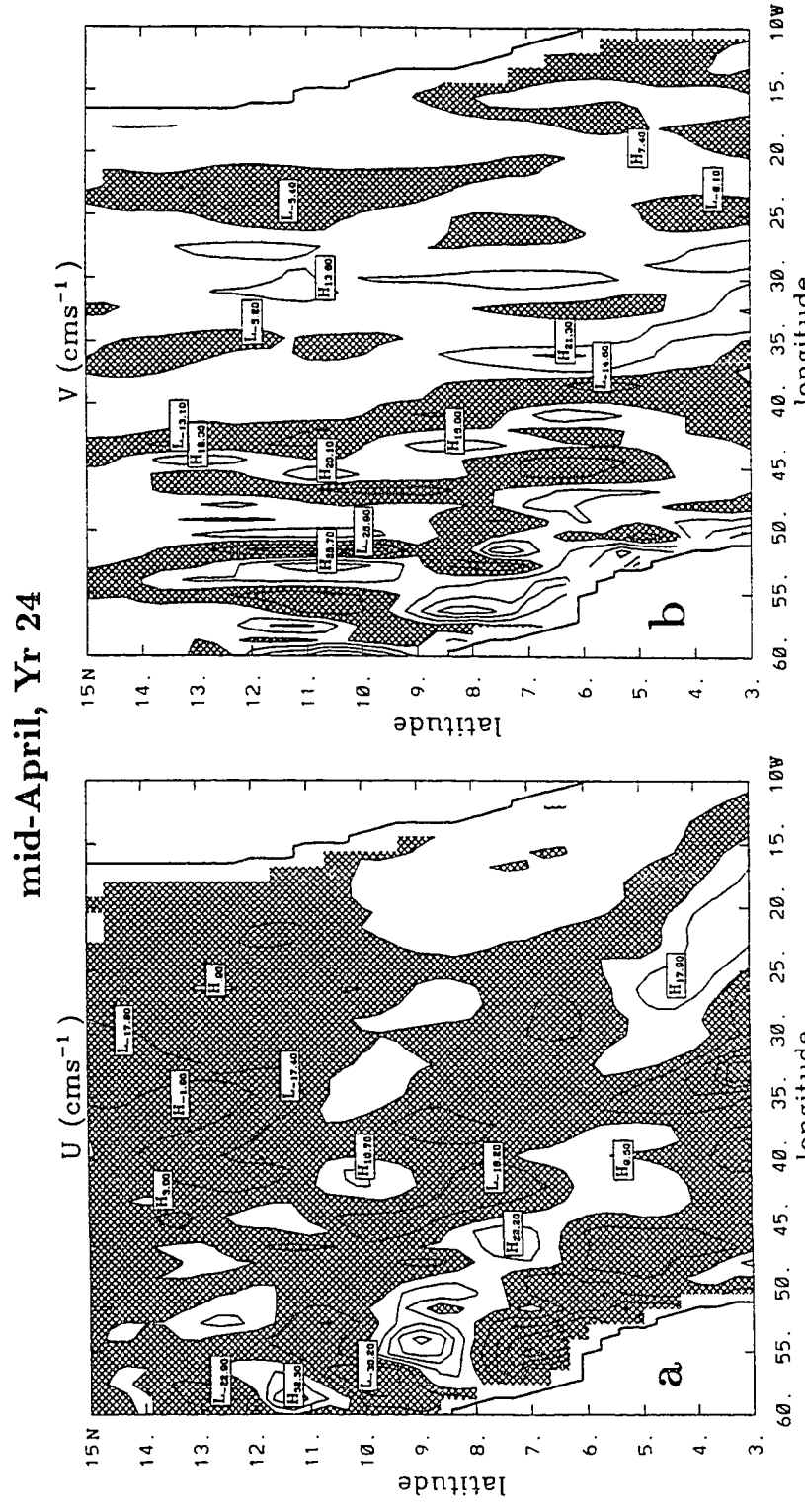

Figure 27: Same as Figure 18, but for mid-April of the last year of the model

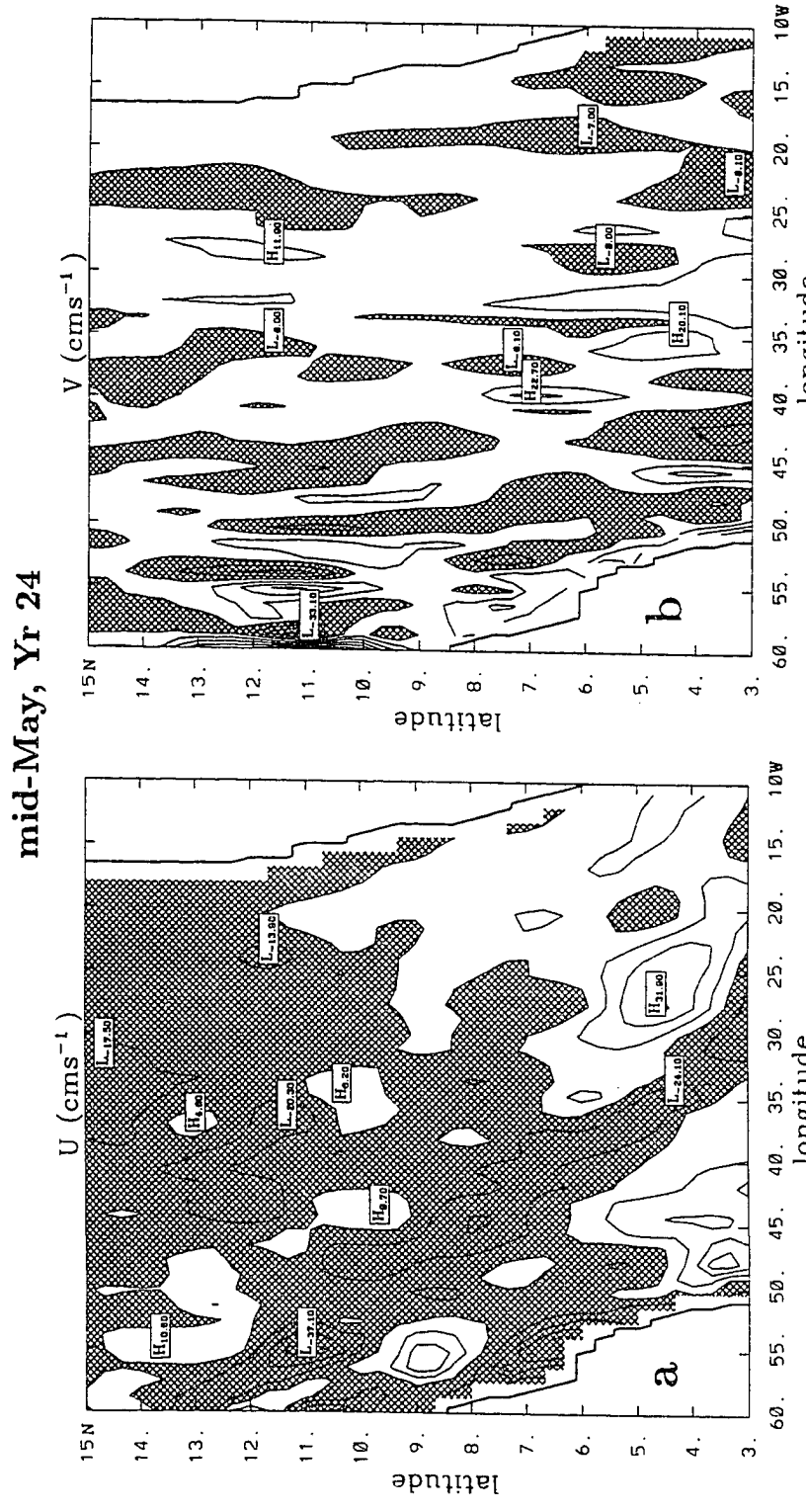

Figure 28: Same as Figure 18, but for mid-May of the last year of the model

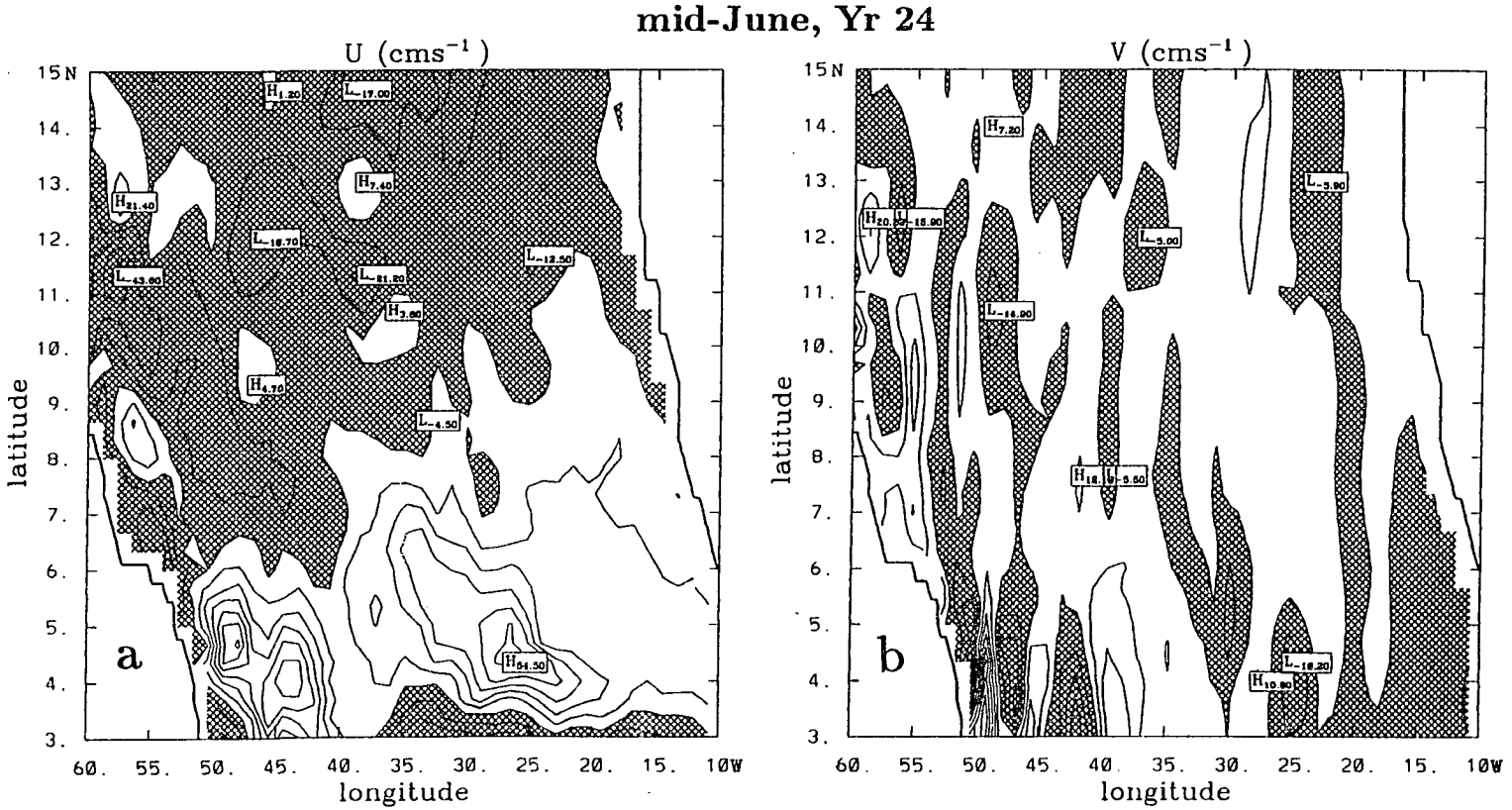

Figure 29: Same as Figure 18, but for mid-June of the last year of the model

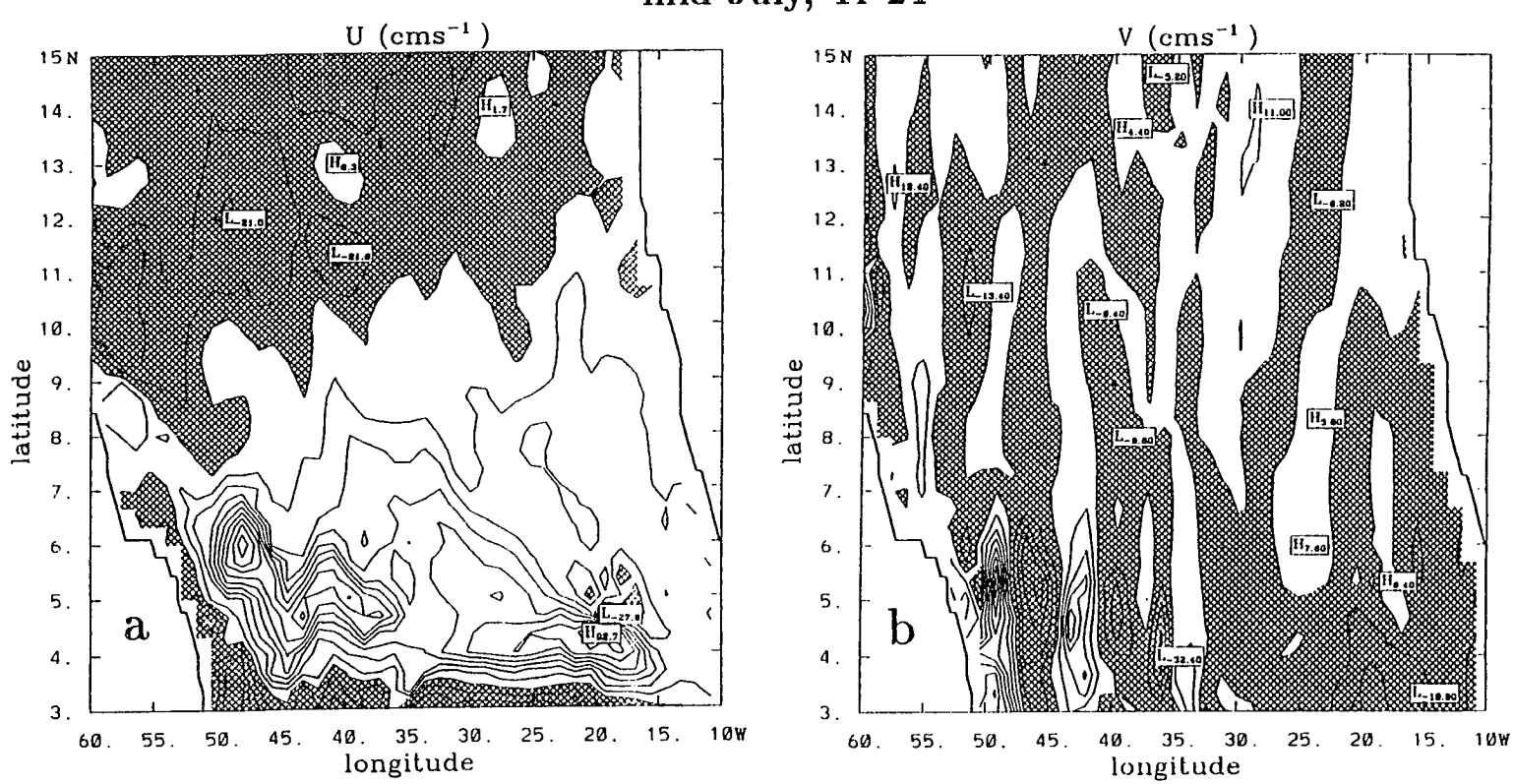

Figure 30: Same as Figure 18, but for mid-July of the last year of the model

are due to simple temporal changes. The structures in the meridional flow weaken with time and disappear first in the interior of the basin and finally disappear altogether before the retroflection starts up again. It will be shown in the remainder of this chapter that oscillations of the meridional component of velocity, with periods of 50 days, occur in this region at fixed locations from December through April. As well, they will be shown to to be advected westward along the same path as the wave-like structures discussed here.

5.2 Time Series Analysis

The first step in these analyses was to establish that a significant signal occurred in the meridional velocity component at or near 50 days. To do this the variance in the 40-70 day band of the meridional component (V) of velocity was calculated. This was done by first estimating the power spectral density (PSD) of the V-velocity at each grid point in the domain from the 256 available discrete samples. The expression for the PSD is

$$G(f) = \frac{2}{N\Delta t} \mid X(f) \mid^2$$

where N is the number of discrete samples and Δt is the time interval between samples. Here Δt is about 3 days, hence $N\Delta t$ is 779 days. $X(f)$ is the discrete form of the fast fourier transform (FFT) of the V-velocity which is defined as

$$X(f) = \Delta t \sum_{n=0}^{N-1} x_n e^{-i2\pi f n \Delta t}$$

where x_n is the velocity times series, $0 \leq n \leq N-1$ and and f is the frequency [Bendat and Piersol, 1986]. The FFT algorithm used was based on that of Cooley et al. [1969]. The variance in the 40-70 day band was obtained by integrating the PSD with respect to frequency over the frequency bands corresponding to the 40-70 day range (Figure 31). Energy is seen in the western region of the domain between 60°W and 30°W and between 3°N and 13°N. Three areas of "high" variance are seen. At 36°W, 5°N and 55°W, 11°N the variance exceeds 70 $cm^2\ s^{-2}$, while at 50°W, 7°N it is greater than 100 $cm^2\ s^{-2}$.

Time series of the meridional velocity at these three locations are seen in Figure 32. The time series were band-pass filtered between 40 and 70 days. The filter used

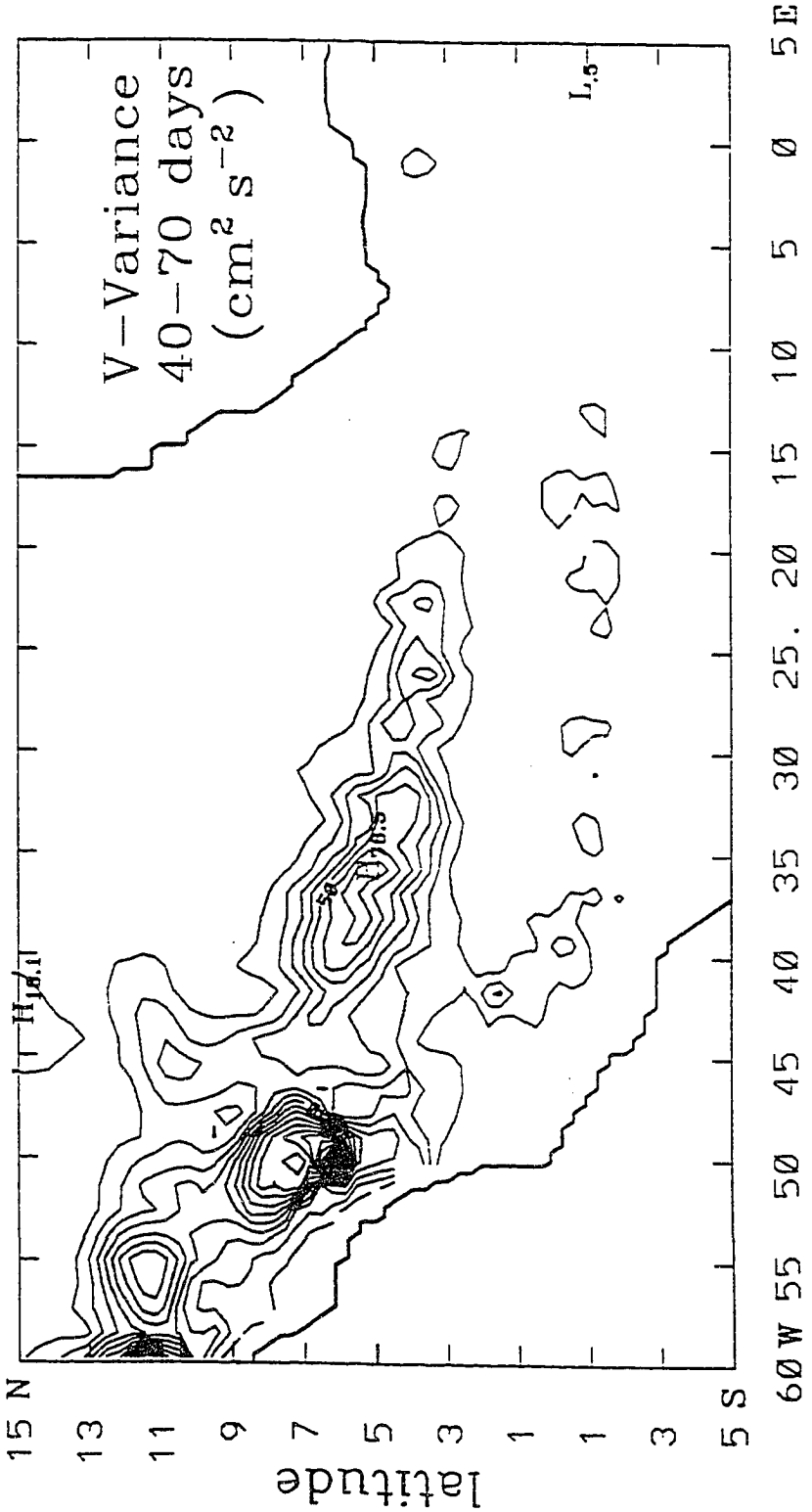

Figure 31: Variance of meridional component of velocity in $cm^2\ s^{-2}$, between 40 and 70 days. Contour interval is 10 $cm^2\ s^{-2}$.

is an infinitely long sinc function which is truncated at the second zero crossing. The sinc function is the fourier transform of a discrete step function in frequency space, hence the truncation results in an imperfect filter in frequency space. Band-passing was achieved by first low-passing at 1/40 cpd , then high-passing the remaining signal at 1/70 cpd. The start of the time series corresponds to Julian day 319 (November) of the third last year of the CME2 simulation, hence day 52 of the time series corresponds to January 3 of the following year. Two sets of wave packets are seen in each of the time series. This discussion will concentrate upon the details of the second wave packet in each time series. At 36°W, 5°N the onset of this packet occurs in November at about day 360 (Julian day 311) of the time series. The start of the first cycle in the wave packet is identified by a wave trough. The period of this trough to trough cycle is about 68 days. The remaining cycles in the wave packet have periods of about 52 days. Roughly 60 days later, a wave packet is seen at 50°W, 7.5°N; the period of its waves is about 52 days. A similar packet appears 30 days later at 55°W, 11°N. These lags in the appearance of the wave packet at progressively westward locations suggest that the packet is either propagating or being advected westward. If the former case is true, the group speed of the packet is 0.2 – 0.3 m s^{-1}. The wave packet at 36°W, 5°N contains 3 cycles (about 172 days) and is seen to decay in April (around day 744 of the time series). Evidently these oscillations are seen to appear at the end of the retroflection period and disappear just prior to it starting up again. Examination of the unfiltered meridional velocity at these locations shows the peak-to-peak amplitudes of the oscillations to be about 0.5 m s^{-1} (Figure 33).

Variance-preserving spectra of meridional velocity were then calculated at the "high" variance locations. These spectra were obtained by calculating the PSDs as before. Each PSD was logarithmically smoothed to produce 30 estimates over the

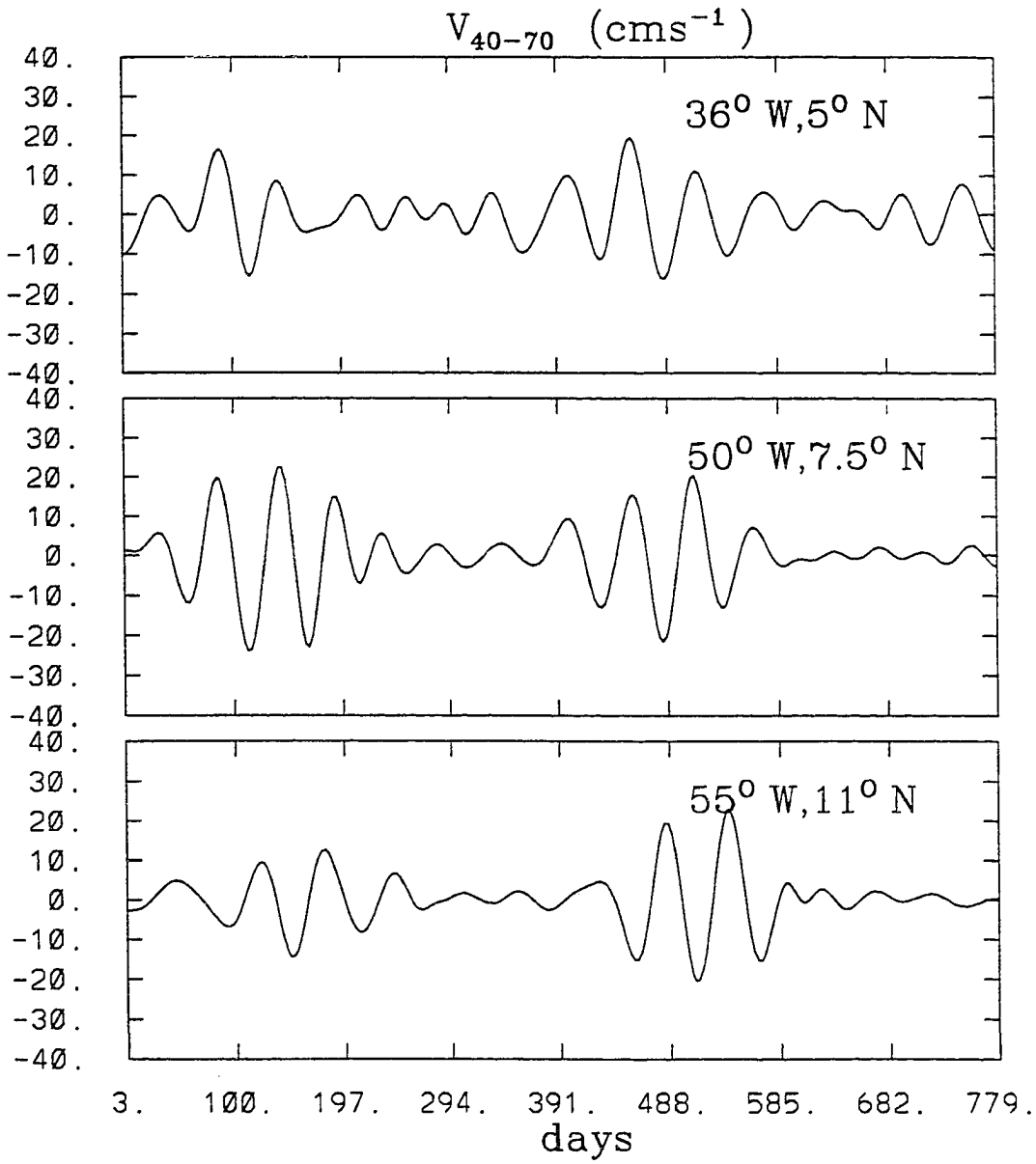

Figure 32: Time series of band-pass filtered (40-70 days) meridional velocity (m s^{-1}) at 36°W, 5°N, 50°W, 7.5°N and 55°W, 11°N. The times series extends a little over the last two years of the simulation. The time series starts at Julian day 319 (November) and day 52 corresponds to the start of the following year.

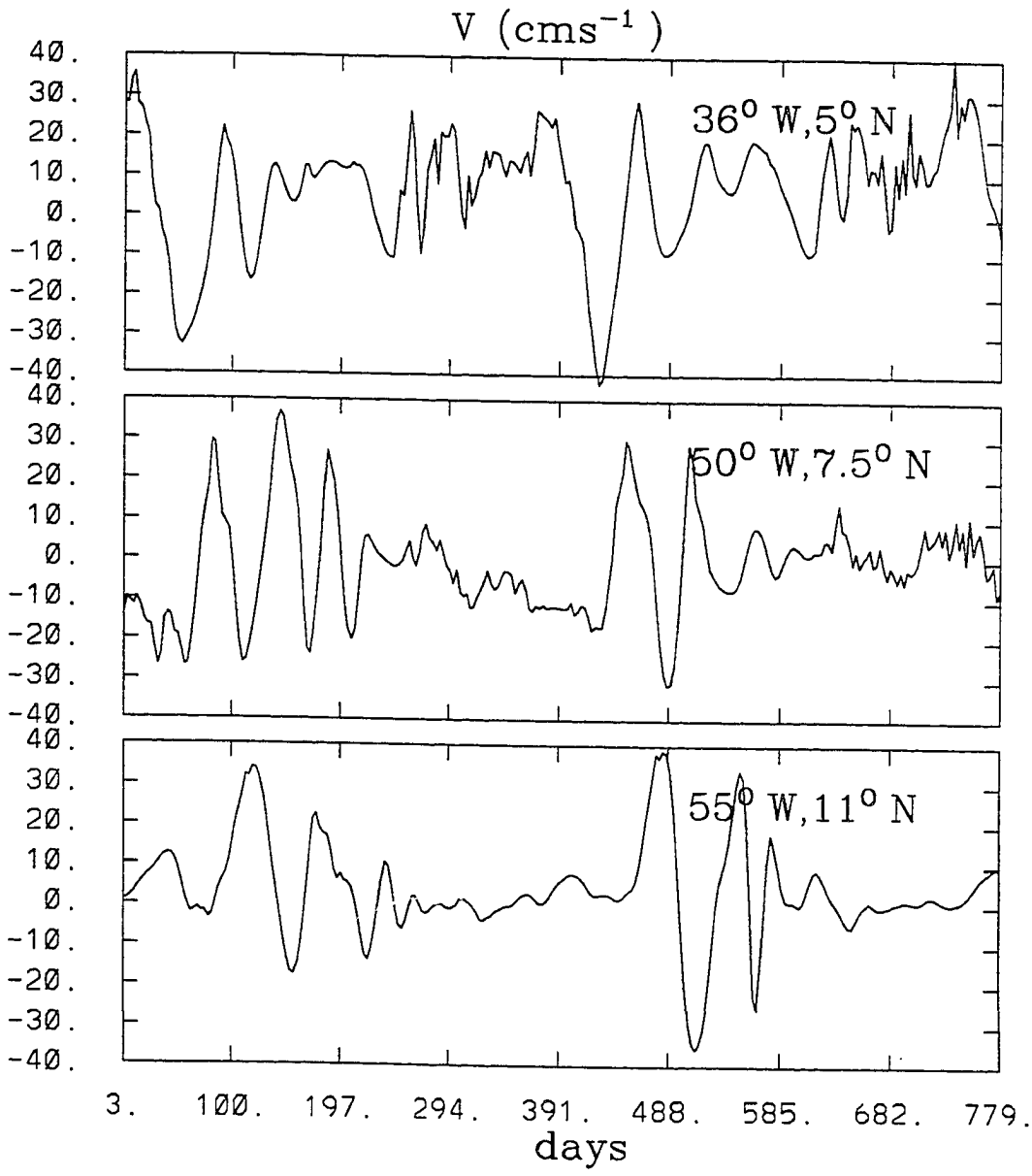

Figure 33: Same as Figure 32, except that the meridional velocities are unfiltered.

resolved frequency range. The smoothed spectra estimates were then multiplied by frequency to give the variance-preserving spectra. At 50°W, 7.5°N, a peak of about 230 $cm^2\ s^{-2}$ is seen to be centered at 52 days (Figure 34b). Energy in other bands is seen to be an order of magnitude smaller. A similar picture is seen at 55°W, 11°N (Figure 34c), although the peak occurs at a longer period (about 70 days). At 36°W, 5°N (Figure 34a), the largest peak occurs at 86 days and has a value of about 440 $cm^2\ s^{-2}$. Another smaller peak (140 $cm^2\ s^{-2}$) occurs at 52 days. The peak at 86 days may be due to the inadequate resolution of the 100 day period; two years of data may not be enough to resolve this signal properly. These spectral analyses confirm that a significant signal at or near 50 days is present in the meridional component of velocity at these locations, in particular at 50°W.

Time series of zonal velocity, band-passed filtered between 40 and 70 days, at the three locations discussed above are seen in Figure 35. Some evidence of wave packets are seen in these time series, but they are not as evident as those in the meridional component of velocity. The amplitudes are somewhat less than half those of the amplitudes of the band-passed filtered meridional velocities.

To determine the dispersion characteristics of the 50-day signal the horizontal phase relationship between two grid points in the western basin was investigated. The pair of grid points chosen were at 50.4°W, 7.33°N and 51.6°W, 7.33°N. These points were selected since they lie in a "high" variance area. The wavenumber vector can be assumed to be parallel to the "axis" of the V-variance map (Figure 31). This axis can be thought of as the line between the "high" variance locations. Since this line is about 17° from the horizontal in the interior, the north-south wavenumber is small relative to the east-west wavenumber.

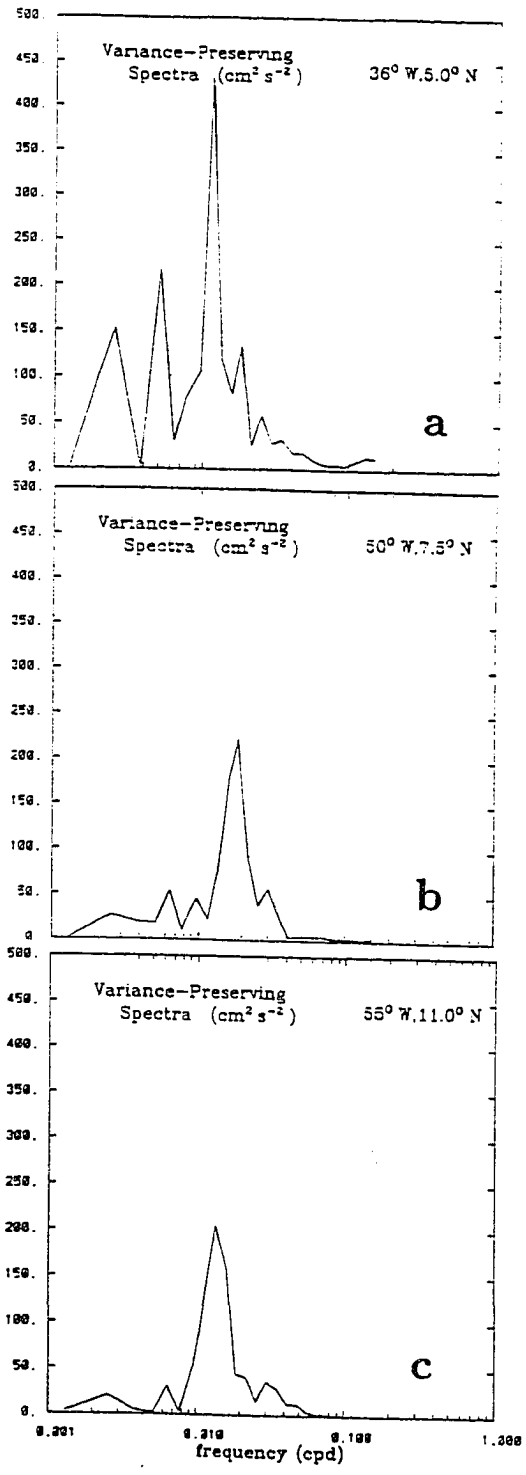

Figure 34: Variance-preserving spectra of meridional velocity at (a) 36°W, 5°N, (b) 50°W, 7.5°W and (c) 55°W, 11°N.

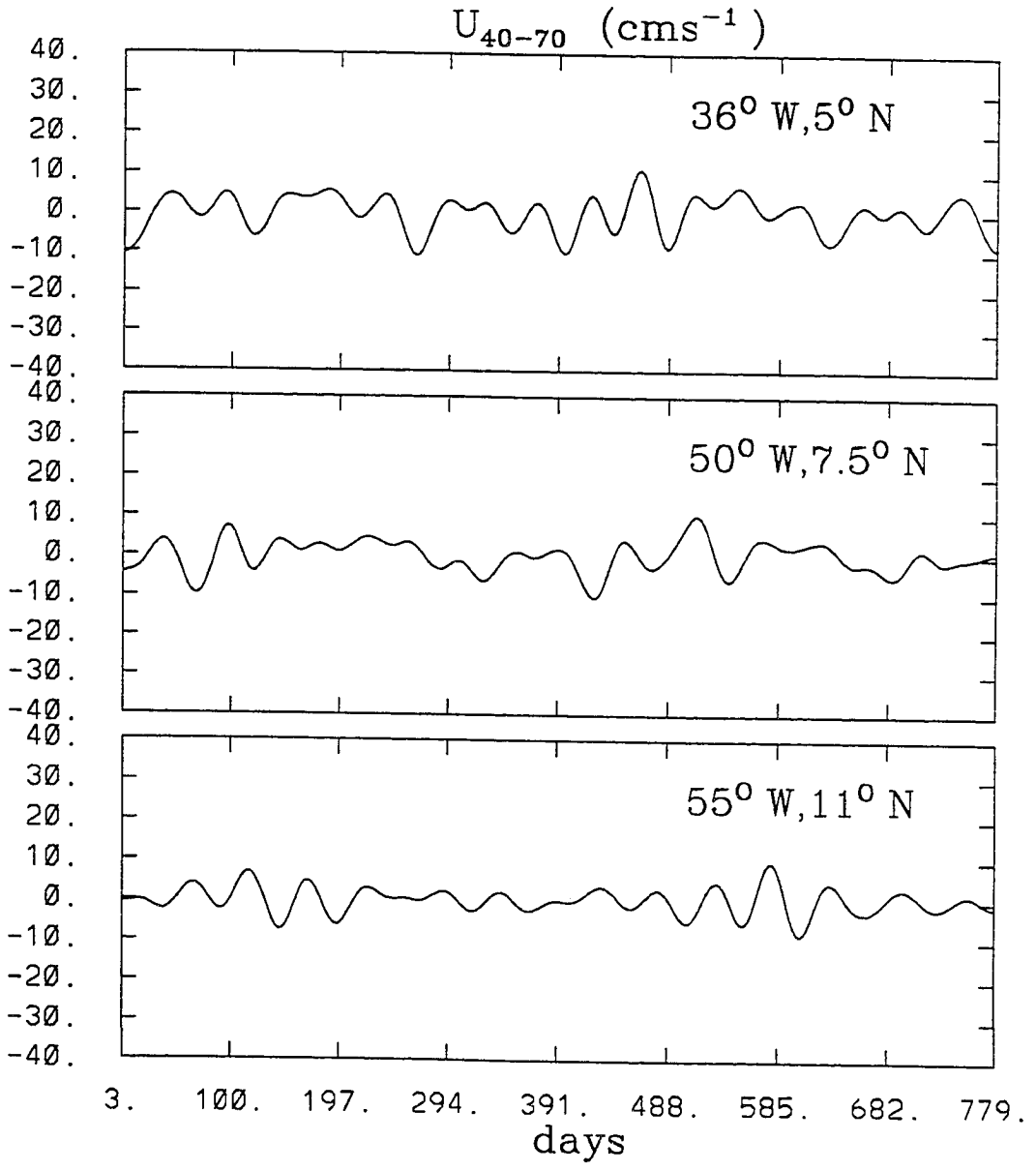

Figure 35: Same as Figure 32, except that the velocities are zonal.

A cross-spectral analysis (coherence-squared and phase calculation) was performed on the meridional component of velocity at the two sites over the extracted model period. The coherence function $\hat{\gamma}^2_{xy}(f)$ between two stationary time series $x(t)$ and $y(t)$ is estimated by

$$\hat{\gamma}^2_{xy}(f) = \frac{|\hat{G}_{xy}(f)|^2}{\hat{G}_{xx}(f)\hat{G}_{yy}(f)}$$

where $\hat{G}_{xx}(f)$ and $\hat{G}_{yy}(f)$ are the autospectral density functions of $x(t)$ and $y(t)$, respectively, and $\hat{G}_{xy}(f)$ is the cross-spectral density function between the two time series. The expression for the phase relationship between $x(t)$ and $y(t)$ is

$$\hat{\phi}(f) = tan^{-1}[-\hat{Q}_{xy}(f)/\hat{C}_{xy}(f)]$$

where $\hat{Q}_{xy}(f)$ and $\hat{C}_{xy}(f)$ are the real and imaginary parts, respectively, of $\hat{G}_{xy}(f)$. They are known as the quadrature spectrum and the co-spectrum, respectively [Bendat and Piersol, 1986]. The autospectral density functions, the co-spectrum and the quadrature spectrum were averaged over 3 adjacent bands to produce 6 degrees of freedom. The raw data were prewhitened using a finite-difference filter prior to calculating the spectra.

The result of this analysis is seen in Figure 36. A significant peak, at the 95% level, of 0.94 is seen at 0.02 cpd (50 days) in the coherence-squared plot. The significance level for the squared coherence was calculated using the expression

$$\left[\hat{\gamma}^2_{xy}(f)\right]_{crit} = \frac{F_{2,n-2}(\alpha)}{\frac{n-2}{2} + F_{2,n-2}(\alpha)}$$

where $[\hat{\gamma}^2_{xy}(f)]_{crit}$ is the squared coherence, $F_{2,n-2}(\alpha)$ is the F distribution with 2 and $n-2$ degrees of freedom for the 100α percentage point [Jenkins and Watts, 1968]. The phase at this frequency is +103.5°, suggesting that the V-component of flow at the most westward grid point lags that to the east by about 15 days (29%

of a 52-day period). The distance between grid points, Δx, is 132 km, hence the approximate wavelength is

$$\Delta x/(103.5°/360°) = 460\ km$$

The error associated with each phase estimate was obtained from the following formulation [Jenkins and Watts, 1968]

$$\Delta\phi(f,\alpha) = sin^{-1}\left[\frac{2}{n-2}\frac{1-\bar{\gamma}^2_{xy}(f)}{\bar{\gamma}^2_{xy}(f)}F_{2,n-2}(\alpha)\right]$$

The resulting range in the wavelength estimate is 410-520 km. This estimate agrees with the wavelength of the wave-like structures seen in the contours of meridional velocity in Section 5.1.

The phase speed, C, which is the rate at which the wave (crests and troughs) propagate, is defined as

$$C = \frac{\omega}{k}$$

where ω is radian frequency and k is the zonal wavenumber. For this case, it is -0.1 m s^{-1} with a range of -0.09 to -0.12 m s^{-1}. The same analysis was repeated between the meridional component of velocity at 38.4°W, 5.67°N and 36°W, 5.67°N. In this case the wavelength is 540 km with a range of 450-680 km and the phase speed is -0.12 m s^{-1} with a range of -0.10 to -0.15 m s^{-1}. Between 54°W, 9.3°N and 52.8°W, 9.3°N, the analysis yields a wavelength of 390 km (350-440 km) and a phase speed of -0.09 m s^{-1} (-0.08 to -0.10 m s^{-1}). Hence, the wavelength of the oscillations is shorter in the west than in the interior of the basin. These results are summarized in Table 1.

Preliminary identification of these oscillations is possible by considering the dispersion relationship for plane, off-equatorial baroclinic Rossby waves. The off-

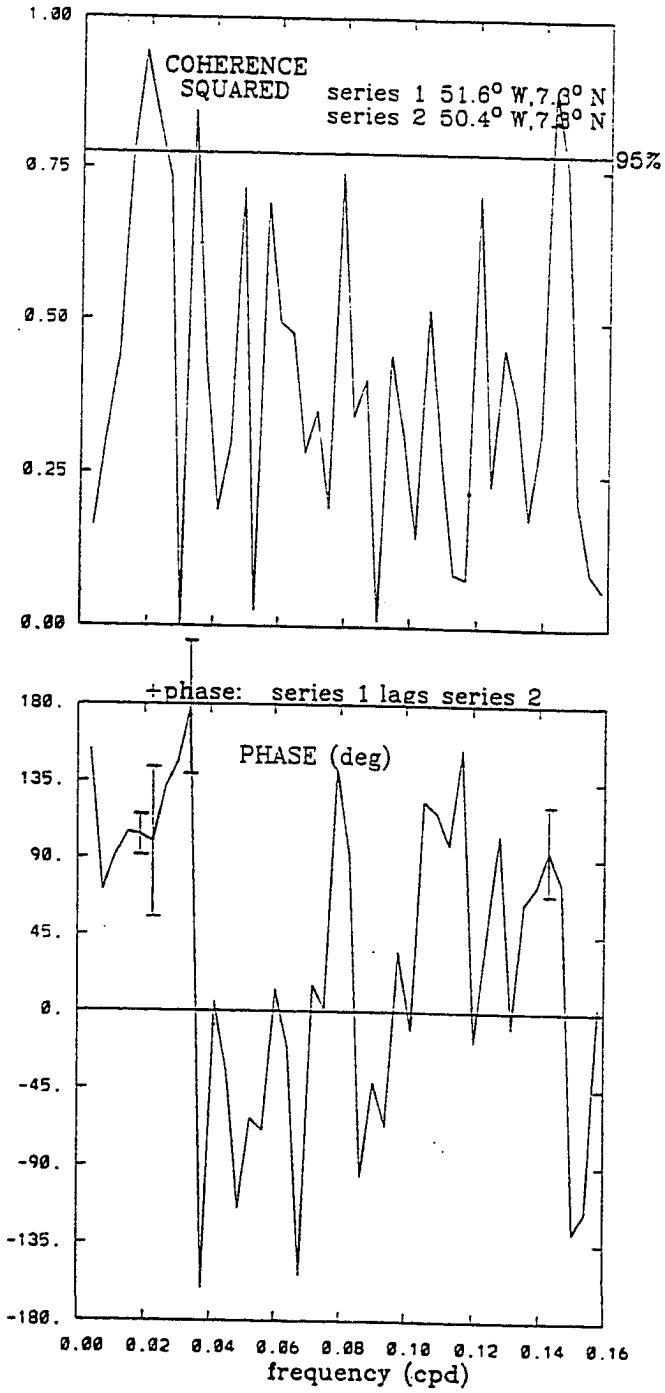

Figure 36: Cross-spectrum (coherence-squared and phase) of meridional velocity between 51.6°W, 7.33°N (series 1) and 50.4°W, 7.33°N (series 2).

Location: Series 1	**Location: Series 2**	**Wavelength (km) (range)**	**Phase Speed ($m\ s^{-1}$) (range)**
38.4°W, 5.7°N	36.0°W, 5.7°N	540 (450 to 680)	-0.12 (-0.10 to -0.15)
51.6°W, 7.3°N	50.4°W, 7.3°N	460 (450 to 680)	-0.10 (-0.09 to -0.12)
54.0°W, 9.3°N	52.8°W, 9.3°N	390 (350 to 440)	-0.09 (-0.08 to -0.10)

Table 1: Locations of series 1 and 2 used in cross spectral analyses and the resulting wavelength and phase speed calculated from phase estimates at 50 days. Their ranges reflect the error in the phase estimates.

equatorial relationship can be used since these oscillations lie well out of the equatorial waveguide (2°S to 2°N):

$$\omega = \frac{-\beta k}{k^2 + l^2 + R_n^{-2}}$$

where ω is the wave frequency, β is the planetary vorticity gradient, k and l are the zonal and meridional wavenumbers, and R_n is the internal Rossby radius of deformation for the *nth* baroclinic mode [Pedlosky, 1987]. It is defined as [Kundu, 1990]

$$R_n = c_n / f_0$$

where f_0 is the Coriolis parameter and c_n is the phase speed of long internal waves. The zonal phase speed of baroclinic Rossby waves is [Pedlosky, 1987]

$$C_x = \frac{-\beta}{k^2 + l^2 + R_n^{-2}}$$

The first baroclinic deformation radius, R_1, between 5° and 10°N and between 35° and 40°W is about 124 km [Emery et al. 1984]. The wavelength of the 52-day oscillation was found to be 540 km from the cross-spectral analysis performed in this area. The associated wavenumber, k is -1.16×10^{-5} m^{-1}. l is assumed to be zero since the direction of propagation of the signal as shown by the V-variance (Figure 31) is almost zonal. The phase speed and the period calculated for the Rossby wave relationships are -0.11 m s^{-1} and 55 days, respectively. These values compare well with the inferred values of the zonal phase speed and period.

In the case of a Rossby wave, the phase speed in the x-direction is always negative (westwards), however the component of the group velocity in the x-direction can be positive or negative [Pedlosky, 1987]. A packet containing a wave for which

$$k^2 > l^2 + R_n^{-2}$$

will propagate in the positive x-direction (eastwards), while a packet for which

$$k^2 < l^2 + R_n^{-2}$$

propagates westwards. Here, $k^2 > R^{-2}$, hence the group velocity is directed eastwards. This eastward group velocity at first sight conflicts with the westward packet propagation inferred from the meridional time series in Figure 32. The group velocity of a Rossby wave in the x-direction is [Pedlosky, 1987]

$$G_{gx} = \beta \frac{k^2 - l^2 - R^{-2}}{(k^2 + l^2 + R^{-2})^2}$$

which, in this case, is 0.04 m s^{-1}. Since this value is small, it could be overridden by westward advection.

A comparison of the results from these analyses and those obtained by Johns et al. [1990] revealed some similarities. The oscillations in both cases exhibited a mean periodicity of about 50 days. In the CME model, the oscillations were only seen during the non-retroflection period (February through May), while in the observations they were seen throughout the year. The period, however, varied in the observations from 40 days in spring to 60 days in fall. Significant energy was found in both cases at periods of about 50 days, and the phase speeds and wavelengths obtained from the cross-spectral analyses were both around -0.10 m s^{-1} and 500 km. In both cases, the waves were considered to approximate first mode baroclinic Rossby waves, with the caveat that the group speed of the model oscillations appears to be in the wrong direction. However, this discrepancy may be explained by westward advection. Also, it should be noted that the observed oscillations were documented over the continental slope, while those in the model were found over most of the western tropics.

5.3 Nature of 50-Day Oscillations

According to the above, there is reason to believe that the 50-day oscillations seen in the extracted model are baroclinic Rossby waves. To investigate this idea further, velocity cross-spectra were calculated in those parts of the domain where the 50-day oscillations appeared. Wavenumber, k, estimates were found from phase shifts whenever they were significant at 0.02 cpd. The north-south wavenumber, l, was again zero. These wavenumber estimates, at a fixed frequency, were then compared with the theoretical dispersion curve for a first baroclinic Rossby wave.

Time series of meridional velocity at adjacent or nearby points along a line connecting the high variance centers at 36°W, 5°N and 50°W, 7°N in Figure 31 were the raw material of the calculations. Table 2 shows their locations. The spacing between grid pairs was about 2.4° of longitude (265 km). In all cases, the grid points in each pair were at the same latitude. The squared coherence values were significant at the 95% level for all but one pair of grid points. In the previous section, cross-spectra were calculated between velocity series separated by about 130 km in basin interior. There, the coherency varied little from that obtained between series separated by about 240 km. The k estimates were obtained at periods of 52 days ($\omega = 1.4 \times 10^{-6}$ s^{-1}) from the phase shifts.

Pair	Location: Series 1	Location: Series 2
1	36.0°W, 5.3°N	33.6°W, 5.3°N
2	38.4°W, 5.7°N	36.0°W, 5.7°N
3	40.8°W, 6.0°N	38.4°W, 6.0°N
4	43.2°W, 6.0°N	40.8°W, 6.0°N
5	45.6°W, 6.3°N	43.2°W, 6.3°N
6	46.8°W, 6.7°N	45.6°W, 6.7°N

Table 2: Locations of pairs of grid points used in cross-spectral analyses.

The $\omega - k$ pairs are listed in Table 3. The grid point pair from which the estimates were obtained is also listed and can be found by referring to Table 2. The k (m^{-1}) and ω (s^{-1}) values were non-dimensionalized by c/f_0 and $f_0/\beta c$, respectively. f_0 is the value of the Coriolis parameter at the latitude of interest, β is the planetary vorticity gradient and c is the phase speed of long internal waves. This non-dimensionalization scheme is that used for the l=0 theoretical Rossby wave dispersion curve (Figure 37) such that the maximum frequency and zero group speed are attained at kc/f_0=−1, corresponding to $\omega_{max} f_0/\beta c$=0.5 [Kundu, 1990]. Regions of negative and positive group velocity, C_{gx} are indicated in Figure 37. If the same values for the parameters are chosen when non-dimensionalizing, the points fall onto the same domain as the theoretical dispersion curve. If the points lie on or near the curve within some error range it is reasonable to infer that the oscillations approximate baroclinic Rossby waves.

The values of the parameters used when non-dimensionalizing must be representative of the domain from which the wavenumber estimates were obtained. The cross-spectra were limited to the interior region (35°, 5°N to 50°W, 7°N) so that each of the parameters would have roughly the same value. The values of f_0 and β were calculated using a latitude of 6°N, the average latitude of this subdomain. As mentioned, R_1 is roughly 124 km, hence c_1 is 1.9 m s^{-1}. The theoretical curve was constructed using the Rossby wave dispersion relationship in the previous section. The $\omega - k$ points, where ω corresponds to periods of 52 days, and the theoretical dispersion curve are seen in Figure 38. The $\omega - k$ estimates are represented by letters in Figure 38; these letters and the corresponding $\omega - k$ pairs are listed in Table 3. The error in the wavenumber estimate is seen directly below the letter with which the error is associated. The errors are located at different frequencies

Pair	I.D.	Wavenumber (m^{-1})	Frequency (s^{-1})	Period (days)
1	A	-8.68572E-06	1.40543E-06	51.75
2	B	-1.16645E-05	1.40543E-06	51.75
3	C	-1.12296E-05	1.40543E-06	51.75
4	D	-9.39709E-06	1.40543E-06	51.75
5	E	-1.05336E-05	1.40543E-06	51.75

Table 3: $\omega(k)$ pairs associated with periods of 52 days. The number designates the locations from which $\omega - k$ pairs were calculated and the letter is used as identification in the following figures.

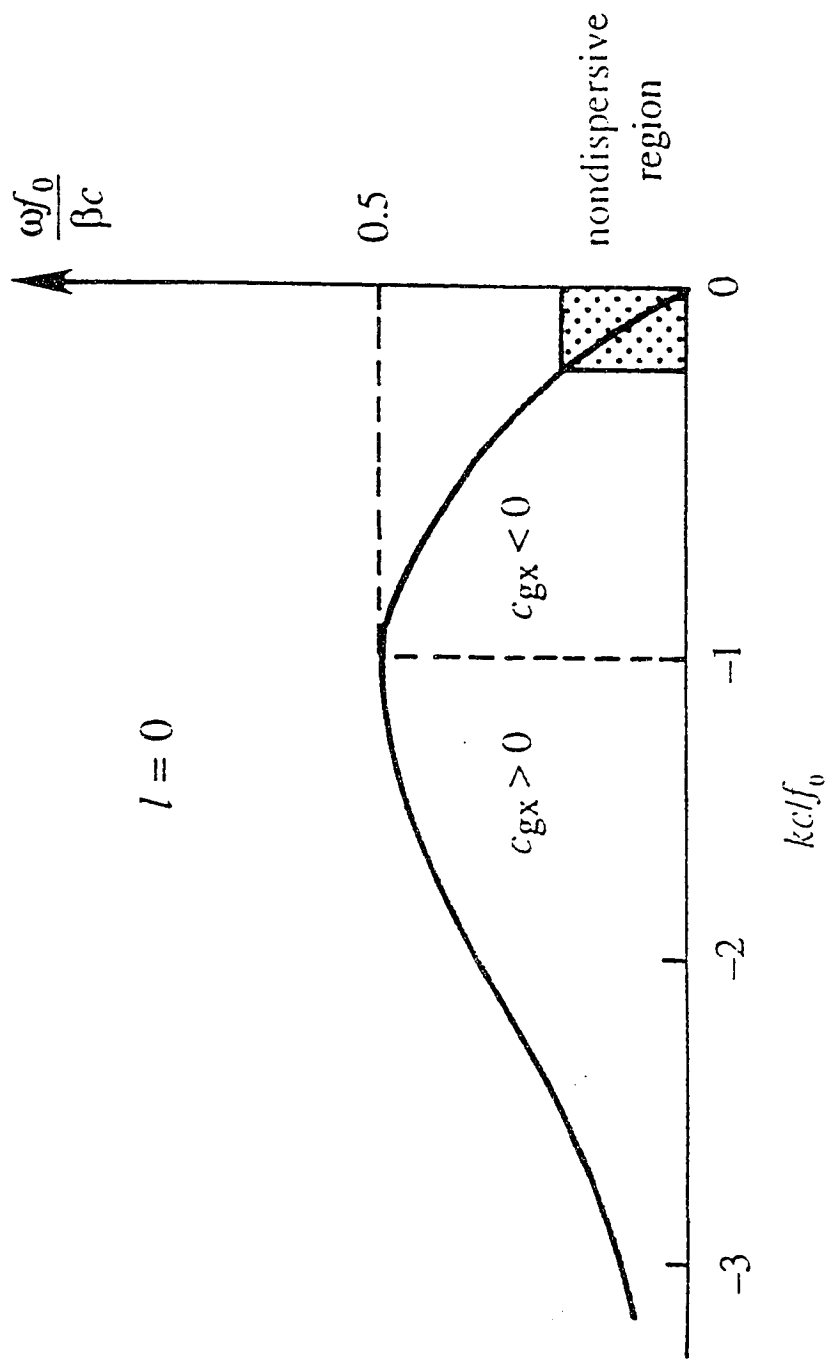

Figure 37: Theoretical dispersion relation (ω vs k) for l=0 (after Kundu [1990]).

to improve graphic representation; in reality they occur at the non-dimensionalized frequency corresponding to 52 days. The error is again obtained from the phase error which was calculated using the formulation in the previous section. Again, the 95% confidence level is used.

The $\omega_{52} - k$ estimates lie very close to the zero group velocity inflection point of the Rossby wave curve. They do, however, also lie in the section of the domain where C_{gx} is greater than zero. This region of the domain represents short Rossby waves. The non-dimensionalized theoretical wavenumber at 52 days is about -1.2. A line is drawn over the full extent of the frequency domain at this wavenumber value. The line intersects four of the error estimates associated with the $\omega_{52} - k$ estimates. The one remaining error estimate does not lie far from this line. Hence, it is reasonable to infer that these points have the dispersion characteristics approximating linear, first baroclinic mode Rossby waves with zero or slightly eastward group velocity. Again, this result is in contradiction with the reported westward wave packet propagation discussed earlier. Further evidence for the nature of these oscillations will be presented in the following section, as well as an explanation of these conflicting findings.

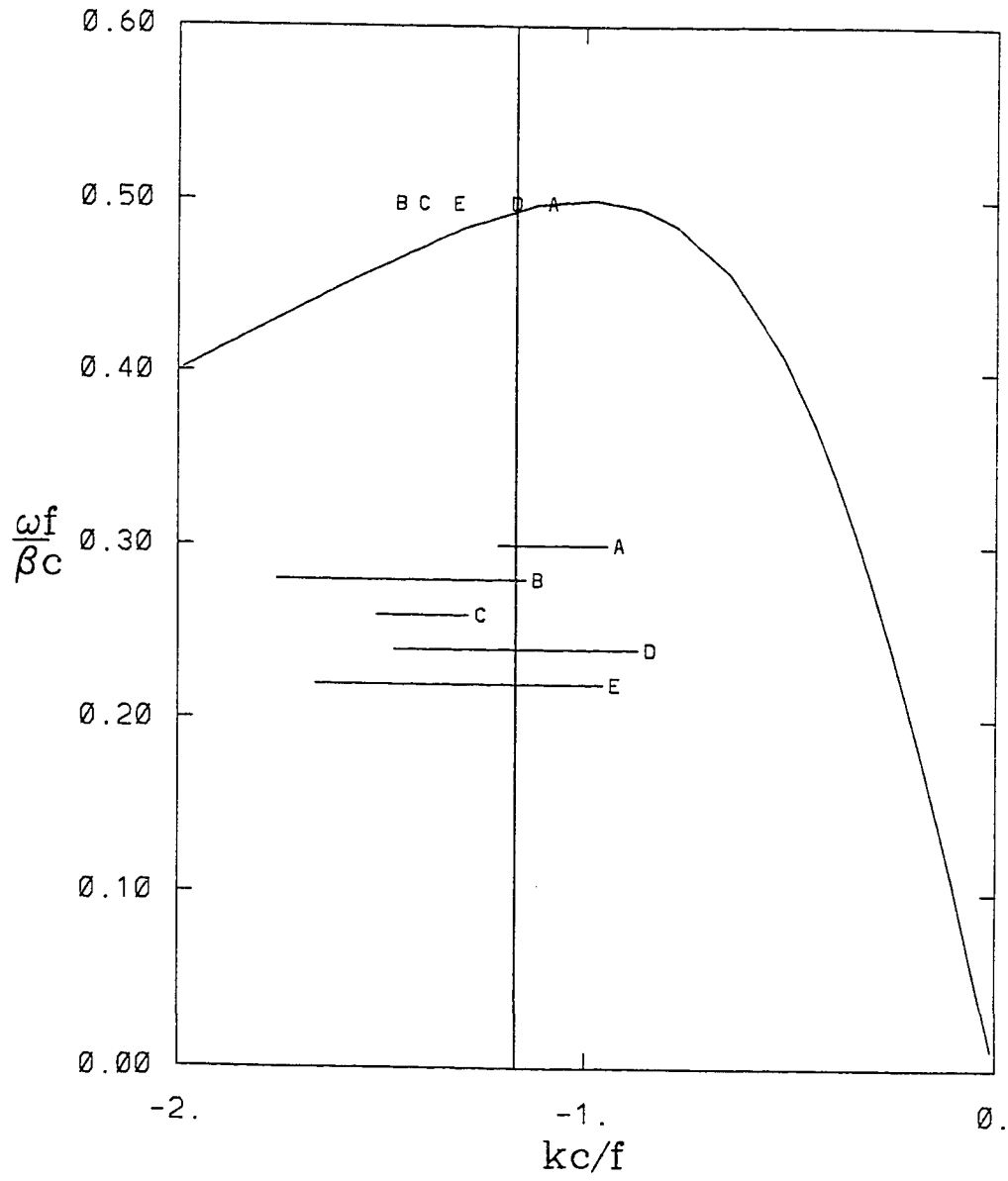

Figure 38: Non-dimensionalized $\omega - k$ pairs where ω corresponds to periods of 52 days are plotted in the same domain as the theoretical dispersion curve for a first mode baroclinic Rossby wave. The error associated with each estimate of k is found by looking directly below the associated letter.

5.4 Dynamics of 50-Day Oscillations

It would appear from the time history of the depth-averaged velocity fields discussed earlier, that a meander pattern expands eastward as the NECC develops and retreats westward as the NECC weakens and vanishes. These meanders weaken with time and disappear first in the interior of the basin and finally disappear altogether before the retroflection starts up again. They move westward along the same path and at the same time as the 50-day oscillations discussed above, hence it is reasonable to consider the oscillations and the meanders to be the same phenomenon. To verify the dynamics suggested by the time history and further validate the claim that the 50-day oscillations are indeed Rossby waves, a vorticity analysis was performed on snapshots of velocity taken from the retroflection and non-retroflection periods.

The first snapshot discussed is from February when the 50-day oscillations are most pronounced and the retroflection is absent. The leading balance obtained is that known to represent Rossby waves. The dominant modes of these waves were then identified from a modal decomposition and the vorticity analysis was repeated using the flow fields associated with the barotropic and first three baroclinic modes. These calculations were then performed using a snapshot from the retroflection period. The same leading balance and dominant modes were obtained, hence the meanders are also Rossby waves in an eastward zonal current. Consequently, one can say that the 50-day oscillations are the residue of the meander pattern associated with the NECC.

In this study, the vorticity analysis scheme developed as part of the PRE-EVA

(PRimitive Equation Energy and Vorticity Analysis) package [Spall, 1989] was used to obtain the leading balance in the full vorticity equation. It is derived from the energy and vorticity (EVA) scheme developed and used by Pinardi and Robinson [1986, 1987]. The package calculates all the terms in the full vorticity equation from the output of a primitive equation model. The version used in this thesis was specifically formulated by Spall for the CME model [Spall, 1992]. The vertical vorticity equation was obtained from the horizontal momentum equations by cross-differentiating the momentum equations and summing to eliminate the pressure. The resulting vorticity equation is

$$\zeta_t = -\mathbf{u}_H \cdot \nabla\zeta - \beta v + f w_z + \zeta w_z - w\zeta_z - (u_z w_y - v_z w_x) + B\zeta_{zz} + F_h + T$$

Each of the terms are explained in Table 4. The truncation error warrants special attention; it is due to the misrepresentation of spatial derivatives in the vorticity equation that arises when finite difference schemes are used. The package solves the vorticity equation term by term and then calculates the time rate of change of relative vorticity, ζ_t, as a residual. The package output consists of horizontal maps of each of the terms over some specified region at a particular model level.

The first snapshot of velocity subjected to the vorticity analysis was taken from the start of February (field D033.48) in the last year of the CME simulation; the time at which 50-day oscillations are known to be most pronounced. The analyses were run using the full CME model resolution on the NCAR (National Center for Atmospheric Research) CRAY Y-MP at Boulder, Colorado. The precision of the CRAY is to twelve decimal places, hence round-off error by truncation is minimized. The analysis must be performed at a particular level; the middle of the third layer (92 m) was chosen in this case. This depth was selected as it lies largely outside of the influence of the surface boundary conditions. Since the surface salinity is

Vorticity equation terms	Explanation
ζ	Relative vorticity
ζ_t	Time rate of change of relative vorticity
$\mathbf{u}_H \cdot \nabla\zeta$	Horizontal advection of relative vorticity
βv	Horizontal advection of planetary vorticity
fw_z	Stretching of planetary vorticity
ζw_z	Stretching of relative vorticity
$w\zeta_z$	Vertical advection of relative vorticity
$u_z w_y - v_z w_x$	Vorticity by twisting of horizontal velocity fields
$B\zeta_{zz}$	Vertical diffusion of zeta
F_h	Horizontal diffusion of zeta
T	Truncation error, non-conservative term

Table 4: Explanation of terms in the vorticity equation

relaxed back to Levitus [1982] climatology, instabilities associated with convective overturning may occur. The effects of these instabilities are unlikely to penetrate further than the top two layers of the model. Also, the modal decomposition (to be discussed shortly) revealed that the zero crossings for the first and second baroclinic modes were well below this depth; consequently, the wave signal is detectable in these velocities.

The analysis yielded horizontal maps of the terms in the vorticity equation over the area of interest. Balances in the western boundary layer are likely to be more complicated than in the interior and a clear understanding of the nature of the oscillations may not be obtainable there. Consequently, the region of interest was limited to the interior (5° to 11°N and 48° to 31°W). The maps are seen in Figures 39-48. In the region through which the waves are known to propagate (35°W, 5°N to 48°, 7°N), the leading terms are the horizontal advection of planetary and relative vorticity (Figures 41 and 40, respectively), stretching of planetary vorticity (Figure 42) and the time rate of change of vorticity (Figure 39). Alternating bands of highs and lows are seen in each of these terms, although this pattern is less coherent in the stretching term. The terms are mostly in phase. There is a contribution from the twisting term in isolated patches but it does not display the same spatial distribution as the other terms. Outside of the oscillation region, no significant contribution is made by any of the terms. It appears that the balance in this case is

$$\zeta_t = -\mathbf{u}_H \cdot \nabla\zeta - \beta v + f w_z$$

This balance, as mentioned earlier, is the vorticity balance for advected baroclinic Rossby waves. It should be noted however, that the magnitude of the $\mathbf{u}_H \cdot \nabla\zeta$ term is larger than the other two terms. This advection term will be dominated by $u\partial\zeta/\partial x$, since there is no significant mean component of flow in the meridional direction at

this time (Figure 25b). The "path" along which the oscillations move (Figure 25b) lies in a region of westward flow (Figure 25a), hence the vorticity field is most likely being advected westward. The next most important term is βv and there is some contribution from fw_z.

It is apparent that the fields are noisy. At some particular location (45°W, 5°N), the magnitudes of the terms balance while at others the balance is not as exact. To remove some of the noise in these fields, as well as identify the dominant wave modes, a modal decomposition was performed. The decomposition acts to "filter out" unwanted signals not associated with that of the waves.

Prior to performing the decomposition, the time rate of change of relative vorticity, ζ_t, was determined independently to check the validity of calculating this term as the residual of the full vorticity equation. Fields of relative vorticity, ζ, were also produced by this package, hence ζ_t can be obtained by calculating ζ at two successive times separated by about three days (D033.48 and D036.52) using a finite difference scheme. The resulting ζ_t field (Figure 49) displayed similar patterns to that calculated as a residual (Figure 39), however the magnitudes were smaller. This discrepancy can be explained by the three day time interval used in the finite difference scheme. This interval represents how often model fields are stored and is much greater than the model time step. If the ζ fields had been more closely spaced together in time, the magnitudes would have been similar. It appears that calculating ζ_t as a residual produces a reasonable result.

The analyses in the previous section suggested that the oscillations were first mode baroclinic Rossby waves. To determine if this is so, a normal mode decomposition was performed on the velocity field. The theory governing this decomposition

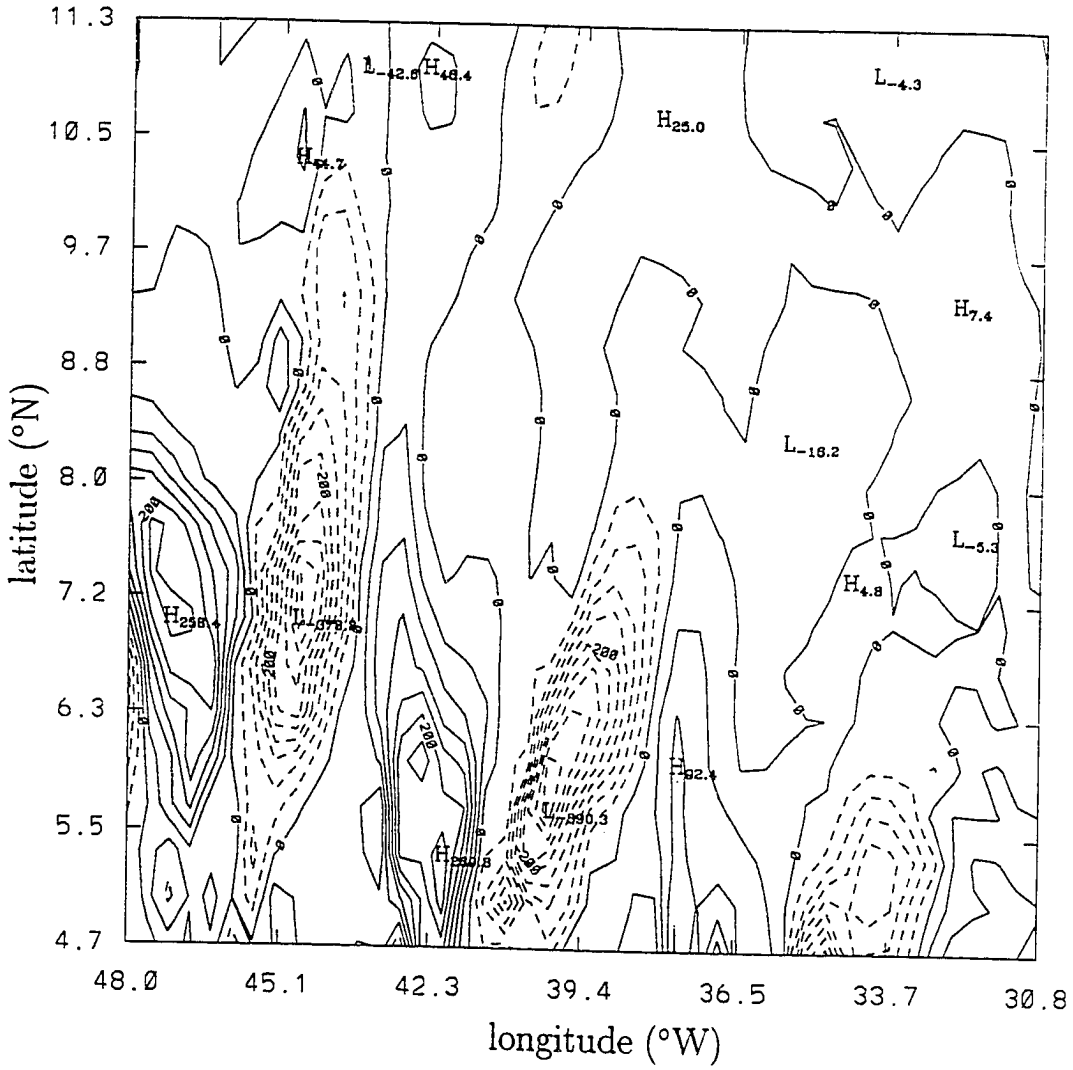

Figure 39: Time rate of change of relative vorticity (s^{-2})

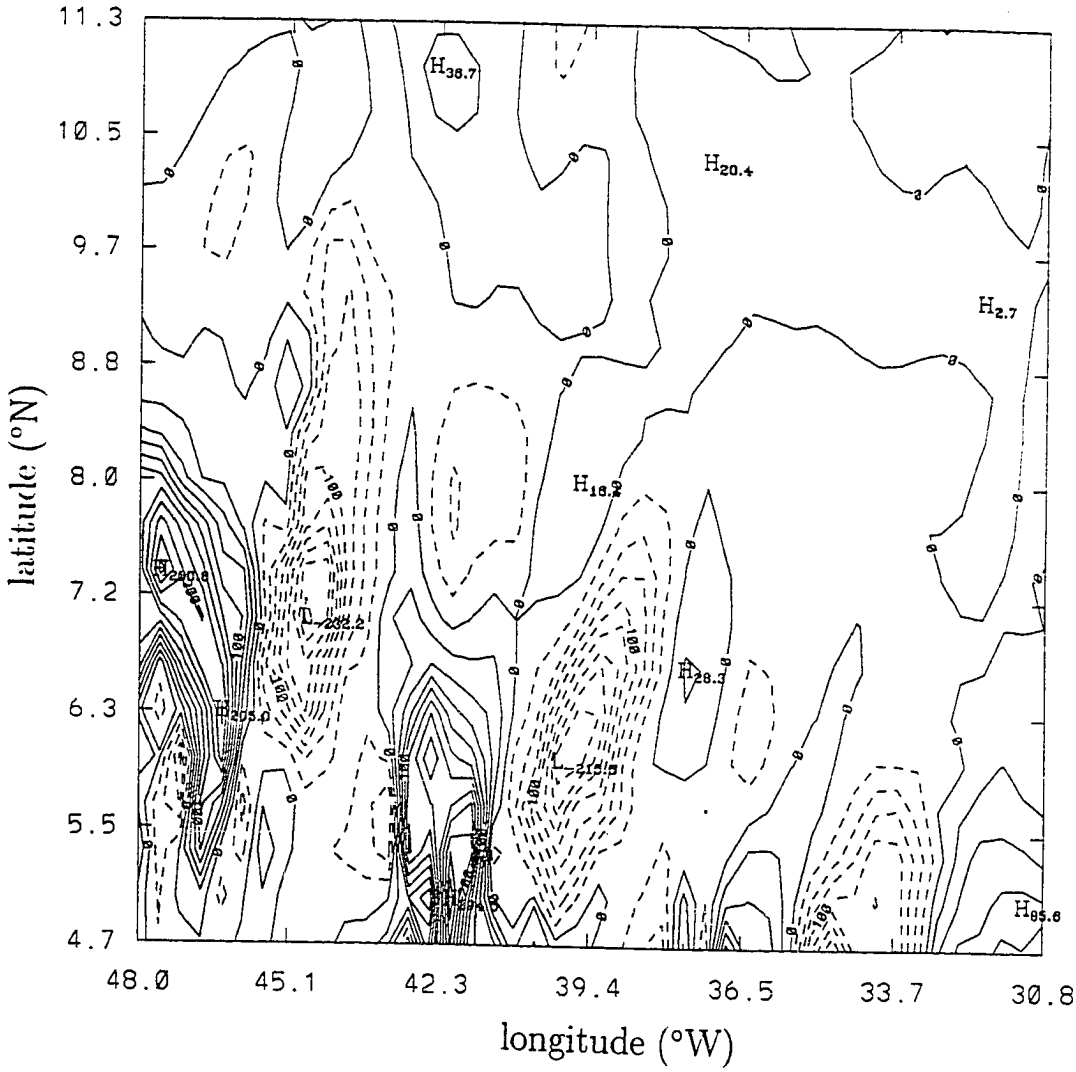

Figure 40: Horizontal advection of relative vorticity (s^{-2})

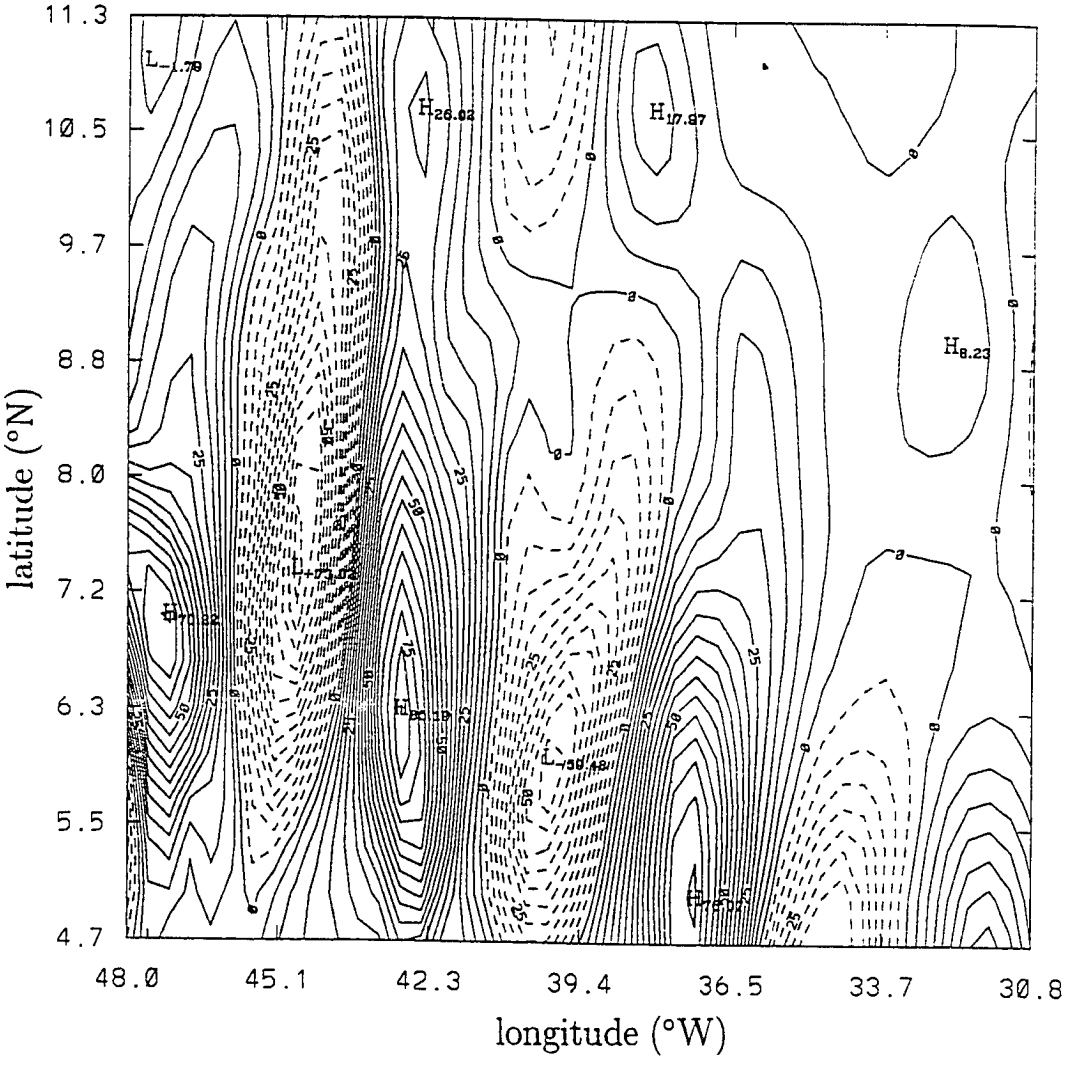

Figure 41: Horizontal advection of planetary vorticity (s^{-2})

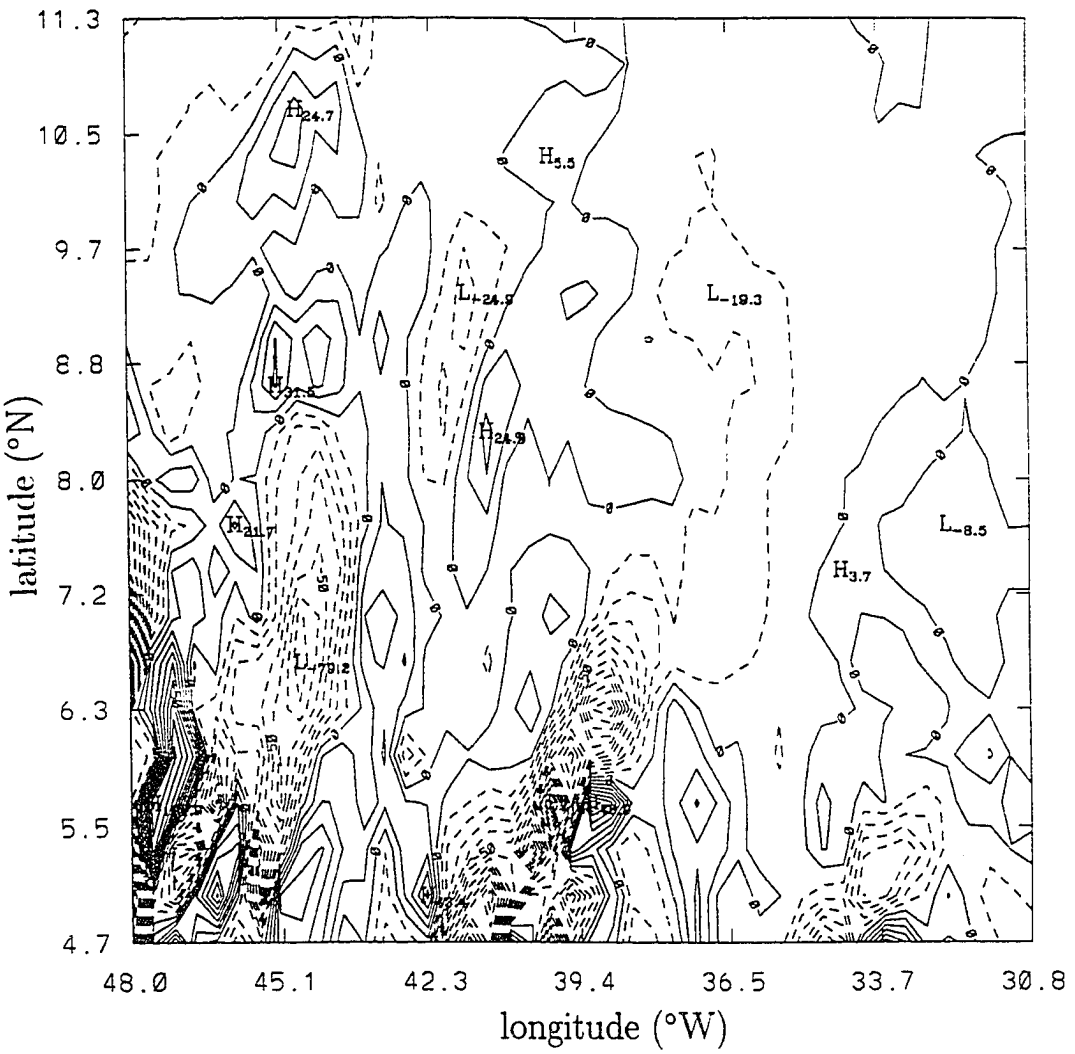

Figure 42: Stretching of planetary vorticity (s^{-2})

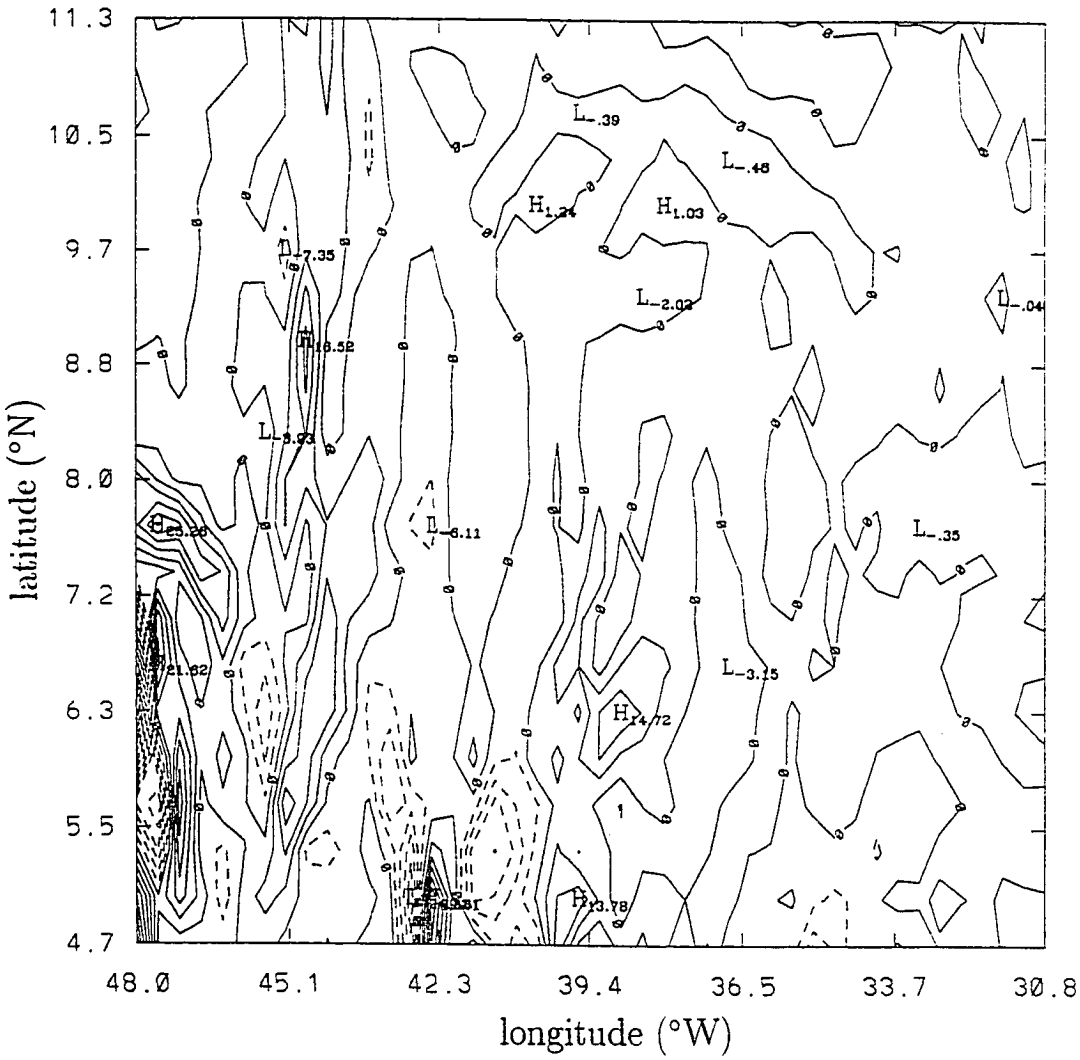

Figure 43: Stretching of relative vorticity (s^{-2})

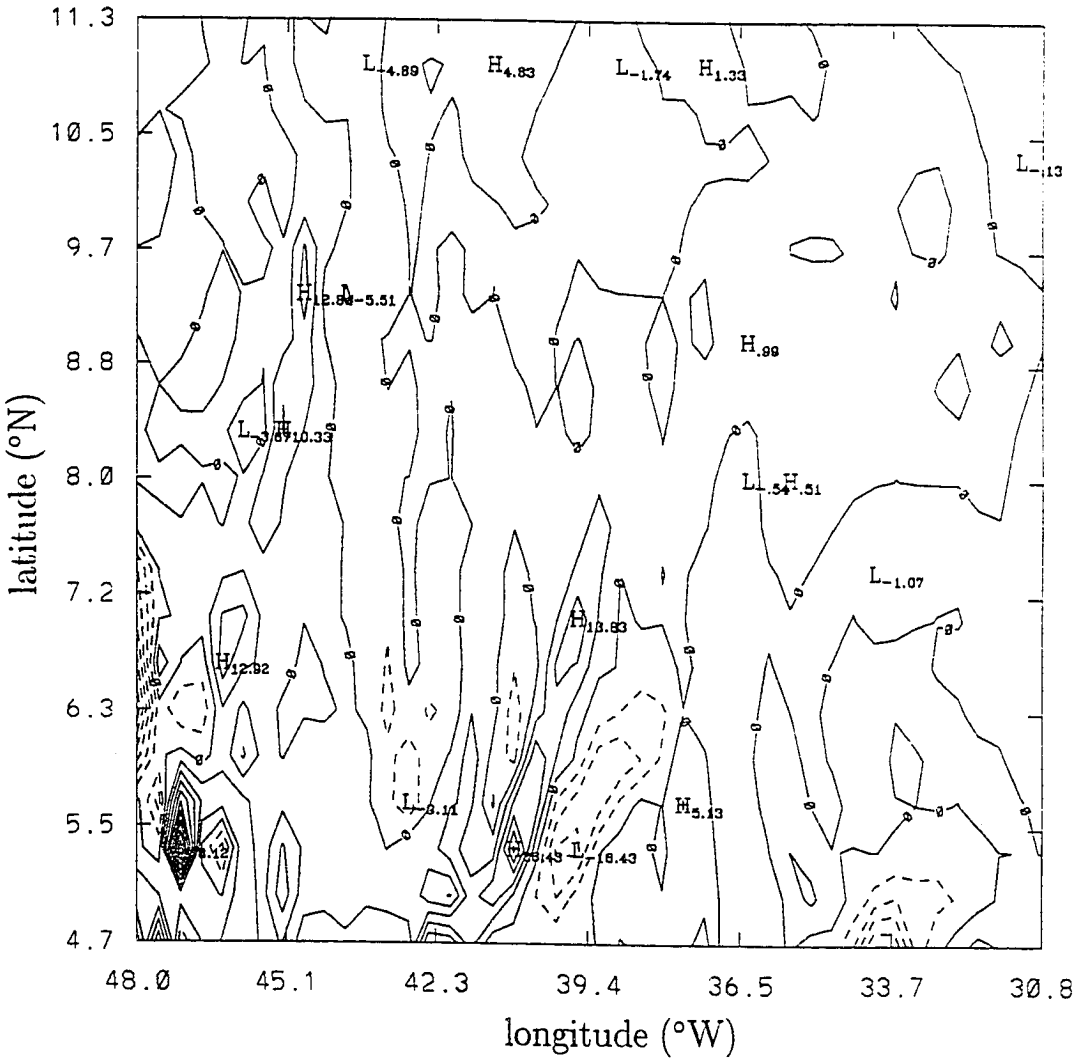

Figure 44: Vertical advection of relative vorticity (s^{-2})

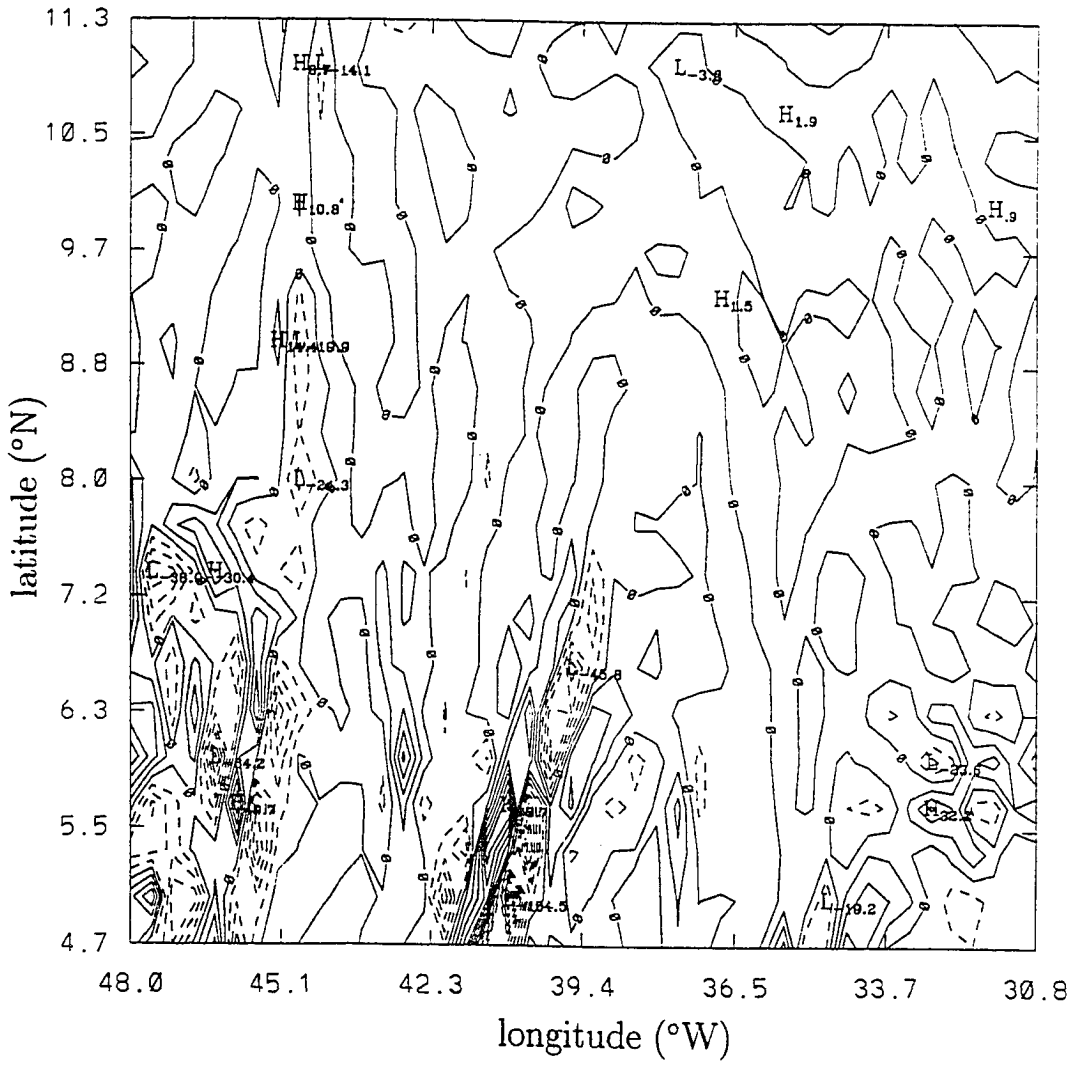

Figure 45: Vorticity by twisting of horizontal velocity fields (s^{-2})

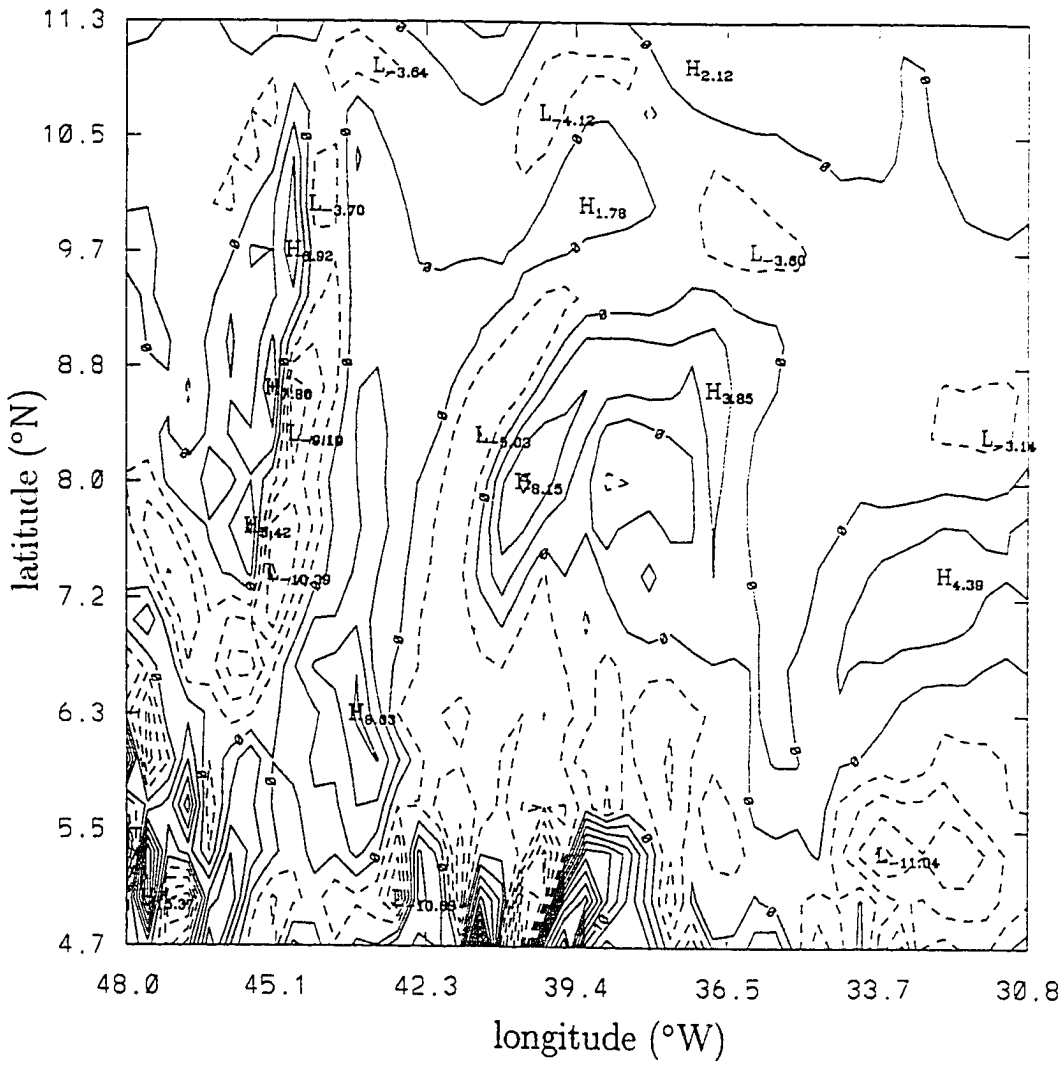

Figure 46: Vertical diffusion (s^{-2})

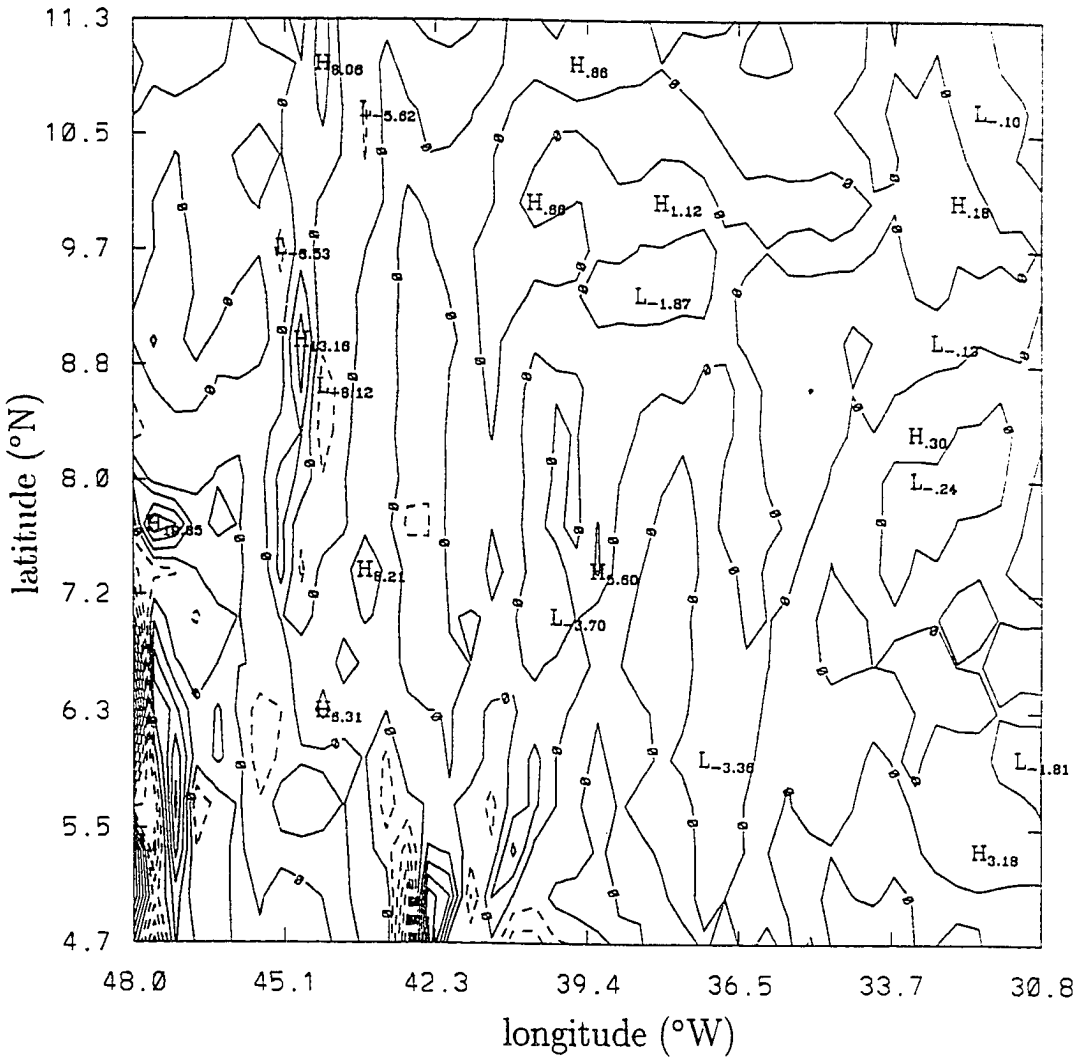

Figure 47: Truncation error (s^{-2})

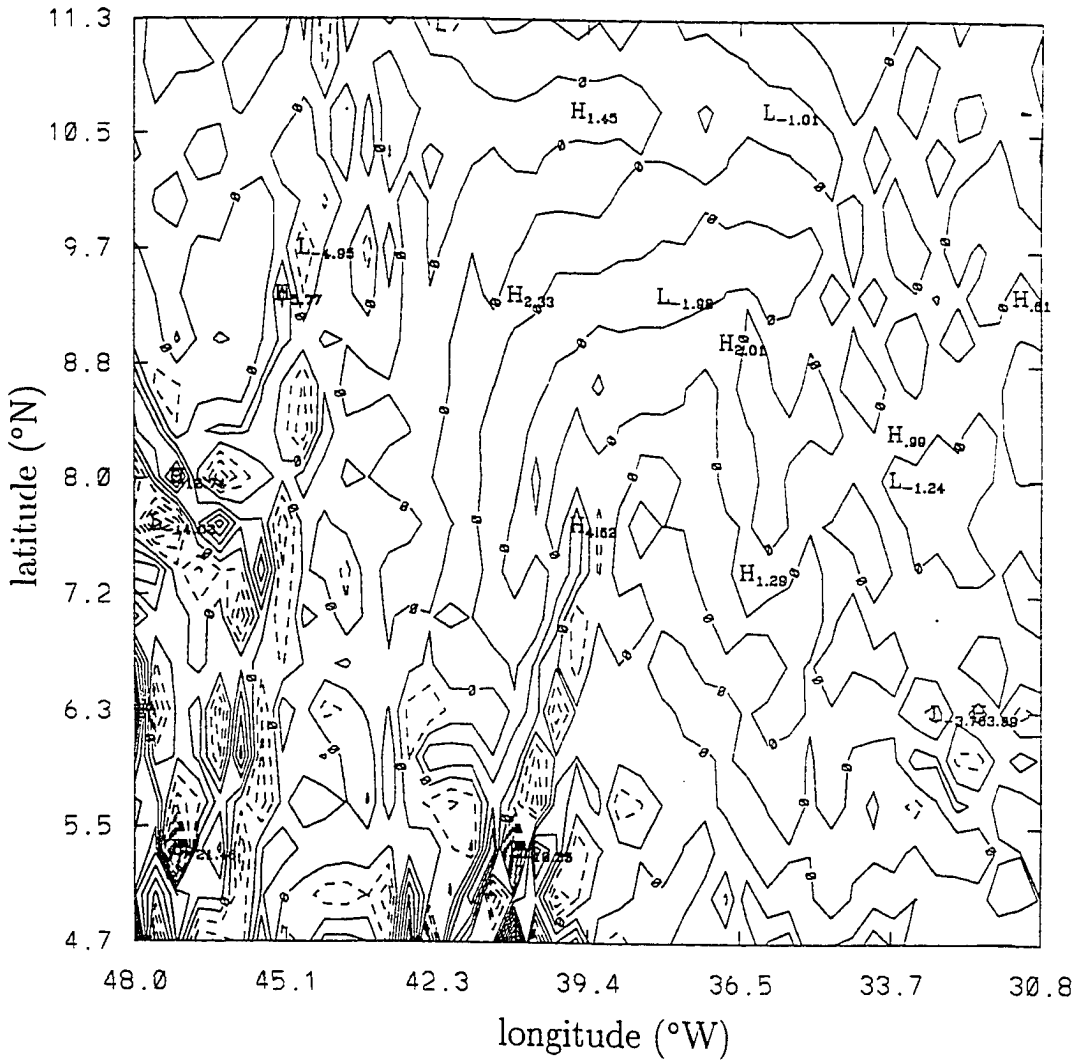

Figure 48: Horizontal diffusion (s^{-2})

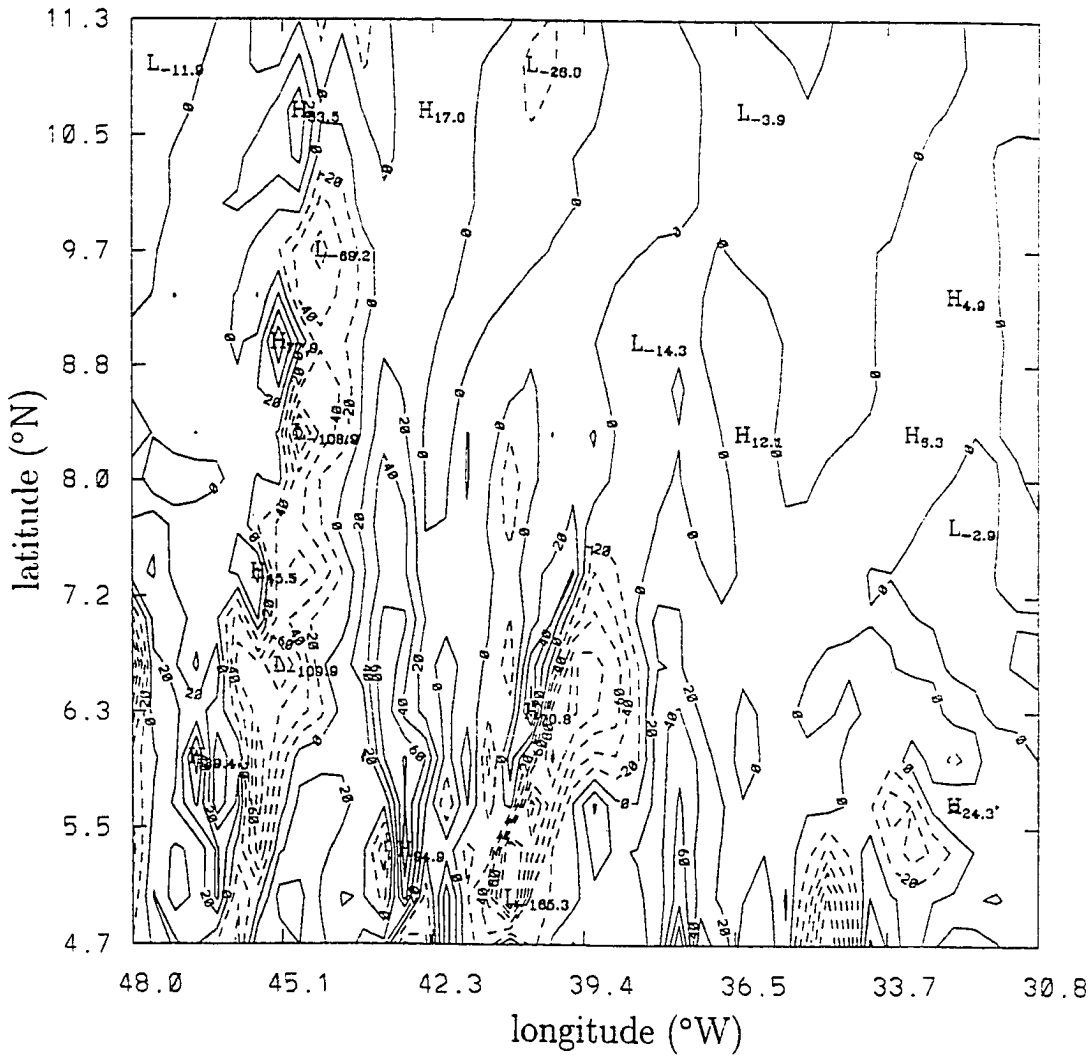

Figure 49: Time rate of change of relative vorticity calculated at two successive times separated by about three days (D033.48 and D036.52) using a finite difference scheme.

is found in Appendix 1. The eigenfunctions $\hat{w}_n$ and eigenvalues c_n where found by solving the following equation numerically

$$d^2\hat{w}_n/dz^2 + (N^2/c_n^2)\hat{w}_n = 0$$

subject to the boundary conditions

$$\hat{w} = 0 \ \ at \ \ z = 0, \ -H$$

where N is the Brunt-Väisälä frequency. A finite difference form of this equation was formulated for an irregularly spaced grid. The coefficients of the finite difference form of the equation at each depth were then used to construct a tridiagonal matrix. In this way, the boundary conditions were included in the formulation. The equation, in vector form, becomes

$$\mathbf{M}\hat{\mathbf{w}} = \lambda\hat{\mathbf{w}}$$

where λ=$1/c_n^2$ and $\mathbf{M}$ is the tridiagonal matrix. This expression was then solved using EISPACK, which is a fortran library of routines that returns the eigenvalues and eigenvectors of a matrix.

The definition of $N^2(z)$ is

$$N^2(z) = -\frac{g}{\rho_0}\frac{d\rho}{dz}$$

The $N^2(z)$ profile used in the equation was created by first averaging the vertical profiles of temperature and salinity over the region that was used in the vorticity analysis (5° to 11°N and 48°W to 31°W) for a particular field (in this case, D033.48). The temperature was converted to potential temperature and the density was calculated. $N^2(z)$ was then calculated using an upwind finite difference scheme. The resulting profile is seen in Figure 50. The differencing scheme placed the N^2 values at the depths corresponding to those of the CME vertical levels. The $\hat{w}_n$ values, produced by the EISPACK routine, consequently occurred at the same depths.

These vertical velocity eigenfunctions were then converted to pressure perturbation eigenfunctions, $\hat{p}_n$, by calculating the vertical gradient of $\hat{w}_n$ *i.e.*

$$\hat{p}_n = d\hat{w}_n/dz$$

Again, a finite difference scheme was used that placed the $\hat{p}_n$ values at the same vertical locations as the velocity variables. Hence, the modal amplitudes and the reconstructed velocities associated with each mode could be calculated at these locations.

The value chosen for the ocean depth, H, is that of the deepest level of the CME model (5500 m). There are, however, locations in the region of interest where the topography is shallower than this depth. As discussed in Appendix 1, the modal amplitudes are found by vertically integrating the product of the velocity and the pressure perturbation eigenfunction over the depth of the model ocean. This value is then divided by H. The velocities at the deeper levels of the model are insignificant in comparison to the values near the surface, hence their contribution to the integral is unlikely to be important. Consequently, the amplitudes calculated from velocity profiles in shallower depths (4500 m) and those obtained from profiles with the same structure in maximum depth waters are unlikely to differ greatly.

The vertical profiles of $\hat{w}_n$ and $\hat{p}_n$ for the first three baroclinic modes are seen in Figures 51 and 52. The values of c_n are 2.34, 1.44 and 0.83 m s^{-1} for $n = 1, 2, 3$, respectively. The values of the internal Rossby radius of deformation, R_n, for these modes are 115, 71 and 41 km. The R_1 value compares well with the value of 124 km reported by Emery et al. [1984] for this region, while the c_1 value, which can be found using $c_n = f_0 R_n$, is 2.2 m s^{-1} at 7°N.

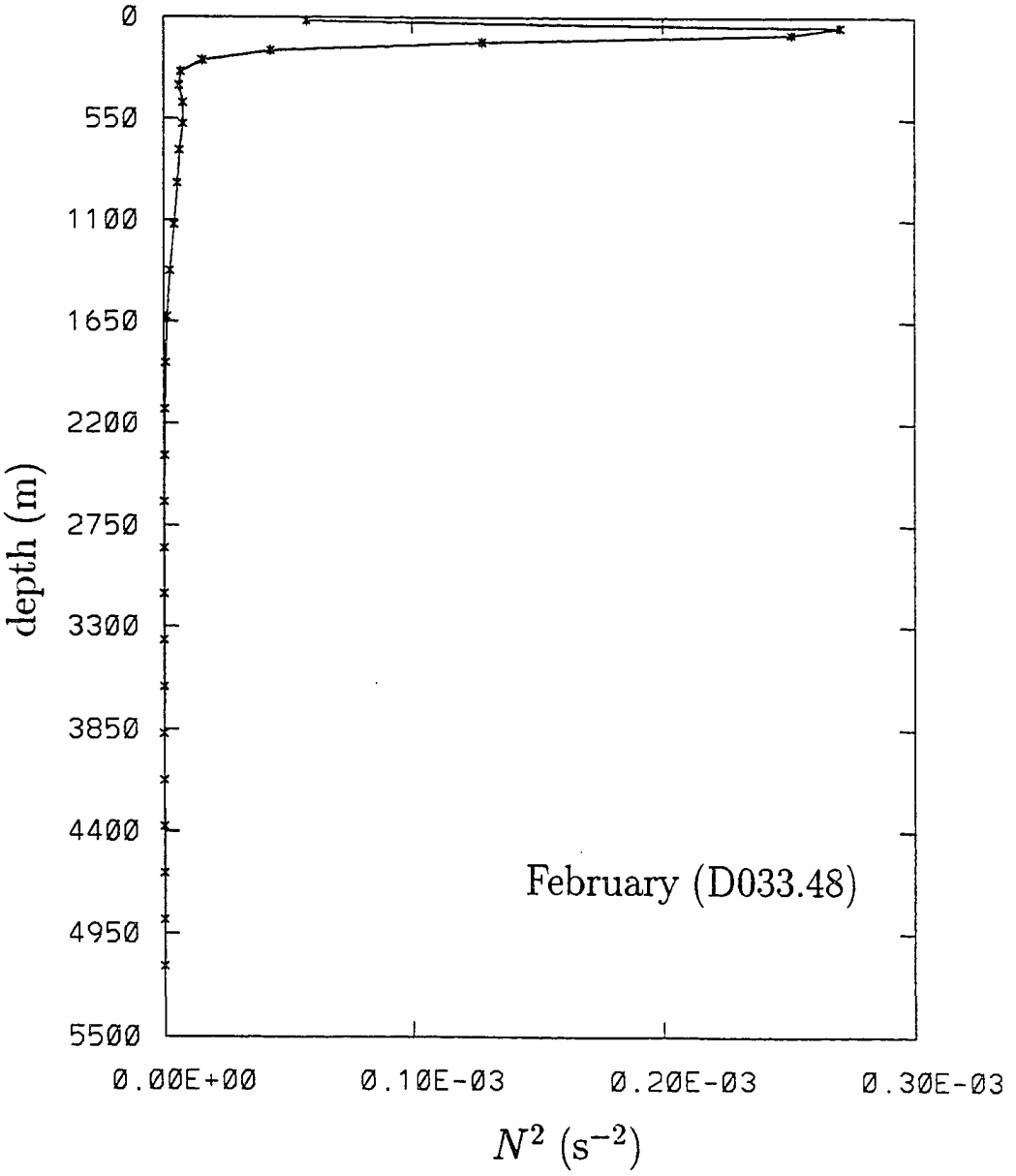

Figure 50: $N^2(z)$ (s^{-2}) profile averaged over the domain for an individual field in February (D033.48).

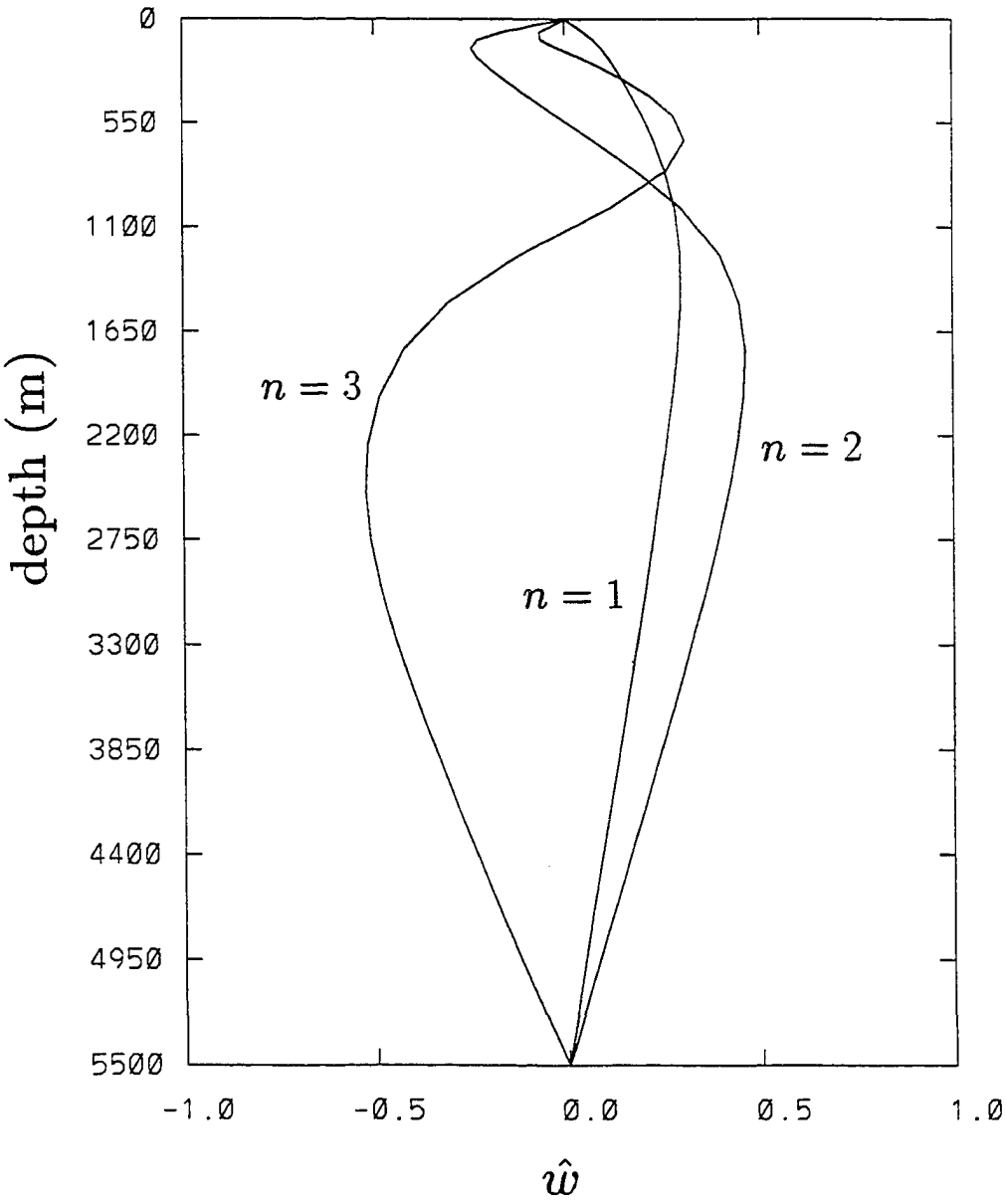

Figure 51: Vertical profiles of the vertical velocity eigenfunction, $\hat{w}_n$, for $n = 1$, 2, 3.

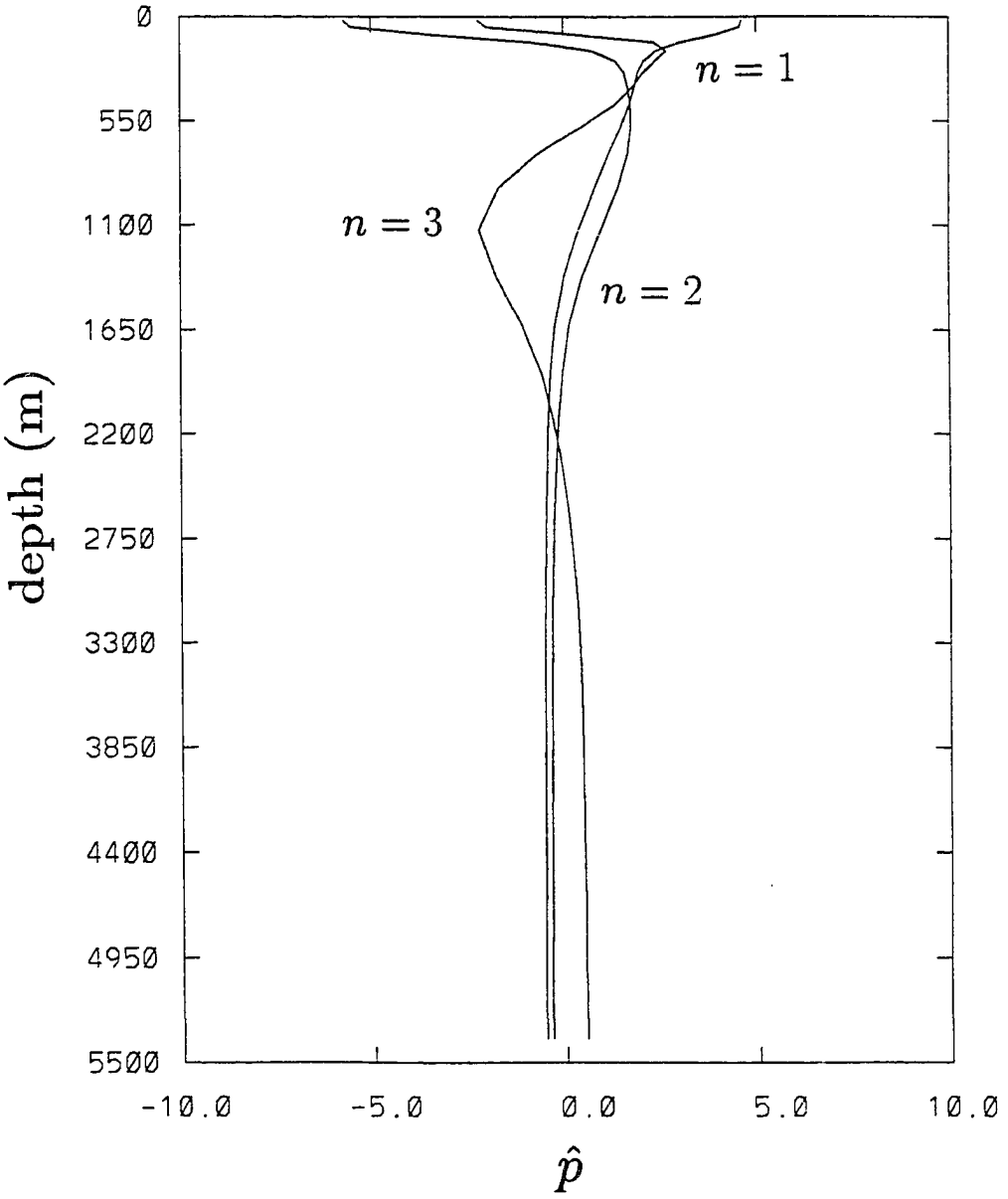

Figure 52: Vertical profiles of the pressure perturbation eigenfunction, $\hat{p}_n$, for $n = 1, 2, 3$.

The meridional (v) and zonal (u) components of velocity at 92 m from the D033.48 field were each modally decomposed over the region 5°N to 11°N and 48° to 31°W. Each of the reconstructed velocity fields associated with the barotropic and first three baroclinic modes were subjected to the vorticity analysis. The leading balance for the $n = 1$ case is that representing baroclinic Rossby waves (Figure 53).

$$\zeta_t = -\mathbf{u}_H \cdot \nabla\zeta - \beta v + f w_z$$

Alternating bands of highs and lows are again seen in the $\mathbf{u}_H \cdot \nabla\zeta$, βv and ζ_t maps in the region through which the waves propagate. The $\mathbf{u}_H \cdot \nabla\zeta$ term dominates the balance as in the undecomposed case; this term is again dominated by $u\partial\zeta/\partial x$. The stretching term is less coherent and its contribution is less than the other three terms. The remaining terms of the equation were negligible in comparison to the leading terms. Examination of the maps for the $n = 2$ case, show the leading balance to again be that for baroclinic Rossby waves (Figure 54). The stretching term is contributing a little more in this case. The magnitudes of the leading terms are similar for both cases.

All the terms for the $n = 3$ case are negligible in comparison to the terms obtained for the first and second modes. No Rossby wave balance is seen in this case (Figure 55). In the barotropic case, $n = 0$, the dominant terms in the oscillation region are βv and ζ_t (Figure 56); this balance of terms represents barotropic Rossby waves. Horizontal advection of relative vorticity is insignificant.

These vorticity analyses yielded leading balances in the region of the oscillations that represent barotropic and first and second mode baroclinic Rossby waves. To verify that the modal decomposition did not filter out a significant process, the velocity fields associated with the first and second baroclinic modes and the barotropic

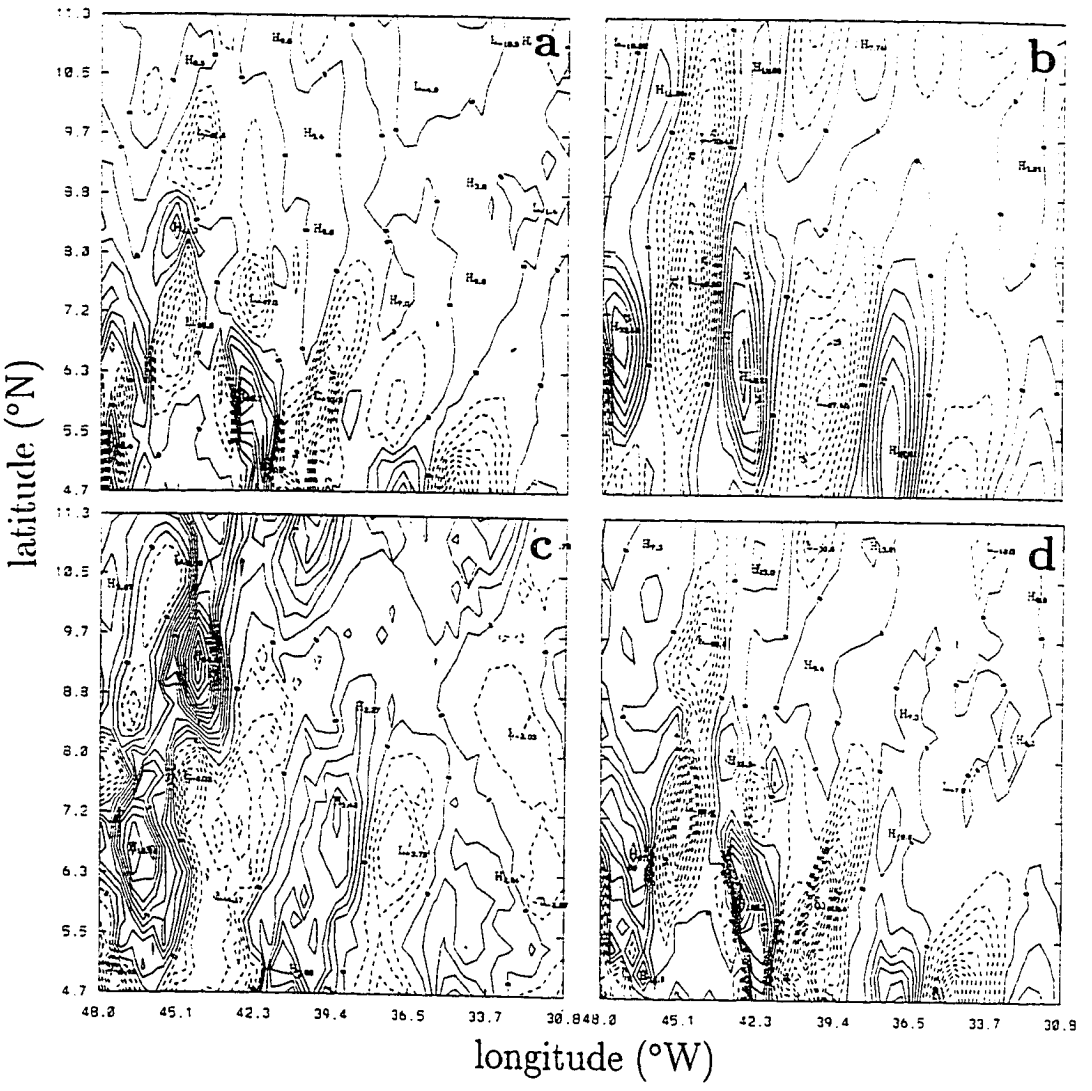

Figure 53: Leading balance of terms from full vorticity equation: (a) $\mathbf{u}_H \cdot \nabla\zeta$ (b) βv(c) fw_z and (d) ζ_t, for $n = 1$ mode for February (D033.48) at 92 m.

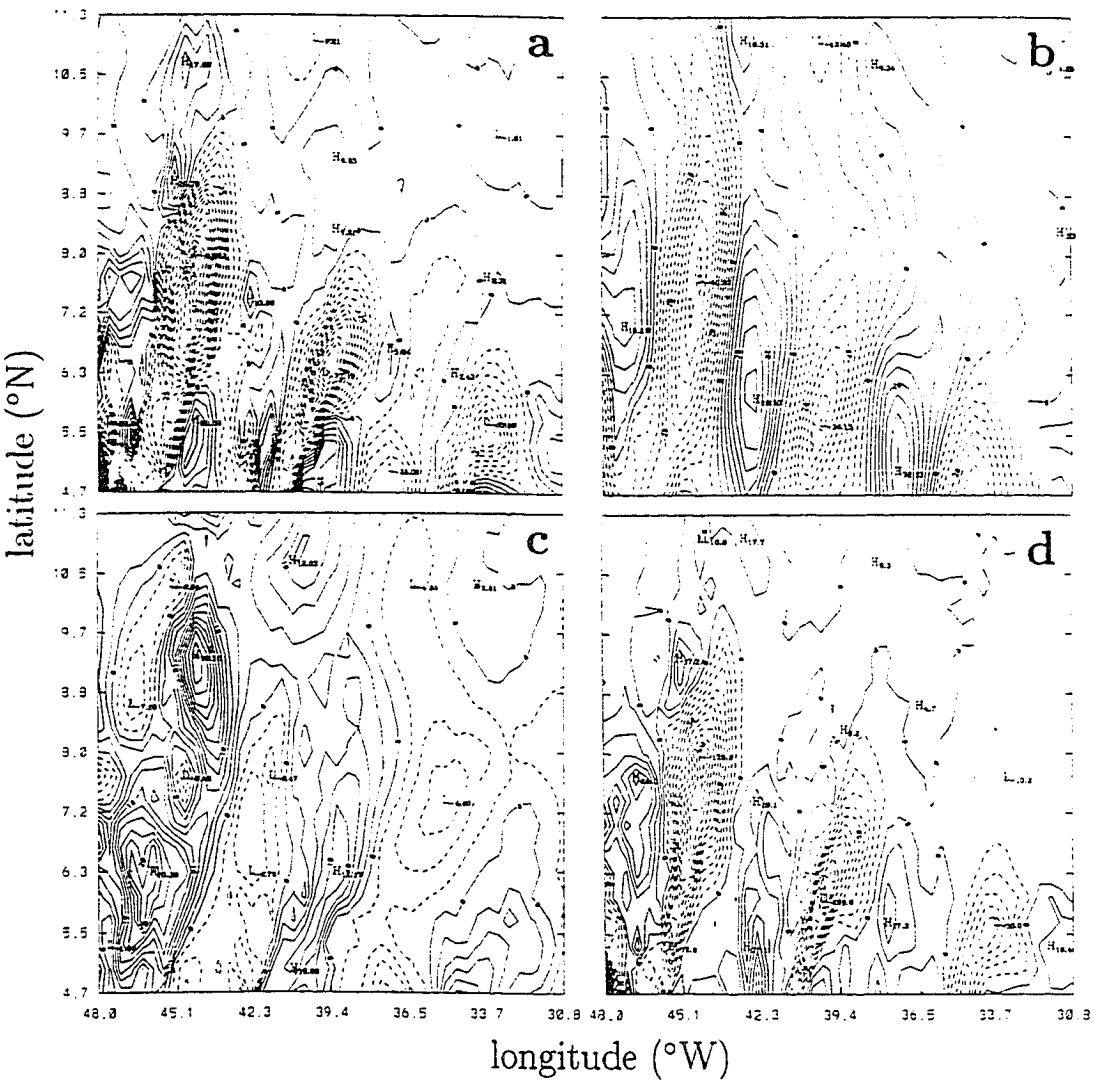

Figure 54: Same as Figure 53, except for $n = 2$ mode.

mode were summed and the vorticity analysis repeated. The leading terms had similar magnitudes (Figure 57) to those in the undecomposed case, verifying that no other major process was lost due to the modal decomposition. The spatial patterns of the terms have the advantage over the undecomposed case of being less noisy and the wave patterns are more easily identifiable.

Having proved that the 50-day oscillations are primarily first and second mode baroclinic Rossby waves, the question remains as to their cause. The time history of the meridional velocity contours suggested that they arose from the standing meander pattern of the NECC when the flow of this current stopped. To determine if this is likely, the leading balances of the terms in the vorticity equation are sought when the NECC is fully active. If balances representing baroclinic Rossby waves are found, it would be reasonable to suggest that the 50-day oscillations observed after the disappearance of the NECC are the same waves, only advected westward rather than eastward.

The $N^2(z)$ profile for an individual field in November (D319.59) was calculated in the manner discussed above. Concurrent velocity fields at 92 m were then modally decomposed and the velocities associated with the barotropic and first three baroclinic modes were reconstructed and subjected to the vorticity analysis. The dominant terms were seen in the retroflection and meander region of the NECC. Leading balances representing baroclinic Rossby waves were obtained for the first and second modes. The terms derived for the third baroclinic mode were insignificant in comparison to those for the first and second modes. The velocities associated with the barotropic and first and second baroclinic modes were again summed and the vorticity analysis repeated. The leading balance for this case is seen in Figure 58. The dominant balance indicates that baroclinic waves are present in the standing

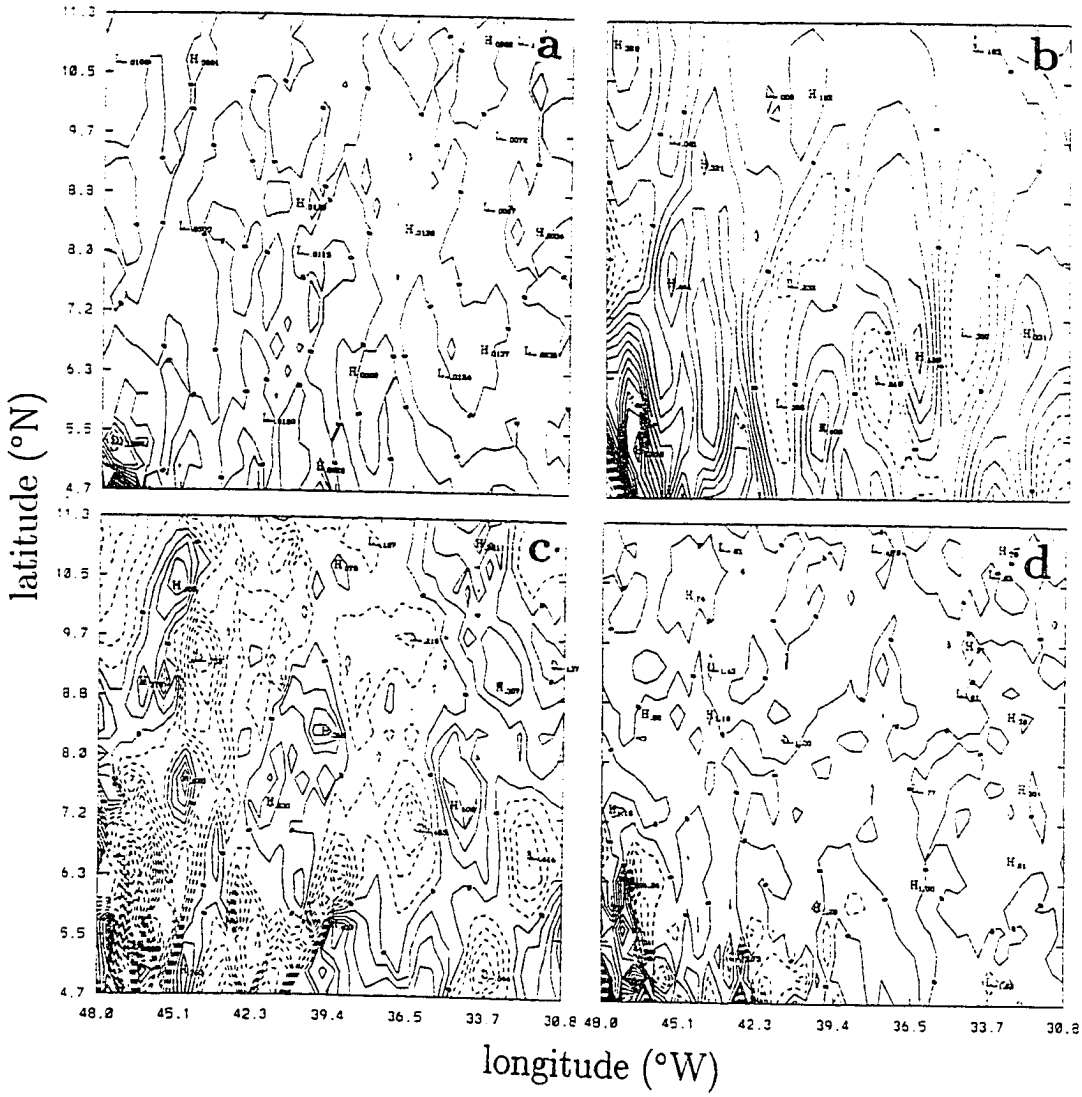

Figure 55: Same as Figure 53, except for $n = 3$ mode.

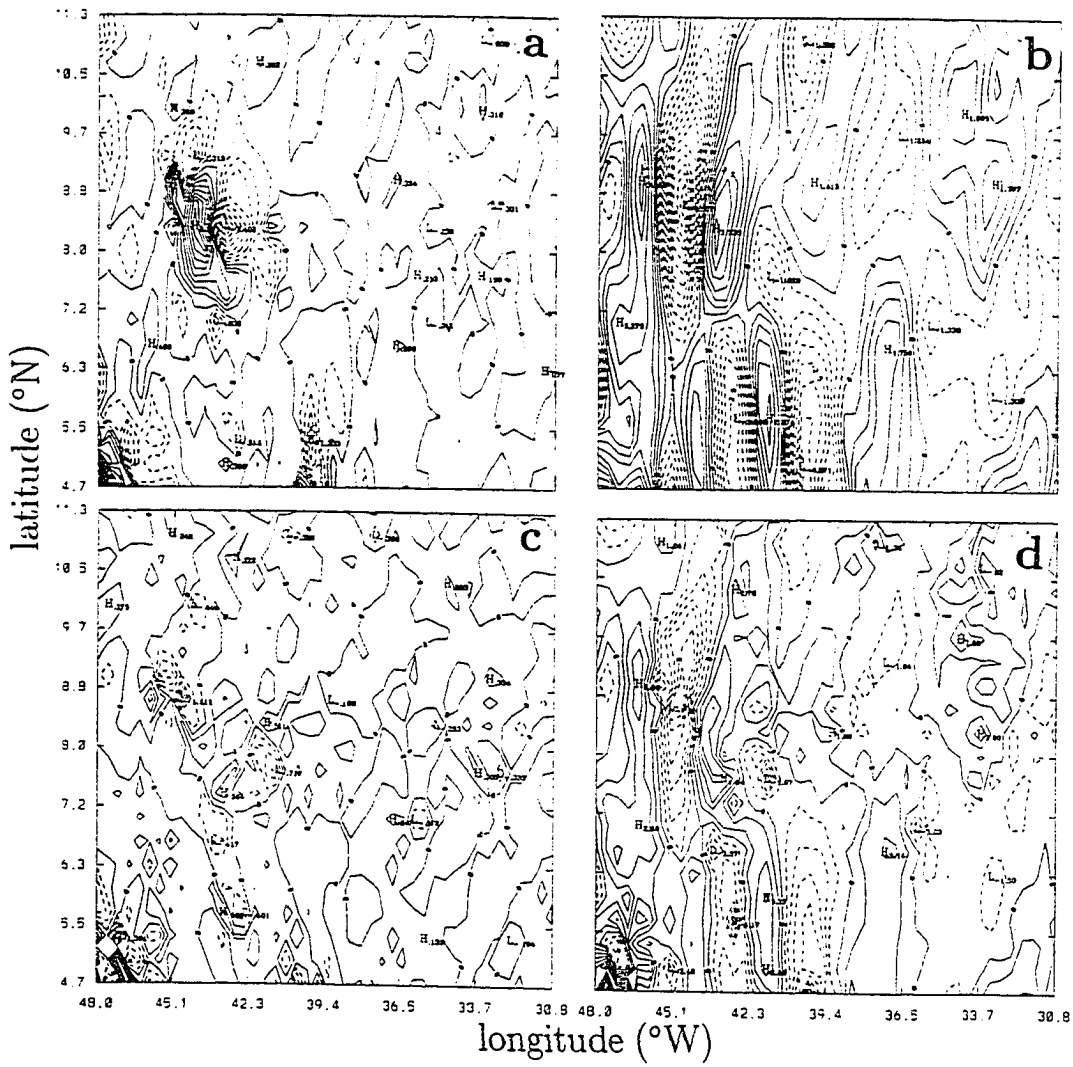

Figure 56: Same as Figure 53, except for the barotropic, $n = 0$, mode.

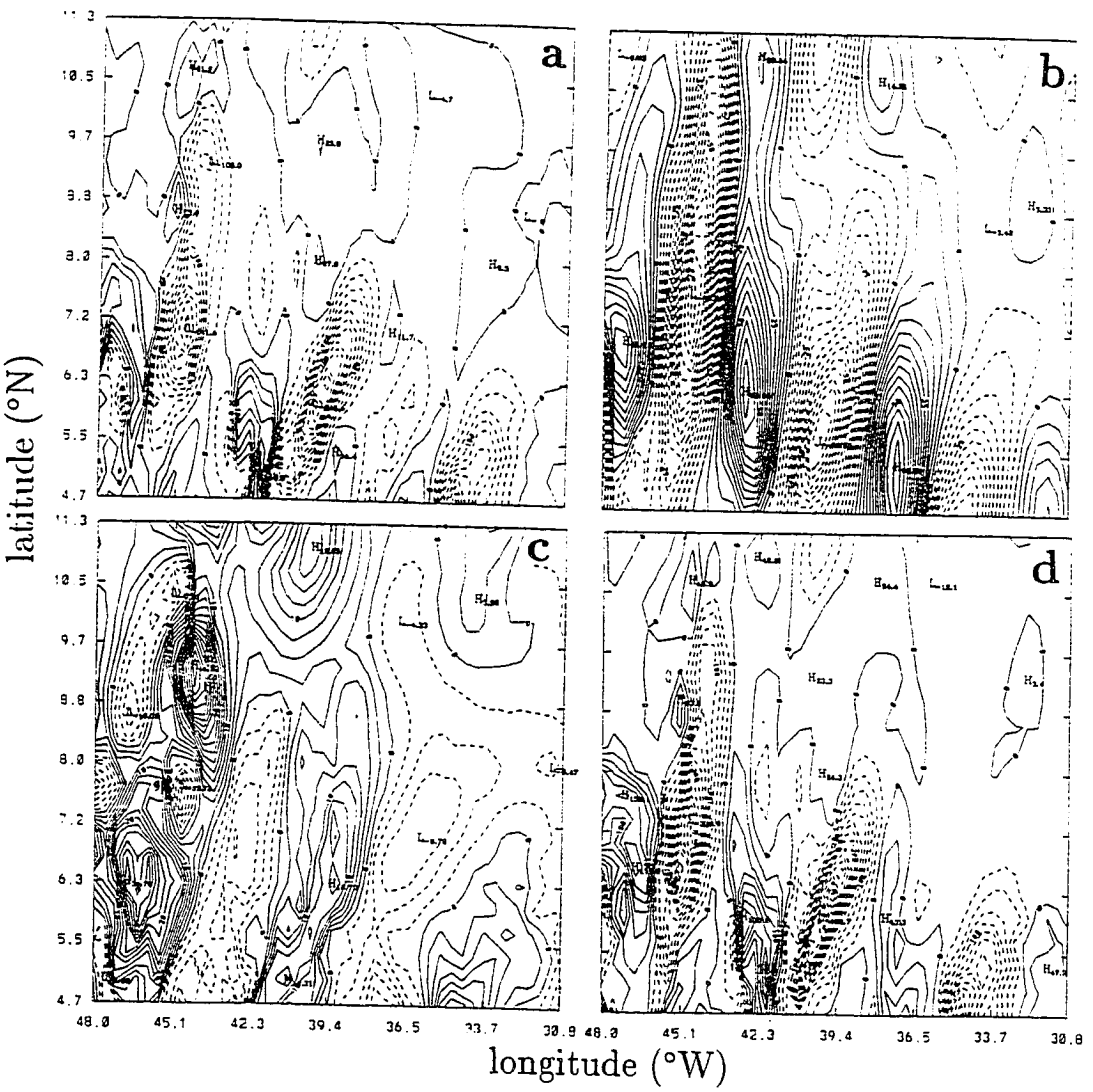

Figure 57: Same as Figure 53, except for $n = 0, 1, 2$ modes summed together.

meander region. Horizontal advection of relative vorticity, which is mainly due to $u\partial\zeta/\partial x$, is again the dominant term. Here, the flow is eastward due to the NECC, hence the waves are advected eastward. The scenario suggested above, therefore, quite possibly explains the cause of the 50-day oscillations.

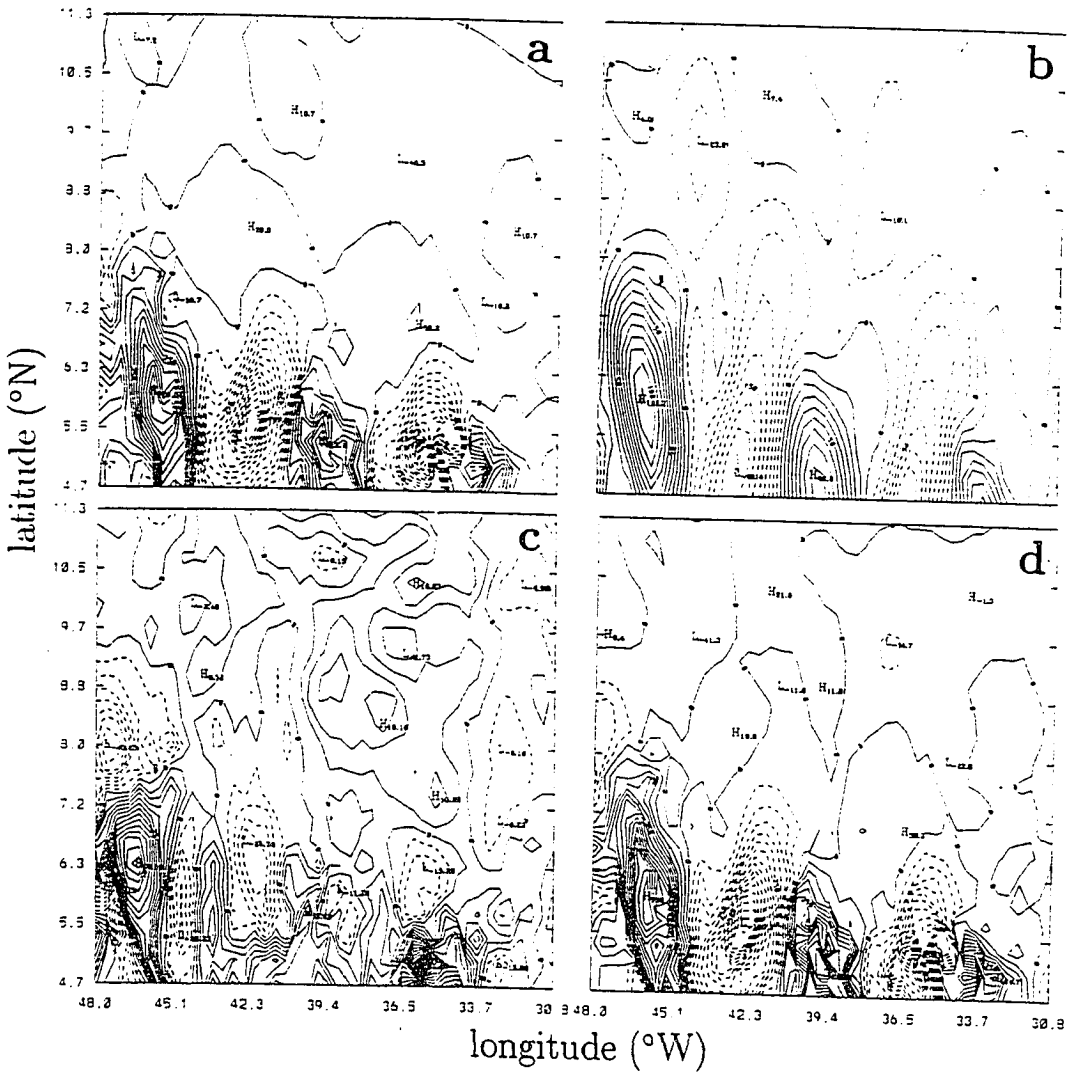

Figure 58: Leading balance of terms from full vorticity equation: (a) $\mathbf{u}_H \cdot \nabla\zeta$ (b) βv(c) fw_z and (d) ζ_t, for $n = 0, 1, 2$ summed modes for November (D319.59) at 92 m.

6 Discussion

Findings in the last section, strongly suggest that 50-day oscillations originate from the westward advection of vorticity anomalies left over by the NECC. This scenario will be discussed shortly in the light of the analytic solutions obtained Campos and Olson [1991]. In the Indian ocean, these oscillations have been attributed to wind forcing; the likehood of it being responsible in the CME model will be also be discussed. The results from this study will then be compared with those in the Atlantic and those obtained from modeling and observational studies in the Indian Ocean. Finally, the usefulness of general circulation models in these types of studies will be discussed.

Earlier it has been suggested that the 50-day oscillations are westward advected leftovers of the NECC meanders. As discussed in the Introduction, Campos and Olson [1991] obtained a solution from their analytical model which could represent the NBC retroflection and the meandering NECC. The solution contained Rossby waves with amplitude constant in time, decaying spatially. Since the source of these waves was the western boundary region, the waves with eastward group velocity, were superimposed on a eastward flowing, westward boundary current extension. The NECC can be viewed as an extension of the retroflecting NBC, hence this solution can be thought of as simulating the NECC meanders. The 50-day oscillations, which are baroclinic Rossby waves with very slow eastward group velocity, appear as the NECC breaks down. They are advected westward by the flow, and decay by the end of April. Since the nature of the NECC meanders and the 50-day oscilla-

tions is the same, it is reasonable to conclude that they are the same phenomenon. The vorticity analysis confirms this idea in some detail: the meanders are first and second mode baroclinic Rossby waves, very similar to the 50-day oscillations.

These findings, together with the time history of the flow point to the following scenario regarding the 50-day oscillations. It begins roughly in July with the retroflecting NBC producing Rossby waves with very slow eastward group velocity near the western boundary. These waves can be identified in Figure 18b, where they are limited to the western boundary region. The NECC then becomes stronger by August (Figure 19a) and the waves have penetrated to the interior of the basin (35°W) due to eastward advection by the NECC (Figure 19b). where they dissipate. A stationary Rossby wave pattern is established for several months, while the NECC is active. In December, the NECC starts to slow (Figure 23a) and the waves retreat westwards (Figure 23b). Hence, the meander pattern is slowly released as the NECC slows. By February the NECC has largely disappeared (Figure 25a), but the leftover waves are pronounced, retreating westwards with the flow (Figure 25b). By April, the waves have almost entirely disappeared (Figure 27b). In May they are absent (Figure 28b) and the zonal flow is mainly to the west (Figure 28a). In June, the NECC starts up again and the whole process is repeated.

Observational studies in the Indian Ocean have pointed to the 40- to 50-day oscillation of the wind field in the lower troposphere discovered by Madden and Julian [1972] as a possible cause of these oscillations. The CME model is forced with climatological mean monthly winds, hence little wind energy in the 40- to 60-day period is contained in the model forcing. So, although the oscillations could be produced by wind forcing at the periods of the Madden-Julian oscillation in the real ocean, it is not possible in this model.

For the same reason Kindle and Thompson [1989] disregarded wind forcing as the cause of 50-day oscillations in their reduced-gravity layer model. Rather, they attributed the oscillations to barotropic instability. The scenario suggested in this thesis, however, could be equally valid in the Indian Ocean. The standing meander pattern associated with the East African Coastal Current (EACC) in Kindle and Thompson's model breaks down in April, and 50-day oscillations, presumably Rossby waves, appear. There is every reason to believe that the processes seen in the CME model also occurs in theirs.

Rossby waves seen in the CME model are also presumably responsible for the 50-day oscillations observed by Johns et al. [1990] off the South American coast. One notable difference between the model and observations is that Johns et al. [1990] found oscillations of periods between 40 and 60 days in the meridional component of velocity of the NBC region throughout the year, whereas they are only present in the CME model from December through April. It is not particularly surprising that Rossby waves near the coast are excited by different mechanisms. The wind forcing used in the CME model lacks the high frequency components which may be responsible. Also topographic features reflected in the model geometry may be efficient generators of short Rossby waves in the NBC.

Finally, some mention should be made of the usefulness of general circulation models such as the CME simulation. These calculations have the spatial and temporal resolution to reveal intricate dynamical details, such as individual components of the vorticity balance. To obtain an understanding of the dynamics governing these oscillations, a time sequence of velocity from the western tropics for at least one year were required. Such resolution is not available from observations today or

in the foreseeable future. The model does not contain some of the forcing acting on the real ocean such as the high-frequency components of the wind field nor does it portray dissipative processes well. These very simplifications of the model were responsible, however, for the clarity with which the waves could be identified in the model.

7 Conclusion

The behavior, nature and dynamics of 50-day oscillations were investigated in the western tropical region of the CME general circulation model. These oscillations were seen in the meridional component of velocity between 35° and 55°W and between 5° and 11°N. They occur between December and April and their onset coincides with the seasonal break down of the meander pattern of the NECC. They appear first near 36°W, 5°N and are advected westwards. They have a westward phase speed of 0.1 m s^{-1}, a wavelength of about 500 km and a very slow eastward group velocity. Their period, phase speed and wavelength agree with observations [Johns et al. 1990].

Calculation of the leading balance of terms from the full vorticity equation in the region where the oscillations occur, following a modal decomposition, showed that the oscillations were first and second mode baroclinic Rossby waves. Repetition of this analysis during the retroflection period revealed the NECC meanders to be first and second mode baroclinic Rossby waves; the same as the 50-day oscillations. These findings, together with the time evolution of the flow field over an annual cycle, suggested that the 50-day oscillations were the westward advected residue of the NECC meander pattern that is released as the NECC slows in fall. Wind forcing was not considered to be responsible for the oscillations.

This study represents the first thorough attempt to explain the nature and cause of 50-day oscillations; hitherto, their nature was determined from limited data, while

explanations for their cause were largely speculative. A potentially important reason for understanding these dynamics is that 50-day oscillations may contribute significantly to poleward heat transport. A future study investigating their contribution could be guided by the findings in this thesis.

This research could also serve as a guide for an observational study in this region. Spectra of the current meter data collected by Richardson and Reverdin [1987] at 6°N, 28°W display a significant peak at 50 days. Hence, several current meter arrays could be placed along the path which the waves were advected. The description and dynamics found in the model could then be validated in the ocean interior. As well, the importance of the high-frequency wind forcing could be assessed by collecting concurrent wind data.

Appendix 1

To investigate the nature of current fluctuations, the flow can be separated into barotropic (depth-independent) and baroclinic parts. For motion whose scales are much larger in the horizontal than in the vertical, the method of separation of variables can be used to express the solution as a sum of normal modes, each of which has a fixed vertical structure and a solution in the horizontal and time dimensions. In a continuously stratified ocean, this is expressed for some variable q [Kundu, 1990] as

$$q = \sum_{n=0}^{\infty} q_n(x,y,t)\psi_n(z)$$

The vertical structure of a mode is described by ψ_n, q_n is the horizontal propagation of the mode and n is the mode number.

Following Gill and Clarke [1974], separable solutions are assumed for horizontal velocities u and v:

$$u = \sum_{n=0}^{\infty} u_n(x,y,t)\hat{p}_n(z) \tag{1}$$

$$v = \sum_{n=0}^{\infty} v_n(x,y,t)\hat{p}_n(z) \tag{2}$$

where u_n and v_n are modal amplitudes and $\hat{p}_n$ is the pressure perturbation eigenfunction. Now,

$$\hat{p}_n = d\hat{w}_n/dz \tag{3}$$

where $\hat{w}_n$ is the vertical velocity eigenfunction which satisfies

$$d^2\hat{w}_n/dz^2 + (N^2/c_n^2)\hat{w}_n = 0 \tag{4}$$

N is the Brunt-Väisälä frequency and c_n are the eigenvalues. The expression for N^2 is The expression for N^2 is

$$N^2(z) = -\frac{g}{\rho_0}\frac{d\rho}{dz}$$

c_n is otherwise known as the separation constant and is related to the equivalent depth, H_e, by

$$c_n = gH_e$$

H_e is the depth over which each mode in a stratified flow acts like a homogeneous layer in the horizontal dimensions and in time [Kundu, 1990]. It is the speed at which long internal waves propagate in the non-rotating case.

The eigenfunctions $\hat{w}_n$ and the eigenvalues c_n for the baroclinic modes ($n = 1, 2, ..$) are obtained by solving equation (2) subject to specified boundary conditions. Equation (2) is of the Sturm-Liouville form, for which the solutions are orthogonal. It is also the form for which the Boussinesq approximation has been made (ρ_0 varies slowly compared with $\hat{w}$). To solve the equation, the ocean is assumed to be of constant depth, H, with a rigid lid. Hence, the boundary conditions are

$$\hat{w} = 0 \quad at \quad z = 0, \; -H \tag{5}$$

The amplitudes u_n and v_n are obtained by exploiting the orthogonality relationship between the modal solutions. The technique employed involves the expansion of arbitrary functions in series of orthogonal functions [Hildebrand, 1976]. Both sides of equation (1) are multiplied by the pressure perturbation eigenfunction of the mth mode, $\hat{p}_m$, and vertically integrated over the depth of the ocean.

$$\int_{-H}^{0} u_j \hat{p}_{mj} dz = \sum_{n=1}^{N} u_n \int_{-H}^{0} \hat{p}_{nj}\hat{p}_{mj} dz$$

where j refers to the depth index. Now the modes are orthogonal, so

$$\delta_{mn} = \begin{cases} 1 & \text{m=n} \\ 0 & \text{m}\neq\text{ n} \end{cases}$$

As a result

$$\int_{-H}^{0} u_j \hat{p}_{mj} dz = u_m \int_{-H}^{0} \hat{p}_{mj}^2 dz$$

where u_m is the amplitude of the mth mode. The integral of the square of the pressure eigenfunction has a positive numerical value [Hildebrand, 1976]. Therefore, let

$$C_m = \int_{-H}^{0} \hat{p}_m^2 dz$$

The eigenfunctions are normalized by the total water depth such that the value of this integral is unity. To be consistent with this scheme, the amplitudes must be normalized by the total water depth. Hence, the amplitude associated with the mth mode is

$$u_m = \frac{1}{H} \int_{-H}^{0} u_j \hat{p}_{mj} dz \tag{6}$$

The velocity signal for the mth mode at the jth depth is then reconstructed by multiplying u_m by $\hat{p}_{mj}$ *i.e.*

$$u = u_m \hat{p}_{mj}$$

Having investigated the baroclinic modes contributing to the flow, the barotropic mode ($n = 0$) remains to be considered. The pressure perturbation eigenfunction for this mode, $\hat{p}_0$, equals one. Hence, using equation (6), the amplitude for the barotropic mode is

$$u_0 = \frac{1}{H} \int_{-H}^{0} u_j dz$$

and the reconstructed velocity associated with this mode equals u_0.

Bibliography

Bendat, J. S., and A. G. Piersol, Random data, *2nd. ed. John Wiley & Sons Inc., U. S. A., 566 pp*, 1986.

Boyd, J. D., Thermohaline steps off the northeast coast of South America, *Ph. D. thesis*, Texas A&M University, College Station, TX, 1986.

Bruce, J. G., J. Kerling, and W. Beatty, On the North Brazilian eddy field, *Prog. Oceanogr., 14*, 57-63, 1985.

Byran, K., A numerical method for the study of the circulation of the world ocean, *J. Comput. Phys., 4*, 347-376, 1969.

Bryan, F. O., and W. R. Holland, A high resolution simulation of the wind- and thermohaline driven circulation in the North Atlantic Ocean, *Proceedings Hawaiian Winter Workshop: Parameterizations of small scale processes.*, Univ. of Hawaii, Jan 17-20, 1989.

Campos, E. J. D., and D. B. Olson, Stationary Rossby waves in western boundary current extensions, *J. Phys. Oceanogr., 21*, 1202-1224, 1991.

Cooley, J. W., P. A. L. Lewis, and P. D. Welch, The fast Fourier transform and its applications, *IEEE Transactions on Education*, 12(1), 1969.

Cox, M. D., A primitive equation three dimensional model of the ocean, *GFDL Ocean Group Technical Report No. 1*, Geophysical Fluid Dynamics Laboratory/NOAA, 1984.

Csanady, G. T., Retroflection and leakage in the North Brazil Current: Critical point analysis, *J. Mar. Res., 48*, 701-728, 1990.

Didden, N., and F. Schott, Seasonal variations in the western tropical Atlantic: surface circulation from Geosat altimetry and WOCE model results, *J. Geophys. Res., 97*, 3529-3541, 1992.

Emery, W. J., and J. S. Dewar, Mean temperature-salinity, salinity-depth and temperature-depth curves for the north Atlantic and the north Pacific, *Prog. Oceanog., 11*, 219-305, 1982.

Emery, W. J., W. G. Lee, and L. Magaard, Geographic and seasonal distribution of Brunt-Väisälä frequency and Rossby radii in the north Pacific and north Atlantic, *J. Phys. Oceanogr., 14*, 294-317, 1984.

Flagg, C. N., R. L. Gordon, and S. McDowell, Hydrographic and current observations on the continental slope and shelf of the western equatorial Atlantic, *J. Phys. Oceanogr., 16*, 1412-1429, 1986.

Garzoli, S. L., and E. J. Katz, The forced annual reversal of the Atlantic North Equatorial Countercurrent, *J. Phys. Oceanogr., 13*, 2082-2090, 1983.

Gill, A. E., and A. J. Clarke, Wind-induced upwelling, coastal currents and sea-level changes, *Deep-Sea Res., 21*, 325-345, 1974.

Halpern, D., Variability of near-surface currents in the Atlantic North Equatorial Countercurrent during GATE, *J. Phys. Oceanogr., 10*, 1213-1220, 1980.

Han, Y. J., A numerical world ocean general circulation model. Part II, A baroclinic experiment, *Dyn. Atmos. Oceans, 8*, 141-172, 1984.

Hellerman, S., and M. Rosenstein, Normal monthly wind stress over the world ocean with error estimates, *J. Phys. Oceanogr., 13*, 1093-1104, 1983.

Hénin, C., P. Hisard, and B. Piton, FOCAL, vol. 1, Observations hydrologiques dans l'Océan Atlantique Equatorial (juillet 1982 - août 1984), *Editons de l'ORSTOM Collect. Trav. et Doc., 196*, 191 pp., ORSTOM, 1986

Hénin, C., and P. Hisard, The North Equatorial Countercurrent observed during the Programme Océan et Climate Dans l'Atlantique equatorial experiment in the Atlantic ocean, July 1982 to August 1984, *J. Geophys. Res., 92*, 3751-3758, 1987.

Hildebrand, F. B., Advanced calculus for applications, *Prentice-Hall Inc., New Jersey, 733 pp*, 1976.

Jenkins, G. M., and D. G. Watts, Spectral analysis and its applications, *Holden-Day Inc., San Francisco, 525 pp*, 1968.

Johns, W. E., T. N. Lee, F. A. Schott, R. J. Zantoff, and R. H. Evans, The North Brazil Current retroflection: seasonal structure and eddy variability, *J. Geophys. Res., 95*, 22,103-22,120, 1990.

Katz, E. J., R. L. Molinari, D. E. Cartwright, P. Hisard. H. U. Lass, and A. deMesquita, The seasonal transport of the Equatorial Undercurrent in the western Atlantic (during the Global Weather Experiment), *Oceanol. Acta, 4*, 445-450, 1981.

Katz, E. J., Introduction, *FOCAL/SEQUAL*, i-ii, American Geophysical Union, 1987.

Kindle, J. C., and J. D. Thompson, The 26-day and 50-day oscillations in the western Indian ocean: model results, *J. Geophys. Res., 94*, 4721-4736, 1989.

Kraus, E. B., and J. S. Turner, A one-dimensional model of the seasonal thermocline: II. The general theory and its consequences, *Tellus, 19*, 98-106, 1967.

Kundu, P. K., Fluid mechanics, *Academic Press Inc., San Diego, 638 pp*, 1990.

LeBlond, P. H., and L. A. Mysak, Waves in the ocean, *Elsevier Scientific Publishers B. V., 602 pp*, 1978.

Levitus, S., Climatological Atlas of the World Ocean, *NOAA Prof. Pap. 13*, U. S. Govt. Print. Office, 173 pp, 1982.

Madden, R. A., and P. R. Julian, Description of global-scale circulation cells in the tropics with a 40-50 day period, *J. Atmos. Sci., 29*, 1109-1123, 1972.

Moore, D. W., Rossby waves in ocean circulation, *Deep-Sea Res., 10*, 735-747, 1963.

Moore, D., and P. Niiler, A two-layer model for the separation of inertial boundary currents, *J. Mar. Res., 32*, 457-484, 1974.

Mysak, L. A., and G. J. Mertz, A 40- to 60-day oscillation in the source region of the Somali Current during 1976, *J. Geophys. Res., 89*, 711-715, 1984.

Pedlosky, J., Geophysical Fluid Dynamics, *2nd. ed. Springer-Verlag, New York, 710 pp*, 1987.

Pinardi, N., and A. R. Robinson, Quasigeostrophic energetics of open ocean regions, *Dyn. Atmos. Oceans, 10*, 185-219, 1986.

Pinardi, N., and A. R. Robinson, Dynamics of deep thermocline jets in the POLYMODE region, *J. Phys. Oceanogr., 17*, 1163-1188, 1987.

Quadfasel, D. R., and J. C. Swallow, Evidence for 50-day period planetary waves in the South Equatorial Current of the Indian ocean, *Deep-Sea Res., 33*, 1307-1312, 1986.

Richardson, P. L., Moored current meter measurements in the Atlantic North Equatorial Countercurrent during 1983, *Geophys. Res. Lett., 11*, 749-752, 1984.

Richardson, P. L., and T. K. McKee, Average seasonal variation of the Atlantic equatorial currents from historical ship drifts, *J. Phys. Oceanogr., 14*, 1226-1238, 1984.

Richardson, P. L., and G. Reverdin, Seasonal cycle of velocity in the Atlantic North Equatorial Countercurrent as measured by surface drifters, current meters, and ship drifts, *J. Geophys. Res., 92*, 3691-3708, 1987.

Schott, F., M. Fieux, J. Kindle, J. Swallow, and R. Zantopp, The boundary currents east and north of Madagascar 2. direct measurements and model comparisons, *J. Geophys. Res., 93*, 4963-4974, 1988.

Schott, F. A., and C. W. Böning, The WOCE model in the western tropical Atlantic: upper layer circulation, *J. Geophys. Res., 96*, 6993-7004, 1991.

Spall, M. A., Regional primitive equation modeling and analysis of the POLYMODE data set, *Dyn. Atmos. Oceans, 14*, 125-174, 1989.

Spall, M. A., Circulation in the Canary basin: a model/data analysis, *J. Geophys. Res.*, *95*, 9611-9628, 1990.

Spall, M. A., Rossby wave radiation in the Cape Verde frontal zone, *J. Phys. Oceanogr.*, *22*, 796-807, 1992.

Swallow, J., M. Fieux and F. Schott, The boundary currents east and north of Madagascar 1. geostrophic currents and transports, *J. Geophys. Res.*, *93*, 4951-4962, 1988.

Swallow, J. C., F. Schott, and M. Fieux, Structure and transport of the East African Coastal Current, *J. Geophys. Res.*, *96*, 22,245-22,257, 1991.

Treguier, A. M., Kinetic energy analysis of an eddy resolving, primitive equation model of the north Atlantic, *J. Geophys. Res.*, *97*, 687-701, 1992.

Weisberg, R. H., J. H. Hickman, T. Y. Tang, and T. J. Weingartner, Velocity and temperature observations during the seasonal response of the Equatorial Atlantic Experiment at 0°, 28°W, *J. Geophys. Res.*, *92*, 5061-5075, 1987.